PNNL-29603

FY 2019 Report of the Atmosphere to Electrons Mesoscale-to-Microscale Coupling Project

December 2019

SE Haupt   D Allaerts
L Berg   M Churchfield
A DeCastro   C Draxl
DJ Gagne   P Hawbecker
P Jimenez   A Jonko
T Juliano   C Kaul
B Kosović   TC McCandless
J Mirocha   D Munoz-Esparza
E Quon   R Rai
J Sauer   W Shaw

FY 2019 Report of the Atmosphere to Electrons Mesoscale-to-Microscale Coupling Project

December 2019

SE Haupt[1]
L Berg[3]
A DeCastro[1]
DJ Gagne[1]
P Jimenez[1]
T Juliano[1]
B Kosović[1]
J Mirocha[5]
E Quon[2]
J Sauer[1]

D Allaerts[2]
M Churchfield[2]
C Draxl[2]
P Hawbecker[1,2]
A Jonko[4]
C Kaul[3]
TC McCandless[1]
D Munoz-Esparza[1]
R Rai[3]
W Shaw[3]

Pacific Northwest National Laboratory
Richland, Washington 99354

[1] National Center for Atmospheric Research (NCAR)
[2] National Renewable Energy Laboratory (NREL)
[3] Pacific Northwest National Laboratory (PNNL)
[4] Los Alamos National Laboratory (LANL)
[5] Lawrence Livermore National Laboratory (LLNL)

Summary

The overall goal of the Mesoscale-to-Microscale Coupling (MMC) project is to improve coupling between mesoscale and microscale simulations via improved guidance and new strategies for setting up simulations and the development of new tools that can be used across the community. Including the mesoscale forcing is critical to modeling the full energy transfer across scales in the atmosphere. The project-specific objectives include:

- Apply rigorous verification and validation (V&V) techniques to the new modeling tools that are developed as part of the project to ensure the accuracy of our codes and results and develop estimates of the relative uncertainty.

- Improve computational performance of the coupled MMC models through the development of methods that can be used to reduce turbulence spin-up time and hence the size of computational domains.

- Improve representation of the surface layer in microscale models to enhance simulations of hub-height wind speed.

- Develop guidance for the community describing the best ways to couple mesoscale and microscale models, including specific spatial scales at which the handoff to the microscale model should occur.

- Prepare documentation and a suite of software tools that can be used across the community.

- Transition MMC research to the offshore environment.

Major progress was made in each of these areas during FY19. Two coordinating initiatives position the team for making important contributions that can be easily transitioned to industry use. The first of these initiatives is building an MMC-specific Phenomena Identification and Ranking Table (PIRT) that allows us to identify the most important areas for research. The PIRT identified that offshore wind issues are important, but not yet modeled or validated well at this time. Specific phenomena to pursue include low-level jets, land-sea breezes, weather fronts, tropical cyclones, Nor'easters, thermal pooling and terrain-gap flows, icing and precipitation, surface energy and momentum exchange, air-water-wave interactions, and roughness and canopy effects. The second major initiative was to compile and archive MMC code in a GitHub repository that forms the basis of the code and toolset that is being transitioned to industry. This repository includes assessment tools in the form of Jupyter notebooks written in Python that enable reproducible comparisons of multiple techniques. It also includes a common base of the Weather Research and Forecasting (WRF) model that is our mesoscale solver. This MMC version is based on WRF v4.1, includes MMC-specific upgrades and additions, and is accompanied by a "setups" repository. These major initiatives enable all of the objectives listed above.

Progress has been made on the mesoscale modeling side of the project in terms of advancing a fully three-dimensional version of the planetary boundary layer (3D PBL) scheme for WRF that began during the second Weather Forecast Improvement Project (WFIP 2) project. The scheme does not assume horizontal homogeneity as do the current PBL schemes, which is critical as mesoscale modeling proceeds to finer scales. During FY19, the team ported the 3D PBL code to WRF v4.0.3 and thoroughly tested it, implemented and tested a substepping scheme, implemented prognostic turbulence kinetic energy (TKE) computation, and advanced the ways that the surface boundary conditions are handled by the scheme. The team also made progress

on machine-learning surface layer schemes for WRF to replace the traditional Monin-Obukov Similarity Theory (MOST) approach. Both random forests and artificial neural networks can be trained to predict friction velocity, temperature scale, and moisture scale, even improving on MOST for flat-terrain sites different than those on which the models were initially trained.

Major efforts were put into rigorous, systematic comparisons of multiple techniques in two major areas in FY19. The first major area was in the coupling techniques themselves. Coupling configurations that were tested include WRF to WRF-Large-Eddy Simulation (WRF-LES), WRF to the Simulator fOr Wind Farm Applications (SOWFA) in a few configurations, WRF to Nalu-Wind, and Observations to SOWFA. This comparison will be completed in FY20. Additional coupling work includes:

1. Development of the "profile assimilation technique" and further examined and documented best practices for the "budget component approach."

2. Study of the effect of complex terrain in creating turbulence in the microscale domain when mesoscale inflow that lacks resolved turbulence is applied as inflow.

3. Advanced methods to handle atmospheric gravity waves within the microscale domain.

4. Examination of the effect of the activation or deactivation of the atmospheric physical process parameterizations within the microscale domain that may impact the formation of turbulence and other phenomena of importance to wind energy.

The second major area of intercomparison was in initiating turbulence at the microscale that is not resolved at the mesoscale. Methods include stochastic perturbations in the thermal field, stochastic perturbations in the momentum field, and generating turbulence using synthetic methods, such as the Mann or TurbSim methods. The intercomparison has been greatly facilitated by the common assessment tools, and this work will be completed and published in FY20.

At the microscale, the team compared Nalu-Wind to several other microscale solvers, following up on the team's previously published work (Mirocha et al. 2018). Nalu-Wind's predictions of the wind speed profile were generally found to be as consistent with the observed wind speeds as the results of the previously tested microscale solvers, but some potential areas for improvement were also identified. Further evaluation of Nalu-Wind for simulation of atmospheric boundary layers is planned using both canonical flow configurations and coupled runs with realistic forcing derived from mesoscale simulations.

Team members also constructed a "lidar simulator" within the WRF model that allows direct comparison of MMC simulations to scanning lidar data, allowing a more complete picture of the turbulence field than available from point observations. Analysis showed that the orientation and size of both simulated and observed spatial structures resulting were found to be similar.

To quantify the uncertainty in the MMC simulations, the team took a parametric approach to analyzing the effect of choice of parameters, focusing on the WRF model in FY19. An ensemble of several dozen coupled WRF/WRF-LES simulations of a convective boundary layer observed during the WFIP 2 campaign was performed, varying key parameters of a common turbulent kinetic energy-based subgrid-scale (SGS) closure. Parameter sensitivity was evaluated considering different LES grid resolutions, observation locations, and sensitivity analysis methods. The robustness of these findings for onshore cases will be assessed by performing additional case studies.

To assure that the MMC efforts remain relevant to the wind industry, the team held three webinars with industry, both to present our most recent advances and to solicit feedback from industrial partners on their needs and where they see the most useful advances. In addition, MMC formed an industrial advisory panel, including six members that represent wind-plant developers, turbine manufacturers, and wind power forecasters. This panel is helping to plan an industry workshop to be held in 2020.

Finally, the team began the pivot toward studying MMC processes for the offshore environment during FY19. As stated above, the PIRT analysis identified the offshore environment as ripe for advance. As the team winds up the onshore efforts, the members are also beginning the process of identifying appropriate data, constructing machine-learning models of the offshore surface layer, testing fully coupled simulations for an offshore case, and using actuator disk codes to simulate turbines in both WRF-LES and Nalu-Wind. This planned initial case study will further inform where to focus resources to make the most important progress.

The MMC team continues to work collaboratively and has determined strategies to work through the remaining issues required to optimally provide coupled model simulations, including for the offshore environment. These simulations and advances in technologies will provide the wind industry new tools that can be used in the planning, design, layout, and optimization of wind plants, thus facilitating deploying higher capacities of wind generation.

Acronyms and Abbreviations

ABL	atmospheric boundary layer
AMS	American Meteorological Society
ANN	Artificial neural networks
AR	aspect ratio
CBWES	Columbia Basin Wind Energy Study
CPC	Cell Perturbation Case
CVFEM	control volume finite element method
DAP	Data Archive and Portal
DOE	Department of Energy
DRM	dynamic reconstruction model
EBVC	edge-based vertex-centered
ERF	Energy Research and Forecasting (model)
ESIG	Energy Systems Integration Group
GFS	Global Forecasting System
GLM	generalized linear model
HFM	High-Fidelity Modeling
IEC	International Electrotechnical Commission
LANL	Los Alamos National Laboratory
LBC	lateral boundary conditions
LES	large-eddy simulation
LLNL	Lawrence Livermore National Laboratory
LOS	line of sight
MMC	Mesoscale-to-Microscale Coupling
MOST	Monin-Obukov Similarity Theory
MY	Mellor-Yamada
MYNN	Mellor-Yamada-Nakanishi-Niino
NARR	North American Regional Reanalysis
NCAR	National Center for Atmospheric Research
NREL	National Renewable Energy Laboratory
NTC	Nonturbulent Case
PAT	profile assimilation technique
PBL	planetary boundary layer
PDF	Probability density functions
PIRT	Phenomena Identification and Ranking Table
PNNL	Pacific Northwest National Laboratory
POD	proper orthogonal decomposition

PPI	plan position indicator
RF	random forecast
RMSE	root-mean-square errors
RRTMG	Rapid Radiative Transfer Model for GCM [general circulation model]
RSFS	resolvable subfilter-scale
RWP	Radar Wind Profiler
SCPM	stochastic cell perturbation method
SGS	subgrid scale
SOWFA	Simulator fOr Wind Farm Applications
SWiFT	Scaled Wind Farm Technology
TC	Turbulent Case
TI	turbulence intensity
TKE	turbulent kinetic energy
TTU	Texas Tech University
UQ	uncertainty quantification
V&V	verification and validation
WRF	Weather Research and Forecasting

Contents

Figures

Contents

Contents

Tables

1.0 Introduction

1.1 Purpose of the Mesoscale-to-Microscale Coupling Project

The overall goal of the Mesoscale-to-Microscale Coupling (MMC) project is to improve coupling between mesoscale and microscale simulations via improved guidance and new strategies for setting up simulations and the development of new tools that can be used across the community. While significant progress was made during Phase 1, there remain a number of open science questions that are being addressed during Phase 2. This second phase will culminate in producing well-validated tools with the uncertainty quantified as well as validation cases that will be useful to industry. The project-specific objectives include:

- Apply rigorous verification and validation (V&V) techniques to the new modeling tools that are developed as part of the project to ensure the accuracy of our codes and results and develop estimates of the relative uncertainty.

- Improve computational performance of the coupled MMC models through the development of methods that can be used to reduce turbulence spin-up time and hence the size of computational domains.

- Improve representation of the surface layer in microscale models to enhance simulations of hub-height wind speed.

- Develop guidance for the community describing the best ways to couple mesoscale and microscale models, including specific spatial scales at which the handoff to the microscale model should occur.

- Prepare documentation and a suite of software tools that can be used across the community.

- Transition MMC research to the offshore environment.

As it is designed, the project addresses the significant technology barrier associated with the application of coupled modeling systems. Existing systems are complicated to evaluate and use; hence, the primary goal of this project is to help break down that barrier by providing guidance related to best practices, revised software tools, and evaluation data sets that can be used by the community. The technology maturation plan is straightforward and consists of documentation and tools described below that can be distributed to the community.

Realizing these objectives will enable simulation of the full suite of mesoscale and microscale flow characteristics affecting turbine and wind-plant uncertainties and performance, thereby allowing for substantive improvements in wind-plant design, operation, and performance projections. Figure 1.1 diagrams the MMC approach to the project and demonstrates the integration between the objectives. The work is grounded in data from field sites and experiments and culminates in new documentation, guidelines for best-practice model use, software tools, and data sets for testing.
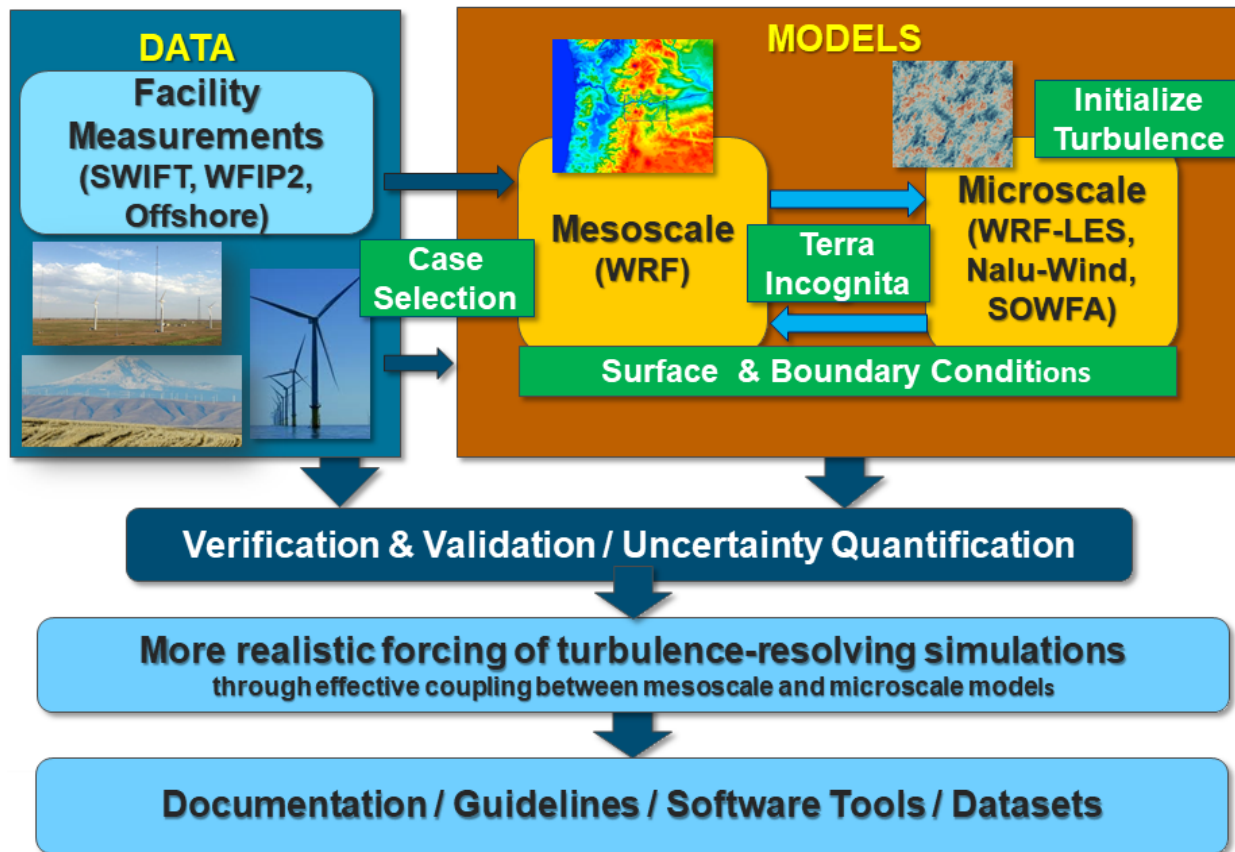
Figure 1.1. Diagram of the MMC project approach of using case studies to address the challenges of mesoscale-to-microscale wind-plant simulation challenges.

1.2 Motivation for Coupled Modeling

Coupling mesoscale (grid spacing on the order of kilometers) and microscale (grid spacing on the order of meters to tens of meters) models is an important step forward for the wind power industry. Appropriate techniques and tools are needed to better understand the turbulent wind flow into and within the wind plant, which impacts energy transfer between scales and, ultimately, the amount of energy available to harvest. The ability to couple these scales is particularly important for nonstationary meteorological conditions (such as frontal passages, thunderstorm outflows, baroclinic systems, and low-level jets) or when considering changes of atmospheric stability associated with the diurnal cycle. Improved estimates of the driving flow are needed to optimize wind-plant and turbine siting, design, and operation. During the first phase of the Atmosphere to Electrons (A2e) MMC project, important progress was made by our team in a number of key areas that are highlighted later in this section.

However, even with these advances, some significant challenges remain that include:
1) providing appropriate and consistent boundary and initial conditions; 2) bridging the so-called *terra incognita* (Wyngaard 2004)—that range of spatial scales between about 100 m and the depth of the boundary layer that is problematic for boundary-layer parameterizations applied in mesoscale models; 3) initializing turbulence at the correct spatial and temporal scales in the microscale models; 4) testing appropriate coupling methodologies; and 5) quantifying the uncertainty of the methods. The MMC team's integrated approach to addressing these challenges has been, and will continue to be, grounded in data. The team seeks to leverage

Department of Energy (DOE)-supported field studies, including at the Scaled Wind Farm Technology (SWiFT) facility site in Texas and the second Wind Forecast Improvement Project (WFIP 2) in the complex terrain of the Pacific Northwest, to select case studies that facilitate addressing the challenges. Through these case studies, the different approaches can be systematically tested and assessed using metrics specific to wind-plant operations. Figure 1.2 illustrates key elements of this approach.
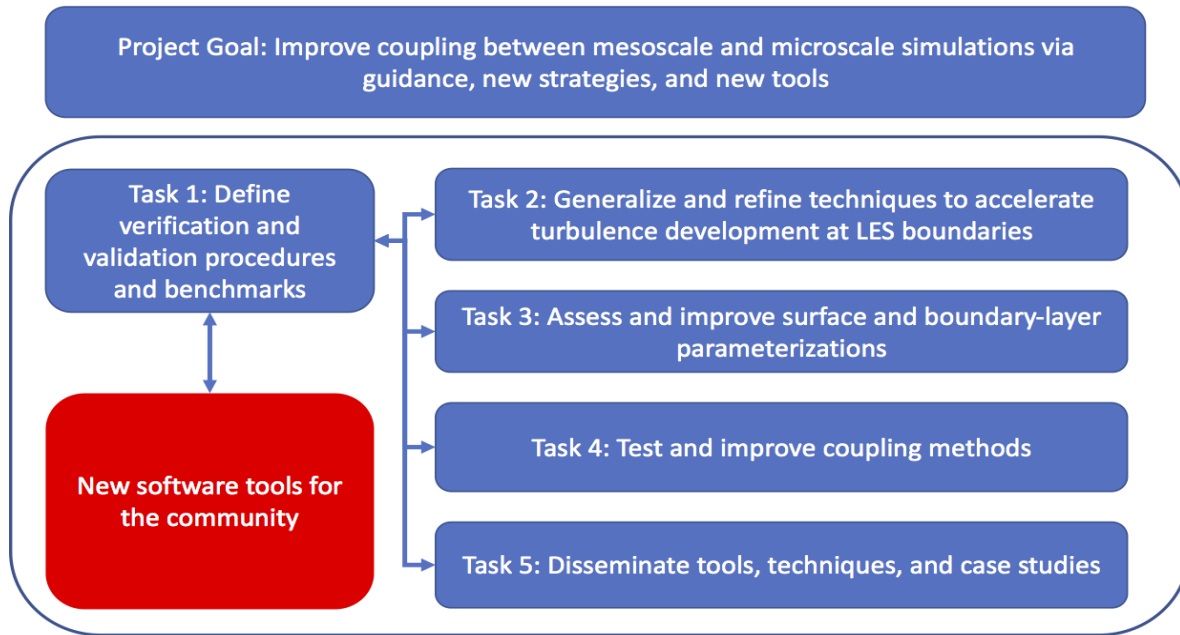
Figure 1.2.   Depiction of overarching project goal, tasks, and planned outcome.

1.3   MMC Project Context within the Atmosphere to Electrons Initiative

The A2e initiative is an effort within the Wind Energy Technologies Office of the U.S. Department of Energy's (DOE's) Energy Efficiency and Renewable Energy Office, whose goal is to optimize power production from wind plants as a whole. To that end, the initiative is explicitly integrating advances in atmospheric sciences, wind-plant aerodynamics, and wind-plant control technologies, taking advantage of current and emerging capabilities for high-performance computing. Because atmospheric inflow is the fuel that powers wind plants, containing both the energy available for conversion into electricity, as well as characteristics that modulate that conversion, the development and validation of first-principles based, high-fidelity physics models within an open-source simulation environment have been identified as a crucial part of A2e science goals and objectives. Furthermore, there has been an overwhelming consensus within the research community that these models must be developed and systematically validated using a formal verification and validation (V&V) process plus uncertainty quantification. The MMC project was intended to provide an initial demonstration of the V&V-guided approach to model development specifically applied to the mesoscale-microscale coupling problem and to provide the foundation for the ultimate selection of a common framework for the development of atmospheric and wind-plant modeling within the A2e initiative. It has been a joint collaborative project between DOE national laboratories, with National Center for Atmospheric Research

(NCAR) leadership as a subcontractor, and incorporating external feedback from A2e team members, the merit review panel, industry, DOE leadership, and other stakeholders.

The MMC project is grounded in data provided by other A2e facilities and projects. For the first two years, the data emphasized measurements taken at the SWiFT facility in West Texas. The MMC modeling helped characterize and inform the wake dynamics experiments being accomplished at that site and its results are expected to contribute to modeling wake dynamics. In years 3 and 4, the MMC project focused on coupled modeling in complex terrain, using data derived from observations taken in the Pacific Northwest as part of the A2e project, WFIP 2. Including mesoscale forcing in microscale models will also become critical to the success of the A2e project when focusing on wind-plant controls. Most prominently, the very specific coupling and modeling philosophies and technologies being developed by the MMC project are necessary for building the high-fidelity modeling tools that are needed by researchers and industry. The results of MMC modeling and case studies are being archived in DOE's Data Archive and Portal (DAP), and code is being provided via a team GitHub repository.

1.4   Progression of the MMC Project

During the first phase of the MMC project, our team made a number of significant accomplishments:

- Down-selected the mesoscale model to be the Weather Research and Forecasting (WRF) model and initiated plans to transition changes to the A2e Energy Research and Forecasting (ERF) model (via a separately funded project).

- Down-selected microscale model to Nalu, which is adopting the wind-plant modeling capabilities of Simulator fOr Wind Farm Applications (SOWFA) [in collaboration with the A2e High-Fidelity Modeling (HFM) project].

- Established metrics for verification and validation of these models relevant to wind-plant simulations and the coupling mechanism, including evaluating turbulence.

- Developed, tested, and evaluated various methods to couple mesoscale-to-microscale simulations, determining that online coupling is needed within WRF into the LES scales and that applying tendency mesoscale forcing in NREL's SOWFA allows the LES model to follow the nonstationary behavior of WRF for diurnal cycle cases in flat terrain.

- Developed, tested, and evaluated various methods of initializing turbulence in the microscale models that is subgrid to the mesoscale models, finding that perturbations that are a combination of temperature and momentum induce turbulence at the correct scales.

- Developed, tested, and evaluated methods to deal with spurious rolls resulting from models with grid spacing in the *terra incognita*. Showed that the upper end of the *terra incognita* is roughly equal to the boundary-layer depth. Found that in most cases it is possible to configure WRF to skip grid spacings in the *terra incognita*.

- Demonstrated and evaluated running coupled simulations for complex terrain associated with WFIP 2.

- Explored methods to better represent the surface layer in both mesoscale and microscale simulations.

These results were presented to the community through a series of articles in peer-reviewed literature (Rai et al. 2016, 2017, 2019; Mirocha et al. 2018; Haupt et al. 2019b; Rodrigo et al.

2016; Munoz-Esparza et al. 2015, 2018a; Quon et al. 2018); through presentations at conferences, including those of the American Meteorological Society, WindTech, Torque, Wind Energy Science, and International Conference on Energy and Meteorology; in PNNL technical reports (Haupt et al. 2015, 2017, 2019a); and a series of industry teleconferences. During the first phase of this project, the work emphasized atmospheric flow without including turbines. Much work remains, however, to develop and optimize a robust, fully coupled modeling system that can be used across industry.

Building on the first phase of the project, the next stages being undertaken in this phase are to develop, test, refine, validate, and disseminate specific MMC coupling strategies and technologies that can be used across industry as well as providing basic research results and enabling reduced-order modeling that can lead to innovative work in wind-plant siting, controls, and better understanding the impact of wakes on downstream turbines. Our team will provide detailed guidance based on our rigorous research experience and is building new high-performance-computing-based multiscale wind-plant simulation tools that couple a broad range of scales, including interactions across scales, which will enable the optimization required to ensure efficient, reliable production and integration of wind power. These tools will be applicable for diverse locations (both on and offshore) and operating conditions as required to support wind energy integration at high-penetration levels. The simulations will include not only the atmospheric flow, but also the wind plant/wake flow, broadening the modeling scope and increasing synergy with the A2e wake characterization and validation tasks. The results of the research in this project will provide essential input to the production of tools in the ERF and HFM tasks. Data and results of the modeling will be archived using the DAP. The tools will undergo thorough verification and validation and uncertainty quantification, via a series of observation-based case studies with increasing complexity in terms of nonstationarity, terrain, offshore influences, and inclusion of actual wind-plant field data.

1.5 Expected Impacts on Industry

The expected impact of the MMC project is to advance the science and engineering of coupled mesoscale-microscale modeling to provide industry with more advanced wind-plant optimization capabilities. Industry stakeholders have made it clear what must be done in terms of better modeling of power output. This issue is complex and involves many factors beyond applying a simple power curve to a simulated mean wind speed and making small adjustments for turbulence. Uncertainties come from many different aspects of the coupling, including interannual variability due to longer-term climatic variability, variability in the outer scales that are resolved by the mesoscale models, variability due to wake effects, inner variability due to the heterogeneity within the wind plant, variability due to coherent structures, inherent uncertainty due to the chaotic nature of turbulent flow, and, finally, impacts through the surface-layer treatment and its interactions with characteristics of the underlying surface. The MMC project addresses these issues directly and, over the course of the multiyear project, will be able to provide specific guidance to industry. The MMC team developed Table 1.1 as a list of uses of the MMC approach, the stakeholder(s), quantities and metrics to assess for each use, and the type of uncertainty analysis that will affect power output.

Table 1.1.Assessment of stakeholder use and assessment strategies to determine if MMC modeling provides useful information for that use.

MMC Use	Stakeholder	Quantity to Measure	Metrics	Uncertainty Analysis for Power Curve
Basic understanding of physics	Scientists, Engineers	Basic metrics plus elevated structures	Current list plus below	Ensembles—physics, initial and boundary conditions
Micrositing	Developers, Contractors, Manufacturers	Binned wind speed, spectra, spatial variability	Probability structures and spatial correlations	Distributions, correlations, spatial correlations, covariance
Turbine siting	Developers, Contractors, Manufacturers	Binned wind speed, spectra, spatial variability	Probability structures and spatial correlations	Distributions, correlations, spatial correlations, covariance
Turbine reliability and design plus forensics		Turbine statistics, shear, coherent structures	Correlated structures to loads	Distribution extremes, wind direction variability
Operations and managements, controls, loads		Slow variations, event variations, binned wind speed, accurate turbulence statistics plus characterization of structures	Use spatial and temporal filters	Time-dependent statistics and variability
Inform low-order models: mass conserving models, Reynolds- averaged Navier-Stokes	Developers, contractors, original equipment manufacturers	3D wind speed, turbulent kinetic energy, and surface fluxes	Spatial correlations	All

Both the improved computational methodologies and the knowledge gained through their assessment and validation will enable substantive improvements in wind-plant design, operation, and performance projections, all of which are required to attract continued investment in wind power as a viable means of meeting national goals of mitigating climate change and establishing energy independence.

The successful outcome of the MMC project will result in improved computer simulation capability that accurately incorporates the impact of mesoscale weather on wind-plant performance. Meeting this goal will require microscale simulations driven by realistic mesoscale forcing, knowledge of when the additional complexity of mesoscale coupling is beneficial, and recommendations for best practices for modeling across spatial and temporal scales. Over the course of this project, the tools and knowledge developed during each phase, outlined above, will continue to be made available to industry and the broader research community.

The MMC team has engaged with industry by participating in the first-year workshop, held in September 2015 at NCAR, at which industry representatives were invited to comment on the approach and results as well as to suggest changes. In FY16, the MMC team conducted an industry survey. During FY17, the team conducted a first telecom with industry to inform them of our progress and solicit input. During FY19, three more teleconferences with industry

(September 20, 2018, and February 14 and April 18, 2019) demonstrated industry's interest in the team's research results. The team also formed an industry advisory panel consisting of:

- Mark Ahlstrom, NextEra, Energy Systems Integration Group (ESIG) President

- Greg Oxley, Envision Energy

- Lawrence Cheung, GE Global Research, US

- Samuel Davoust, GE Renewables

- Line Gulstadt, Vestas

- Philippe Beaucage, UL/AWS Truepower

This advisory committee is helping us to plan and lead an industry workshop in FY20.

MMC team members have also been actively engaged in organizing and presenting papers at major wind industry conferences that were used as forums for bringing the research community together with industry during FY19. This was successfully accomplished at the International Conference on Energy and Meteorology held in Lyngby, Denmark in June 2019; the Tenth Conference on Weather, Climate, and the New Energy Economy held as part of the American Meteorological Society (AMS) Annual Meeting in Phoenix, AZ in January 2019; the American Institute of Aeronautics and Astronautics in January 2019; at the Wind Energy Science Conference in Cork, Ireland in June 2019; and at North American Wind Energy Academy (NAWEA)/WindTech in Amherst, MA in October 2019. All of these meetings included presentations about the MMC project and afforded ample opportunity for industry representatives and team members to discuss the team's progress and plans. As described in more detail in the sections that follow, each of the models and techniques we used are validated against a range of metrics to determine their accuracy for a mix of wind-energy-related applications. *A key outcome of this project is concrete guidance to both industry and research communities regarding the potential strengths and weaknesses of various MMC approaches.* Additionally, the best performing of the approaches assessed will be incorporated into the A2e High-Performance Modeling environment for future design and testing. A set of metrics defined by the project continues to be refined further as the project progresses into additional realms of modeling.

During FY19, the team moved toward a more distributed management structure to better facilitate teamwork across laboratories. The lab leads and NCAR principal investigator and chief scientist formed an executive committee. Each committee member was assigned a team leadership position. Between the biweekly full team teleconferences, the task-based teams would communicate on the specifics of their efforts. Several all-team workshops were held—in January and April 2019—which further facilitated face-to-face communication and planning details of the work.

1.6   Report Contents and Organization

The remainder of this report provides detailed documentation of the results of the MMC project's FY19 effort. The performance metrics were defined at the beginning of the project and updated as needed to assess the phenomena mentioned above. The need for uncertainty quantification has been an intentional part of the metrics development and plans for model runs in the future.

During FY19, the MMC generated a Phenomenon Identification and Ranking Table (PIRT) to determine the most important issues to address in our future research. The PIRT is presented

and discussed in Chapter 2.0. Chapter 3.0 documents the benchmark cases studied during FY19 and Chapter 4.0 describes the methods planned for assessment and the movement toward using common Python tools in Jupyter notebooks and sharing these tools in a team repository. The mesoscale modeling for case days is reported in Chapter 5.0. The results of team efforts to rigorously compare coupling methods appear in Chapter 6.0. Chapter 7.0 reports on efforts to rigorously compare methods of generating turbulence in the microscale simulations. The team also considered best ways to improve our models of near-surface physics in FY19, including machine-learning approaches as well as physics methods, as described in Chapter 8.0. Chapter 9.0 reports on quantifying uncertainty using a parametric approach. A lidar simulator was constructed and tested during FY19, as reported in Chapter 10.0. Chapter 11.0 compares the A2e HFM model, Nalu-Wind, to the other microscale models considered at the beginning of the MMC project and reported in Mirocha et al. (2018). Chapter 12.0 synthesizes the results and their expected impact. Appendix A lists the team's FY19 contributions to the peer-reviewed literature and conference papers presented. Appendix B details each lab's contributions to the FY19 efforts.

2.0 Mesoscale-Microscale Phenomena Identification and Ranking Table

2.1 Background

In FY19, members of the A2e MMC team created an MMC-specific PIRT. The PIRT is a tool to help in prioritizing which aspects of the modeling and simulation framework require research and development. The one constructed in FY19 for MMC builds on the mesoscale PIRT developed during the 2015 A2e ModSim planning meetings.

The MMC PIRT is structured such that it corresponds to the following three classes of locations: 1) flat onshore sites, 2) complex terrain onshore sites, and 3) offshore sites. For each of these locations, there are two classes of phenomena considered: mesoscale and microscale/wind-plant scale phenomena.

For all three location classes, the microscale/wind-plant-scale phenomena considered are the same, but the key mesoscale phenomena vary with location. The rationale is that, in general, no matter where a wind plant is located, it reacts to the winds within the atmospheric boundary layer (or for very shallow boundary layers, the turbines will also react to the winds just above the boundary layer). On the other hand, the mesoscale weather patterns driving the wind resource vary greatly from location to location. For example, the eastern coast of the United States is prone to hurricanes, a type of mesoscale forcing, but the complex terrain of the central Rocky Mountains of the United States is not.

In the end, a table is created with scores that indicate priority level for the research and development of modeling and simulation methods for each listed phenomenon. The table is shown below in the discussion section, but first we discuss how the rankings are created.

2.2 Ranking Method

Rankings are performed for the following categories:

- Importance at application level
- Model adequacy
- Physics understanding
- Adequacy of physics in code
- Level of validation
- Ability to transfer relevant phenomena between scales.

2.2.1 Importance at Application Level

The "Importance at Application Level" ranking category addresses how important the phenomena are in the application of mesoscale-microscale coupling. Here, the main application is to computationally simulate wind-plant aerodynamics using high-fidelity turbulence-resolving methods such as large-eddy simulation. We want to be able to simulate full wind plants under the most realistic atmospheric conditions possible where the turbines are represented using a

spectrum of models ranging from actuator disks to full geometry-resolved computations. The purposes of such simulations include: 1) gaining a better physical understanding of wind-plant flows and wind-plant response to the flow, 2) testing new wind-plant optimization ideas under realistic atmospheric conditions, 3) performing "forensic" analysis on existing wind plants exhibiting unexpected performance, and 4) high-resolution forecasting of wind-plant power production.

2.2.2 Physics Understanding

The "Physics Understanding" ranking category simply addresses how well we understand the physics driving the particular phenomena. For example, the physics of how large wind plants affect mesoscale weather is not well understood.

2.2.3 Adequacy of Physics in Code

The "Adequacy of Physics in Code" ranking addresses how well the real physics is modeled and implemented within the computational tool. For example, perhaps the physics are well understood, but they are complex physics that are difficult to replicate computationally or require prohibitively high resolution. In that case, models of the physics may not be adequate or may perform poorly at normal resolutions. An example of this is stratus-topped atmospheric boundary layers, for which the physics are well understood but the resolution requirement to resolve the sharp cloud top-free atmosphere interface is very high.

2.2.4 Level of Validation

Once a phenomenon is modeled in a code, the results of the model should be compared to high-quality data to validate the model. Low scores of "Level of Validation" mean that either there are little data from which to perform validation, or that validation has not been performed with existing data to the extent required.

2.2.5 Ability to Transfer Relevant Phenomena Between Scales

The "Ability to Transfer Relevant Phenomena Between Scales" ranking is especially pertinent to MMC work, which wishes to bridge the mesoscale and microscale/wind-plant scale. For example, if we wish to determine how a hurricane traveling along the Atlantic coast of the United States may affect a wind plant comprised of some proposed 20-megawatt, very large, very flexible wind turbines, we may need to model that hurricane with the mesoscale model and then transfer the relevant information about that hurricane to the microscale/wind-plant aerodynamics simulation tool. This ranking category addresses how well we can currently do this.

2.2.6 Ranking Method

All categories are scored on a 0-3 scale, in which 0 means unimportant or inadequate, and 3 means the category is of the highest importance or adequacy. We then assign a planning priority number which is calculated by:

$$p = \frac{(app\ level\ importance\ -\ model\ adequacy)\ +\ 3}{2} \tag{2.1}$$

where *p* is the planning priority. This equation simply compares the difference in phenomena importance at the application level and model adequacy and rescales it to fall on a 0-3 scale.

For example, in the extreme, if a phenomenon is of highest importance (ranking = 3), but the model is completely inadequate (ranking = 0), then p = 3, meaning that work to improve the modeling of this phenomenon should be of highest importance. On the other hand, if a phenomenon is not important at all, and the model is very adequate, then p = 0, meaning that work to improve the modeling of this phenomenon is not important.

2.3 Discussion

Figure 2.1 summarizes the mesoscale-to-microscale-coupling PIRT. The rows correspond to different phenomena and are grouped into the mesoscale and microscale/plant-scale phenomena. Three columns provide the planning priority for each phenomenon for each location: flat onshore, complex terrain onshore, and offshore. The priorities are numerically ranked on a scale of 0 to 3 as outlined above, and they are color coded to visually highlight the priority. The darker the shade of gray highlighting, the higher is the priority. Not all mesoscale phenomena have a priority ranking for each location because they do not necessarily occur in all locations. The far-right column represents the mean of the rankings for each phenomenon over all locations, which provides an overall sense of how much priority each phenomenon is allocated. The last two rows give the sum and mean of the rankings of all phenomena by location, presenting a general idea of how much priority is placed on the set of all phenomena for a given location.

Overall, the mean of all prioritizations in order of highest-to-lowest priority is offshore, flat onshore, and complex terrain onshore. This is a somewhat surprising result because we would have expected complex terrain onshore to rank as having overall higher research and development priority over flat onshore. We expect that offshore would rank highly because it is one of the less researched areas in terms of MMC and contains complex air-sea interaction physics that are difficult to model. However, upon further inspection, we see that certain phenomena, including low-level jets, land-sea breezes, and interplant interactions are as equally applicable onshore in flat terrain as offshore. These rankings help us to realize that there are still many challenges, even for onshore flat terrain, and that researchers have not even mastered the diurnal cycle, which is something so commonplace that most onshore wind plants experience it every day. Nonequilibrium atmospheric turbulence is the norm over flat terrain, and it is an area of microscale research that is largely untouched. Thus, the offshore and complex terrain onshore locations have more varied mesoscale phenomena to consider so the number of different research challenges is greater.

Overall, high-priority mesoscale phenomena include low-level jets, land-sea breezes, weather fronts, tropical cyclones, Nor'easters, and thermal pooling and terrain-gap flows. High-priority microscale/wind-plant scale flows include icing and precipitation, surface energy and momentum exchange, air-water-wave interactions, and roughness and canopy effects. Surprisingly, icing and precipitation are ranked high priority, but this is because liquid precipitation can cause wind-turbine blade erosion, a particular problem offshore, and freezing precipitation leading to blade icing can cause a need for curtailment.

Although this PIRT is illuminating and definitely can guide decision making, there are reasons to be cautious. Importantly, the process of creating a PIRT is unavoidably subjective. It requires a set of experts coming to consensus using their knowledge and best judgement. In creating these rankings, there was a requirement of consensus among a group large enough and with sufficiently varied background to attempt to reduce the subjectivity. Equally important is that this PIRT is meant to be fairly general, but every researcher or engineer makes decisions based upon his or her specific application. The application space is vast because of wind energy's

highly interdisciplinary nature. Examples include short-term wind power forecasting, grid integration studies, detailed structural analysis of a particular turbine design (fixed or floating) subject to turbulence specific to its location, and forensic analysis of wake effects within an entire wind plant. If a researcher is dealing with a specific application and needs guidance on which phenomena to prioritize and how, she or he really should perform a PIRT ranking specific to the application and use this general PIRT as a guide and for reference.

PIRT for Mesoscale-Microscale Coupling

Phenomenon	Relevant in Model	Planning Priority			
Mesoscale Phenomena	Offshore	Flat Onshore	Complex Onshore	Offshore	mean
Low-level jets		2.00			2.00
Cold fronts	2	1.88	1.88	1.88	1.88
Warm fronts	2	1.38	1.88	1.88	1.71
Canonical diurnal cycle	2	1.88		0.88	1.38
Thunderstorm outflow		1.88			1.88
Severe weather	1	1.25	1.63	1.63	1.50
Large-scale wind die-off/stabilization		1.13			1.13
Land-sea or land-lake breezes	2	2.00	1.88	1.88	1.92
Mountain waves			1.50		1.50
Hydraulic jumps			0.88		0.88
Terrain-induced cold pools			1.88		1.88
Mountain wakes			1.88		1.88
Thermal and/or lee troughs			0.88		0.88
Terrain gap flows			1.88		1.88
Diurnal valley-driven flows			1.75		1.75
Tropical cyclones	1			2.25	2.25
Noreasters	1			2.13	2.13
Coastal low-level jet	2			2.00	2.00
High pressure with subsidence	3			0.63	0.63
Persistent stratus-topped boundary layer	2			1.50	1.50
Plant Scale Phenomena	Offshore	Flat Onshore	Complex Onshore	Offshore	
Icing and Precipitation: drop size distribution, type of precip.	0	2.13	2.13	2.13	2.13
Influence on mean atmospheric boundary layer structure	1	1.75	1.75	1.75	1.75
Turbulence consistent with larger-scale forcing	2	2.00	2.13	2.13	2.08
Surface energy exchange under realistic mesoscale forcing (moisture)	2	2.13	2.25	2.38	2.25
Wind plant effect on mesoscale flow	1	2.13	1.63	2.13	1.96
Surface features and physics of relevance (roughness, canopy)	1	2.13	2.25	2.13	2.17
Terrain-induced Flow Phenomena (complex terrain)	1	1.88	2.25	2.13	2.08
Urban-environment-induced flow phenomena	1	1.38	1.38	1.50	1.42
Large-scale forcings (geostrophic and advective)	2	2.00	2.00	2.00	2.00
Air-sea interaction (offshore)	1	1.88	1.50	2.38	1.92
sum		32.75	37.13	37.25	
mean		1.82	1.77	1.86	

Figure 2.1. The summary rankings of the mesoscale-to-microscale-coupling PIRT. Note that this summary does not include the rankings for each criterion. The full mesoscale-to-microscale-coupling PIRT is available upon request.

Last, when a researcher chooses a specific phenomenon that ranks high priority upon which to perform research and development, he or she should look at the full ranking and understand why that phenomenon received a high-priority ranking. For example, a ranking could be high priority because the physics are not well understood and require further study, the current

physics model for the phenomenon is known not to duplicate the real physics well even though the physics are well understood, the model is adequate but requires unreasonable numerical resolution, or that the model behavior is simply unquantified because it has not been well validated.

3.0 Case Selection

As seen in Chapter 1.0, the MMC project seeks to improve models through assessing their capabilities for reproducing the specific characteristics of particular case days. During FY19, the team looked at advances in both complex terrain cases and in nonstationary flat terrain cases. The case days are described as follows.

3.1 Canonical Diurnal Case in Flat Terrain – Nov. 8, 2013 SWiFT Site

To assess the ability of the coupled models to capture more canonical diurnal changes as one progresses through a typical day, it is convenient to use data from a flat terrain site. To that end, the team has considered a case day from measurements taken at the DOE/Sandia National Laboratories SWiFT facility in West Texas. The SWiFT site was chosen for its flat terrain, relevance to wind energy installations in the United States and the adjacent atmospheric measurement facilities hosted by Texas Tech University's (TTU's) National Wind Institute. More details of the SWiFT site are documented in the team's Year 2 report (Haupt et al. 2017) and in the report by Sandia National Laboratories regarding that site (Kelley and Ennis 2016).

The team selected November 8, 2013, as the primary diurnal cycle case to model because it represented a day that included typical morning and evening transitions and made a good first test case with common conditions that were important for wind energy. This is the same day studied earlier in the Years 2 and 3 reports. The 1-hour, near-neutral transition is centered around 22:30 UTC. The diurnal cycle, convective-neutral-stable atmospheric transition are centered on the near-neutral transition.

This period was marked by strong southwesterly winds over the Texas Panhandle and generally clear conditions and the winds at the lowest altitudes are consistently south-southwesterly over the course of the day.

3.2 Complex Terrain Cases

In this work, two real case simulations in complex terrain for unstable conditions were performed using multiple one-way nested domains in the WRF model. The simulations were run for parametric quantification of uncertainty (Chapter 9.0) for the lidar simulator (Chapter 10.0). The location chosen for the simulation was the WFIP 2 site near the Columbia River Gorge in Oregon. The candidate dates were selected from a five-month period from May through September 2016, during the intensive portion of the WFIP 2 field campaign. The candidate dates required lidar data to be available for more than 70% of the 5-km radius. This condition provided 36 days for the unstable case (with period 18:00–21:00 UTC). Furthermore, other conditions, such as fair weather (no clouds), westerly wind, and moderate heat flux and wind speed (~200 W/m^2 and ~8 m/s), were also used to search the candidate dates. Finally, August 21, 2016 was found to be the best candidate date. Mesoscale simulation was performed using different reanalysis data—the North American Regional Reanalysis (NARR) and the Global Forecasting System (GFS)—in the WRF model to evaluate the wind magnitude and direction during the unstable period. The NARR forcing resulted in a consistent wind speed compared to the GFS forcing over the three hours of window. Therefore, NARR data were chosen to provide forcing in the mesoscale domain, which nests an LES domain inside in the WRF model.

4.0   Common Methodologies and Tools

In the fifth year of the MMC project, the team has worked to streamline our simulation and analysis workflows, to centralize our code development efforts, and to add transparency and reproducibility to our assessment exercises. To engage with industry and the academic community, we also look toward disseminating a collection of validated, regularly maintained, and version-controlled MMC capabilities. For these reasons, we have created the "A2e: Mesoscale-to-Microscale Coupling" GitHub organization (github.com/a2e-mmc) to serve as a living archive of codes to be used in analysis, assessment, and reporting. The current repositories include:

- **mmctools**: Python-based tools for data standardization, simulation, and analysis

- **assessment**: Results of data (measured and simulated) processing and analyses stored in Jupyter notebooks, i.e., Python code with embedded output and figures

- **WRF**: Central version of the Weather Research Forecast model to contain all MMC-related modifications

- **WRF-setups**: WRF input decks for MMC case studies

- **SOWFA-setups**: SOWFA input decks for MMC case studies.

The analysis codes developed in this repository are written in Python 3. Code is expected to adhere to PEP 8 style guidelines as much as possible to deliver clean, familiar code to all users of Python. In this way, we strive to allow MMC researchers with minimal Python coding experience to read, understand, and develop codes of their own. All code should be usable in, and demonstrated by, Jupyter notebooks. This is a familiar medium for many Python users that combines code with inline code output (including figures) in a natural format. Examples for usage have been added to the assessment repository.

4.1   "mmctools" Repository

These tools are intended to:

1. Enable general offline-coupled mesoscale-to-microscale simulation between a variety of mesoscale and microscale solvers

2. Standardize output from simulations and observational data

3. Facilitate the analysis, assessment, and reporting of MMC results.

The layout of the mmctools repository is illustrated in Figure 4.1.
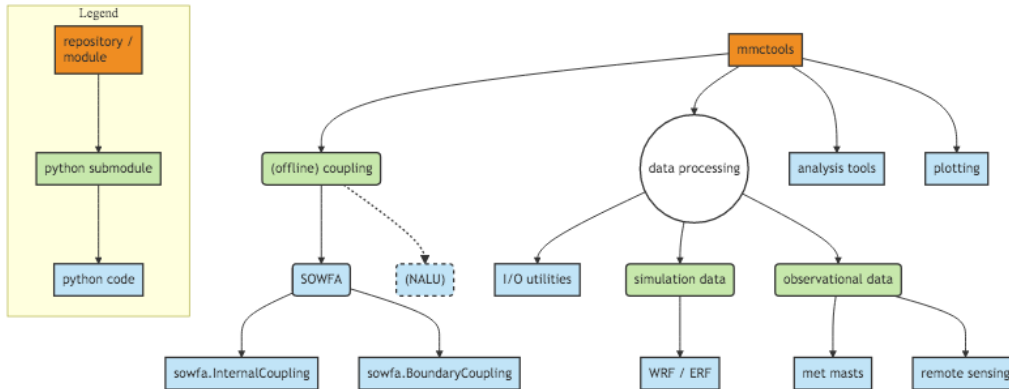
Figure 4.1.   Organizational structure of the A2e-MMC "mmctools" Python code repository.

4.1.1   Offline coupling

For offline coupling methods, the interface codes should automatically translate the outputs from the mesoscale solver into inputs to the microscale solver. Once the MMC methods have been verified, other researchers (both internal and external to the MMC team) should not have to manually repeat this process. To this end, we aim to make the coupling process as straightforward as possible to consistently reproduce expected results and also minimize user error. For example, to set up an offline, internally coupled simulation driven by time-height mesoscale data in the SOWFA microscale solver, a sample code snippet that an end user may write might look like this:

```python
from mmctools.coupling.sowfa import InternalCoupling
to_sowfa = InternalCoupling(output_directory,
  dataframe_with_driving_data,
  dateref='YYYY-MM-DD HH:MM', # t=0 in simulation
  datefrom='YYYY-MM-DD HH:MM', # output range
  dateto='YYYY-MM-DD HH:MM')
# create internal source terms, f(t,z), from a time-height series
to_sowfa.write_timeheight('forcingTable')
# create initial vertical profile, f(z)
to_sowfa.write_ICs('initialValues')
```

The InternalCoupling class will be responsible for processing the standardized data and generally should not require modification from case to case. Similarly, for boundary coupling in SOWFA:

```python
from mmctools.coupling.sowfa import BoundaryCoupling
to_sowfa = BoundaryCoupling(output_directory,
  xarray_with_driving_data,
  dateref='YYYY-MM-DD HH:MM', # t=0 in simulation
  datefrom='YYYY-MM-DD HH:MM', # output range
  dateto='YYYY-MM-DD HH:MM')
# create inflow planes, e.g., f(t,y,z) or f(t,x,z)
to_sowfa.write_boundarydata()
# create initial field, f(x,y,z)
to_sowfa.write_solution(t=datefrom)
```

4.1.2   Data standardization

Data standardization and analysis activities have included the identification and application of several MMC-preferred Python data structures and analysis tools (packages), the development of data processing tools for ingestion of MMC-centric model results and observational data into standardized Python-object data structures, and development of analysis and plotting utilities for use in assessment activities of standardized data.

Two well-known Python packages have been adopted in the development of the mmctools capabilities for MMC-related data science workflows. These are the Series/Dataframe data structures of the pandas package (https://pandas.pydata.org/pandas-docs/stable/reference/api/pandas.DataFrame.html) and the DataArray/Dataset data structures, of the closely related xarray package (http://xarray.pydata.org/en/stable/data-structures.html).

The standardized content for all processed data (both observation and simulation data sets) was formulated intentionally with assessment needs in mind. All standardized data sets include a specified set of variables, with consistent units, and naming conventions. After being standardized, any data set may be read into an assessment notebook for analysis.

Raw data from the A2e DAP may exist in a variety of formats and be organized into different directory structures. To provide a convenient and repeatable framework for creating new data sets, a library of data readers has been developed to streamline the loading of data from a variety of sources. These sources include met mast observations and remote sensing products. Additional tools are under development to process simulation data as well. Once the data have been loaded into memory, they may be easily manipulated (e.g., unit conversions, calculation of derived quantities) and then written out in a standardized data format.

A sample code snippet illustrating the data loading process looks like this:

```
from mmctools.dataloaders import read_dir
from mmctools.measurements.radar import profiler
# read selected files within a directory and concatenate into dataframe
df = read_dir(dpath, file_filter='*_w*', reader=profiler)
```

4.1.3   Data analysis

Two main utility libraries have been developed. First is a plotting library, which takes data loaded in the manner described above and generates near-publication-quality figures with a single command. As a result, all figures used in MMC reporting will have a consistent look and feel. The library also greatly facilitates the use of Python plotting tools and will also facilitate internal discussions and comparisons of results because the data processing and presentation are performed identically. Available plotting functions for comparing one or more data sets include:

- Time-history plots at selected heights
- Time-height plots
- Profile plots at selected times
- Spectra plots for selected time periods.

A library of helper functions has also been developed. The objective is to minimize time spent reinventing the proverbial wheel. Commonly calculated quantities (e.g., covariances, turbulence intensity, power spectral density) can be calculated consistently under the same assumptions. In addition, common meteorological functions and empirical models have also been added to the library. Having a centralized set of functions enables cleaner analyses with fewer calculation errors. These may be used, for example, to estimate virtual temperature from air temperature, pressure, and relative humidity.

4.2   The "assessment" Repository

Throughout the past year, several members of the MMC team collaborated to determine best practices for thorough model comparison and assessment. Discussions resulted in a three-step process: ingest/standardize the data, model evaluation, and evaluation synthesis. The data readers described above in the data standardization step ingest and process the data into a specific pandas or xarray data structure with consistent data field content, units, and naming conventions. Jupyter notebooks in this repository provide a means of evaluating each individual modeling effort in a synergistic manner by producing figures, plots, and statistics using the mmctools utilities. All modelers have been encouraged to use the assessment notebooks as defined evaluation recipes (in the context of this collaborative project) for model results as each team member progresses through his or her research activities. The notebooks provide uniform, publication-ready figures, and reduced assessment metric data sets automatically saved for sharing amongst project participants. Fundamentally, the notebooks simplify the process of synthesizing model results by producing equivalent plots, figures, and statistics for intercomparison against disparate MMC approaches and observations where applicable. Moreover, they provide a transparent and easily accessible means of documenting our analyses with code and discussions saved inline with the analysis products.

The assessment repository contains the results of our data standardization and MMC assessment efforts, as well as accompanying higher-level code. Contents include:

- Notebooks and codes to produce standardized data sets from observations and simulations, ready to use for driving and validating MMC simulations

- Analyses of observations and simulations performed for studies within the MMC project

- Notebooks to produce figures for MMC publications

- Examples of data processing and analysis procedures.

These contents will exclude actual data, only including the code necessary to generate each data set as to keep the git repository lightweight. Actual data products should be uploaded to the DAP or some other suitable data repository. The layout of the assessment repository is illustrated in Figure 4.2.
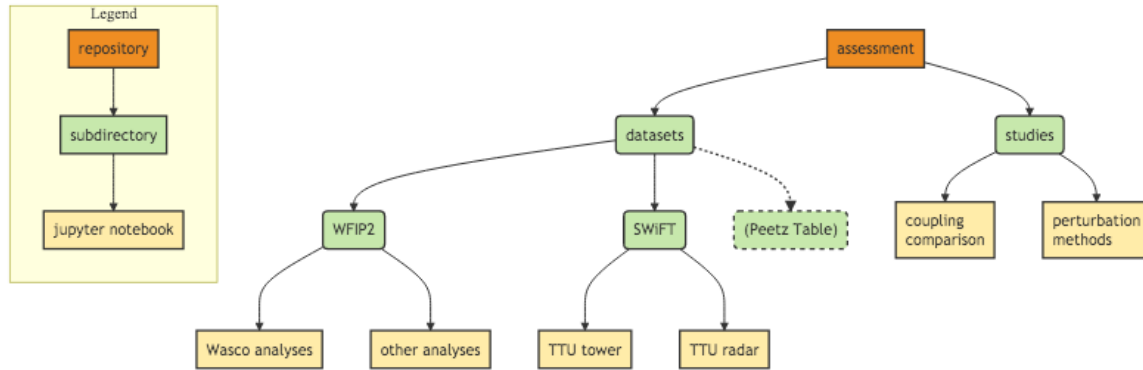
Figure 4.2. Organizational structure of the A2e-MMC "assessment" Jupyter notebooks repository.

4.3   WRF Repository

To work toward our goal of reproducible and easily disseminated MMC tools, we have created a central version of WRF within the A2e-MMC GitHub organization. To facilitate comparisons between WRF modelers within the MMC team, and for reproducibility of results, we expect modelers to use this version for ongoing and future research efforts. This is also the version to which MMC developers should contribute new features so that all team members will have access to the same capabilities developed by others. Moreover, when interacting with research partners in the future, we will have to only deliver a single version of the mesoscale solver.

The A2e-MMC version of WRF has been forked from the NCAR repository (at github.com/wrf-model/WRF) from release version 4.1. The A2e-MMC repository is set up to track the upstream NCAR repository so that new releases may be directly merged into our code base.

4.4   "WRF-setups" Repository

This is an archive of the input files used in completed WRF simulations for MMC studies. Instead of retaining all working WRF files, we keep only the files in the input deck that are needed to generate all other input files (e.g., boundary and initial conditions). For convenience, a shell setup script has been provided that will download reanalysis data for the specified simulation days, run WPS for those dates, then set up submission scripts for WRF to be executed in a high-performance computing environment.

4.5   "SOWFA-setups" Repository

This is an archive of the input files used in completed SOWFA simulations for MMC studies. Similar to the WRF-setups repository, instead of retaining all working files, we keep only the SOWFA input files that are needed to generate all other input files (e.g., blockMesh, topoSet, and refineMesh input dictionaries). The directory structure should mirror the exampleCases directories provided with SOWFA and SOWFA-6.

5.0 Mesoscale Modeling for MMC

5.1 Advancing the 3D PBL Parameterization

Accurate characterization of the wind resource and wind power predictions over heterogeneous surfaces and in complex terrain requires resolving land-use and terrain effects on the flow. In numerical weather prediction models, turbulent stresses and fluxes are commonly parameterized using one-dimensional planetary boundary layer (1D PBL) parameterizations based on the assumption of horizontal homogeneity. Such parameterizations do not include horizontal gradients of turbulent stresses and fluxes and thus cannot accurately represent terrain effects as the grid-cell size decreases. We therefore developed and implemented a 3D PBL parameterization in the WRF model to account for 3D effects on turbulence kinetic energy (TKE) and turbulent stresses and fluxes. The 3D PBL parameterization is an algebraic stress and flux parameterization based on the developments of Mellor and Yamada (1974, 1982). The parameterization involves solving a system of 13 linear algebraic equations at each grid cell for turbulent stresses and fluxes. Once all 6 components of turbulent stresses and 3 components of turbulent fluxes are available, the full divergences of stresses and fluxes are computed and added to the right-hand side of the prognostic equations for momentum, potential temperature, and water vapor mixing ratio. The development of the 3D PBL parameterization started under the WFIP 2 project and continues under the MMC project. Under the WFIP 2 project, we implemented the Level 2 parameterization according to Mellor and Yamada (1982) in WRF, where the TKE is diagnosed. During FY19 under the MMC project we ported the code to a more recent version of WRF (version 4.0.3) and expanded it to include a prognostic equation for TKE. Furthermore, we developed surface boundary conditions that are consistent with the turbulence closure.

During the WFIP 2 project, we carried out LES over the domain of the WFIP 2 field study. The output of these LES was compared to mesoscale simulations and validated using observations. The two domains of LES simulation are shown in Figure 5.1. Considering that the WFIP 2 observations are relatively sparse and thus not suitable for validation of all the components of the 3D PBL parameterization, we therefore used validated LES to assess the 3D PBL parameterization. As a first step, we used LES results to estimate the relative importance of horizontal velocity gradients in comparison to vertical velocity gradients. Since the focus was on the relative importance of horizontal shear on the boundary layer structure and, in particular, its relevance for wind power forecasting, only the first 10 grid cells (approximately 120 m above the surface) were used in this analysis. For this purpose, we analyzed LES output saved every three minutes between 20:00 and 21:00 UTC for March 7, 2016, and used only the east half of the LES domain, 90 km x 90 km, resolved using 3000 x 3000 grid cells (denoted by the red rectangle in Figure 5.1).
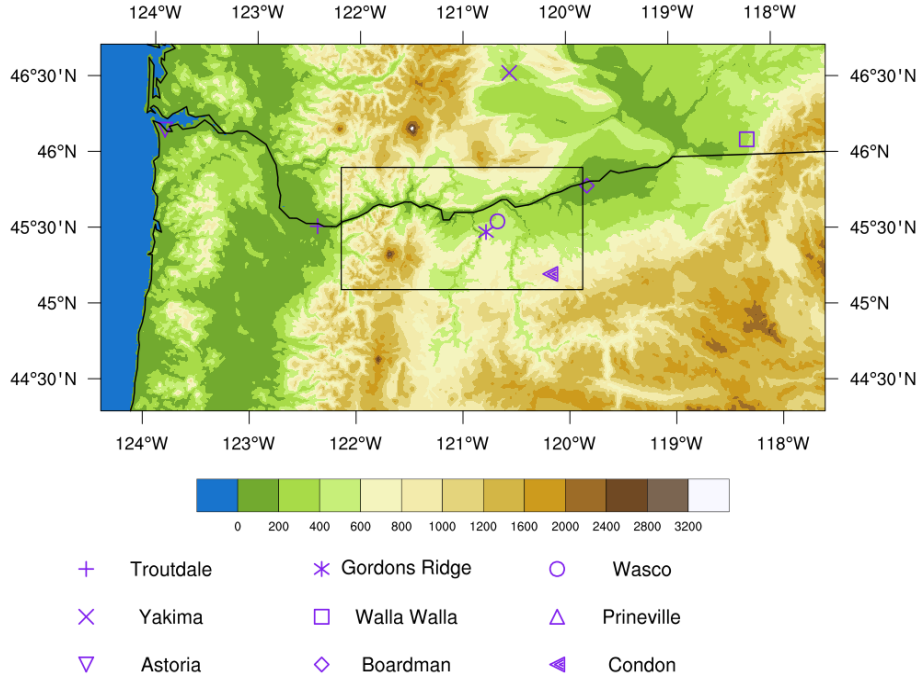
Figure 5.1. Parent and child (black rectangle) domains of the LES corresponding to March 7 and 8, 2016, of the WFIP 2 field study. The grid cell size of the parent/child domain was 90/30 m. The red square is the part of the child domain used in the analysis presented here.

To assess the relative importance of horizontal gradients in comparison to vertical gradients, we computed the following ratio:

$$R = \left[\frac{\left(\frac{\partial u}{\partial x}\right)^2 + \left(\frac{\partial u}{\partial y}\right)^2 + \left(\frac{\partial v}{\partial x}\right)^2 + \left(\frac{\partial v}{\partial y}\right)^2}{\left(\frac{\partial u}{\partial z}\right)^2 + \left(\frac{\partial v}{\partial z}\right)^2} \right]^{\frac{1}{2}} \qquad (5.1)$$

Here, horizontal derivatives of the streamwise velocity components are computed as:

$$\frac{\partial u}{\partial x} = \frac{\partial u}{\partial x'} + \frac{\partial z'}{\partial x'}\frac{\partial u}{\partial z'} \qquad (5.2)$$

and

$$\frac{\partial u}{\partial y} = \frac{\partial u}{\partial y'} + \frac{\partial z'}{\partial y'}\frac{\partial u}{\partial z'} \qquad (5.3)$$

Here, terrain following coordinates are denoted with a 'prime.' Second-order, centered differencing was used to compute all the derivatives. The cross-stream velocity component gradients are computed in a similar way.

We computed the ratio, R, at different scales by filtering the LES results using a top-hat (i.e., moving average) filter with widths of 90 m, 120 m, 150 m, 180 m, 240 m, 300 m, 450 m,

600 m, 900 m, 1,200 m, 1,500 m, 1,800 m, 2,400 m, 2,700 m, and 3,000 m. The results are presented in Figure 5.2.
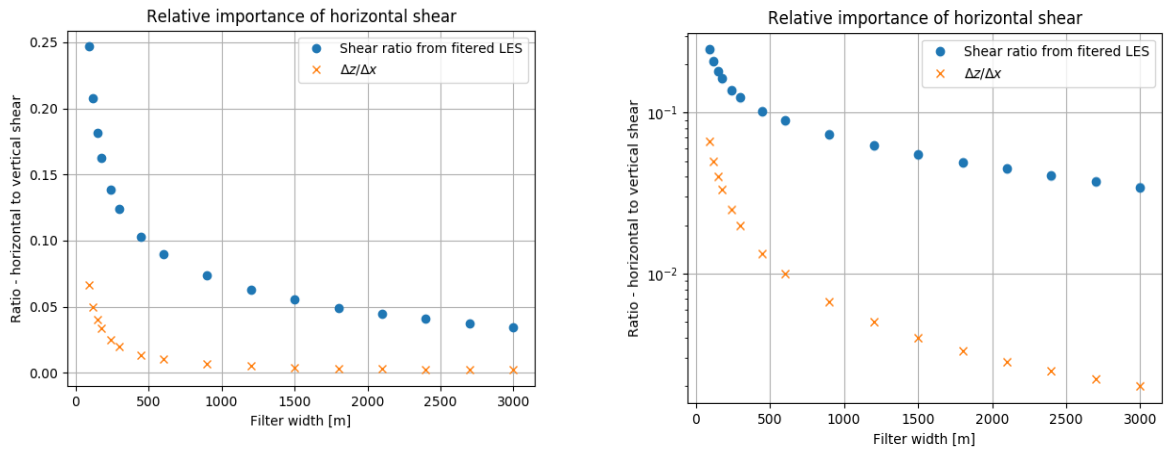
Figure 5.2. Relative magnitude of horizontal gradients in comparison to vertical gradients, as a ratio given by Equation (5.1), computed by filtering LES output at different scales (blue). Left panel—linear-linear plot of the ratio; right panel—log-linear plot of the ratio. The ratio of vertical-to-horizontal grid-cell size is also presented for comparison (orange).

The blue dots represent the ratio of horizontal vs. vertical shear. These results demonstrate that when the grid-cell size is greater than 1,500 m, the horizontal shear is on average less than 5% of the vertical shear in magnitude and decreases as the horizontal grid-cell size increases. However, when the horizontal grid-cell size is less than 1,500 m and while vertical grid-cell size is kept constant (in this case at 12 m), the relative magnitude of the horizontal shear increases exponentially, reaching 25% of the vertical shear magnitude when the horizontal grid-cell size reaches 90 m.

The significance of horizontal gradients in the 3D PBL parameterization can be estimated by analyzing the matrix equation that must be inverted to compute all the turbulent stresses. This matrix is shown in equation 5.4. In this equation, horizontal gradients of horizontal velocity components are highlighted by red boxes. Horizontal gradients figure in a number of diagonal terms together with the turbulent kinetic energy denoted by q/2. In addition, the dominant turbulent shear stress terms are highlighted by yellow boxes. These terms are multiplied and, therefore, also modulated by horizontal gradients highlighted by both red and yellow boxes.

$$
\begin{bmatrix}
\frac{q}{2\ell_1}+2\frac{\partial U}{\partial x} & \frac{\partial V}{\partial y} & -\frac{\partial W}{\partial z} & 2\frac{\partial U}{\partial y}-\frac{\partial V}{\partial x} & 2\frac{\partial U}{\partial z}-\frac{\partial W}{\partial x} & -\frac{\partial V}{\partial z}-\frac{\partial W}{\partial y} & 0 & 0 & \beta g & 0 \\
\frac{\partial U}{\partial x} & \frac{q}{2\ell_1}+2\frac{\partial V}{\partial y} & -\frac{\partial W}{\partial z} & 2\frac{\partial V}{\partial x}-\frac{\partial U}{\partial y} & -\frac{\partial U}{\partial z}-\frac{\partial W}{\partial x} & 2\frac{\partial V}{\partial z}-\frac{\partial W}{\partial y} & 0 & 0 & \beta g & 0 \\
\frac{\partial U}{\partial x} & \frac{\partial V}{\partial y} & \frac{q}{2\ell_1}+2\frac{\partial W}{\partial z} & -\frac{\partial U}{\partial y}-\frac{\partial V}{\partial x} & 2\frac{\partial W}{\partial x}-\frac{\partial U}{\partial z} & 2\frac{\partial W}{\partial y}-\frac{\partial V}{\partial z} & 0 & 0 & -2\beta g & 0 \\
\frac{\partial V}{\partial x} & \frac{\partial U}{\partial y} & 0 & \frac{q}{3\ell_1}+\frac{\partial U}{\partial x}+\frac{\partial V}{\partial y} & \frac{\partial V}{\partial z} & \frac{\partial U}{\partial z} & 0 & 0 & 0 & 0 \\
\frac{\partial W}{\partial x} & 0 & \frac{\partial U}{\partial z} & \frac{\partial W}{\partial y} & \frac{q}{3\ell_1}+\frac{\partial U}{\partial x}+\frac{\partial W}{\partial z} & \frac{\partial U}{\partial y} & -\beta g & 0 & 0 & 0 \\
0 & \frac{\partial W}{\partial y} & \frac{\partial V}{\partial z} & \frac{\partial W}{\partial x} & \frac{\partial V}{\partial x} & \frac{q}{3\ell_1}+\frac{\partial V}{\partial y}+\frac{\partial W}{\partial z} & 0 & -\beta g & 0 & 0 \\
\frac{\partial \theta}{\partial x} & 0 & 0 & \frac{\partial \theta}{\partial y} & \frac{\partial \theta}{\partial z} & 0 & \frac{q}{3\ell_2}+\frac{\partial U}{\partial x} & \frac{\partial U}{\partial y} & \frac{\partial U}{\partial z} & 0 \\
0 & \frac{\partial \theta}{\partial y} & 0 & \frac{\partial \theta}{\partial x} & 0 & \frac{\partial \theta}{\partial z} & \frac{\partial V}{\partial x} & \frac{q}{3\ell_2}+\frac{\partial V}{\partial y} & \frac{\partial V}{\partial z} & 0 \\
0 & 0 & \frac{\partial \theta}{\partial z} & 0 & \frac{\partial \theta}{\partial x} & \frac{\partial \theta}{\partial y} & \frac{\partial W}{\partial x} & \frac{\partial W}{\partial y} & \frac{q}{3\ell_2}+\frac{\partial W}{\partial z} & -\beta g \\
0 & 0 & 0 & 0 & 0 & 0 & \frac{\partial \theta}{\partial x} & \frac{\partial \theta}{\partial y} & \frac{\partial \theta}{\partial z} & \frac{q}{\Lambda_2}
\end{bmatrix}
\begin{bmatrix}
\overline{u^2} \\ \overline{v^2} \\ \overline{w^2} \\ \overline{uv} \\ \overline{uw} \\ \overline{vw} \\ \overline{u\theta} \\ \overline{v\theta} \\ \overline{w\theta} \\ \overline{\theta^2}
\end{bmatrix}
=
\begin{bmatrix}
\frac{q^3}{6\ell_1}+3C_1q^2\frac{\partial U}{\partial x} \\
\frac{q^3}{6\ell_1}+3C_1q^2\frac{\partial V}{\partial y} \\
\frac{q^3}{6\ell_1}+3C_1q^2\frac{\partial W}{\partial z} \\
C_1q^2\left(\frac{\partial V}{\partial x}+\frac{\partial U}{\partial y}\right) \\
C_1q^2\left(\frac{\partial W}{\partial x}+\frac{\partial U}{\partial z}\right) \\
C_1q^2\left(\frac{\partial W}{\partial y}+\frac{\partial V}{\partial z}\right) \\
0 \\ 0 \\ 0 \\ 0
\end{bmatrix}
\qquad (5.4)
$$

5.2 Porting 3D PBL Code from WRF v3.8.1 to v4.0.3

We implemented the new 3D PBL parameterization code into WRF version 4.0.3 to remain updated with the newest iteration of the numerical model. This task involved careful numerical testing of the WRF model after adding each portion of the 3D PBL code to ensure that we did not unintentionally alter the fundamental framework. Testing involved running three short (30 seconds to 1 minute of model time) simulations with WRF in LES mode and mesoscale mode with the Mellor-Yamada-Nakanishi-Niino (MYNN) PBL parameterization activated (Nakanishi and Niino 2006). The three simulations tested for differences in output between (1) nonrestart and restart simulations, (2) serial and parallel simulations, and (3) unmodified (official release version) and modified WRF code (development code containing the 3D PBL parameterization). In addition, we ran two short simulations with WRF in mesoscale mode and using the 3D PBL parameterization. For these 3D PBL simulations, we tested for differences in output between configurations (1) and (2) only because there is not yet an official release version of the 3D PBL parameterization. During the porting process, we discovered a couple of coding typos that influenced the tendency calculations due to horizontal gradients in turbulent fluxes. We speculate that the impact of these coding errors was minor.

As we ported each portion of the 3D PBL code to the new WRF version, we cleaned the code for readability. Examples of these housekeeping measures include renaming variables and adding new subroutines.

5.3 3D PBL Substepping

When simulating a real case with the new 3D PBL parameterization, one may need to reduce the model time step according to the domain topography because the parameterization becomes numerically unstable. To ameliorate this issue, we implemented a capability to substep only the 3D PBL parameterization. The benefit of including such a capability is that the model time step may be run near the recommended $6*\Delta x$, where Δx is the horizontal grid spacing in kilometers. This new feature is user-friendly; one needs to include only a single namelist option ('pbl3d_nsteps') and decide the number of substeps necessary for the particular application. The default number of substeps is set to '1' (that is, a single pass through the 3D PBL parameterization).

The basic logic of the 3D PBL substepping is: (1) first, we save the state variables (u, v, w, θ, and q_v) into temporary arrays (local to the 3D PBL parameterization) at the beginning of the

procedure; (2) then, the tendencies for each of the state variables are calculated from the divergence of the turbulent fluxes and added to both the (i) WRF official tendency arrays and (ii) temporary (local) state variable arrays. While (i) is conducted irrespective of substepping, (ii) is conducted so that the state arrays are updated for the substepping routine. Step (2) is repeated for the number of substeps that the user specifies.

To quantitatively understand the impact of choosing a particular number of substeps, we run an idealized LES (90 x 90 x 40 grid cells in the x, y, and z dimensions; Δx = 100 meters) with a homogeneous surface heat flux set to 279 W m^{-2} for 2 hours of model time. The model time step (Δt) is set to 1 second. We modify the WRF code base to calculate—at each model time step—the state variable tendencies (u, v, w, θ, and q_v) due to 3D turbulent mixing using 1, 2, 4, 8, 16, 32, 64, and 128 substeps. We consider the 128 substep solution to be the control and calculate the maximum percentage difference in the tendencies at all grid cells in the domain between the control and the 1, 2, 4, 8, 16, 32, and 64 substep solutions (Fig. 5.3). We calculate the differences using 4 substeps twice (hence, plotting the 'SS_4' and 'SS_4b' lines) to ensure that our technique is robust. We confirm that the difference between these two solutions is equal to zero. The model solution is advanced using only the 3D PBL control (128 substep) solution. Therefore, the percentage errors plotted in Figure 5.3 are due to only the numerical substepping method.
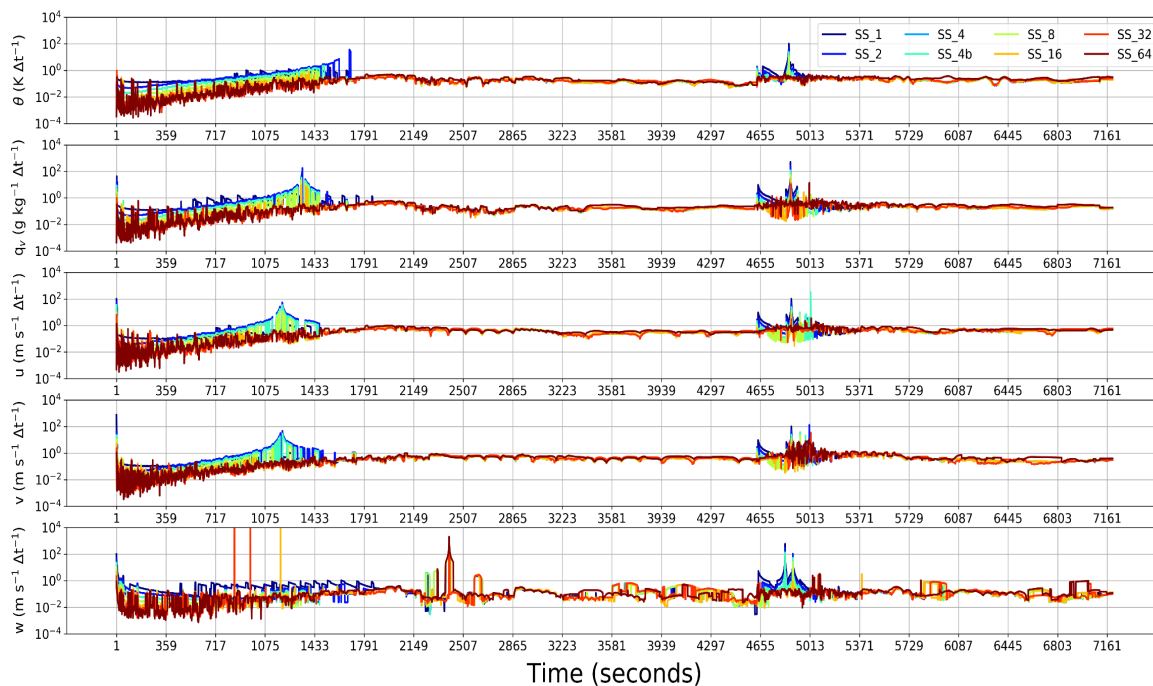
Figure 5.3. The maximum percentage tendency difference across all domain grid cells between the 3D PBL numerical solution using 128 substeps and the 3D PBL numerical solution using 1, 2, 4, 8, 16, 32, or 64 substeps (colored according to legend in top-right corner of figure) for each model time step (Δt = 1 second). From top to bottom: potential temperature (θ), water vapor mixing ratio (q_v), u-component of the wind (u), v-component of the wind (v), and vertical velocity (w). The percentage difference is calculated as: 100% * (x_i − x_{ctrl})/ x_{ctrl} , where x_i is the solution using 1-64 substeps and x_{ctrl} is the solution using 128 substeps. Note that we show the y-axis in log scale.

There are several features to highlight in Figure 5.3. First, and as expected, the maximum percentage difference decreases as the number of substeps increases. Also, Figure 5.3 suggests that there are distinct regimes whereby the number of 3D PBL substeps may or may not appreciably change the 3D PBL solution. The maximum percentage differences increase during model spin-up (from t = 0 second to t ≈ 1800 seconds) as the PBL deepens. Evaluation of the vertical model index (not shown) confirms that the maximum difference occurs typically near the PBL top (that is, increasing vertical model index as the spin-up period progresses). From t ≈ 1,800 seconds to t ≈ 4,500 seconds and from t ≈ 5,300 seconds to t = 7,200 seconds, in general, the domain maximum difference for each of the state variable tendencies is approximately tenths of a percentage. In this regime, the 3D PBL solution is relatively insensitive to the number of substeps. Moreover, we see convergence from t ≈ 4,500 seconds to t ≈ 5,300 seconds; that is, a solution using relatively few substeps (e.g., 4) yields relatively large and erratic maximum differences, whereas that using relatively many substeps (e.g., 64) yields relatively small and consistent maximum differences. The cause of the spike in maximum differences during this time period is curious and additional tests confirm that these values occur at the PBL top (not shown). These results suggest that the sensitivity of the numerical approach outlined herein may be linked to atmospheric stability and resultant PBL characteristics; however, more testing is needed to confirm this hypothesis.

Through preliminary testing of the aforementioned and additional idealized simulations, we find that the increased cost of substepping the 3D PBL parameterization is approximately 7% per substep. Additionally, a single domain (Δx = 750 meters), real-world case over a 5-day period and covering the WFIP 2 Wasco field site benefits greatly from using the substepping. Before the substepping, the model time step must be set to 0.5 seconds to avoid numerical stability issues. After the substepping, the simulation runs successfully using a 4-second time step, resulting in a substantial overall speed up in model run time.

5.4 Prognostic TKE

To solve the system of linear equations for the 3D PBL parameterization, one must calculate both the master length scale and the TKE at each grid cell. Therefore, accurately calculating the TKE is a crucial component of the turbulent closure model. Up to this point in the 3D PBL parameterization development, we have calculated the TKE diagnostically; that is, TKE is dependent upon characteristics of the atmospheric state from only the current time step and the local grid cell. While this approach is relatively simple and cost effective, the TKE field may not evolve smoothly. In some instances, we expect that this may contribute to the numerical stability issues discussed in section 5.3. To address this problem, we implemented a prognostic form of the TKE equation following Mellor and Yamada (1974, 1982). One of the main advantages of calculating TKE using a prognostic equation is that the field evolves smoothly because TKE is updated from the previous time step and is dependent upon information from both the local grid cell and adjacent grid cells. The prognostic TKE equation accounts for the following physical processes: vertical and horizontal advection of TKE, vertical and horizontal turbulent transport of TKE, shear production of TKE, buoyancy production of TKE, and dissipation of TKE.

Idealized simulations to test the prognostic TKE implementation are currently underway. We also plan to test the new approach for real-world cases, including days from the WFIP 2 field campaign. Moreover, we hypothesize that running the new parameterization with prognostic TKE will reduce the number of substeps needed or eliminate the need for substepping.

5.5 Surface Boundary Conditions

The advancements described in this section are being implemented currently by Masih Eghdami (graduate student at Duke University working under the direction of Ana P. Barros). To determine the boundary conditions near the surface after diagnosing $\overline{uw}, \overline{vw}, \overline{wq_w}$, and $\overline{w\theta}$ from from the surface layer boundary conditions, the rest of the turbulent components can be diagnosed using the PBL equations. Other approaches such as Mellor (1973) are not readily available for modeling purposes as they are given for a streamline. Furthermore, the ratios between the velocity variance show a clear violation of the isotropy assumption, which is used in the model. Here, we use a simplistic empirical fit to diagnose the total available kinetic energy near the surface (q_{surf}) based on stability conditions.

$$q_{surf} = \{7.00u_*^2 + 0.33, \partial\theta_v/\partial z < 0 \quad 9.47(\partial\theta_v/\partial z) + 0.84, \partial\theta_v/\partial z \geq 0 \tag{5.5}$$

where u_* is the friction velocity and $\partial\theta_v/\partial z$ is the vertical derivative of virtual potential temperature. The model is a linear fit based on the values obtained from the 17-m-tower flux (identification code: 19z.b0). Otherwise we set q as the maximum of q_{surf} and the q diagnosed from the second layer. Furthermore, for vertical momentum transfer, we have an estimate of friction velocity that is $u_f^2 = \sqrt{\overline{uw}^2 + \overline{vw}^2}$. The turbulent shear stress components can be computed as follows:

$$\overline{uw} = u_f^2 U/(U^2 + V^2)^{1/2} \tag{5.6}$$

$$\overline{vw} = u_f^2 V/(U^2 + V^2)^{1/2} \tag{5.7}$$

The vertical heat and moisture flux can be diagnosed based on the surface layer:

$$\overline{w\theta} = HFX/\rho c_p \tag{5.8}$$

$$\overline{wq_v} = QFX/\rho \tag{5.9}$$

where HFX and QFX are sensible heat and moisture flux, respectively; ρ is density, and c_p is specific heat of the air. For diagnosis of the rest of the fluxes, we make two assumptions: first, we use the second layer derivatives for the surface; second, we assume that the Mellor and Yamada (1982) model, which is based on the return to isotropy, is still valid at the surface. Using the already diagnosed fluxes the rest of the fluxes will be as follows:

$$\overline{w\theta_v} = \overline{w\theta} + 0.608T_{skin}\overline{wq_v}/(1 + 0.608q_v) \tag{5.10}$$

where we use the surface skin temperature and the water vapor from the first model layer (not the surface). We can now calculate the rest of the velocity covariances as follows:

$$\overline{uv} = -3A_1l/q(\overline{uw} + \overline{vw}) \tag{5.11}$$

$$\overline{u^2} = q_{surf}/3 + 2A_1(-2\ \overline{uw}\ dU/dz + \overline{vw}\ dV/dz - g/T_0\ \overline{w\theta_v}) \tag{5.12}$$

$$\overline{v^2} = q_{surf}/3 + 2A_1(\overline{uw}\ dU/dz - 2\ \overline{vw}\ dV/dz - g/T_0\ \overline{w\theta_v}) \tag{5.13}$$

$$\overline{w^2} = q_{surf} - \overline{u^2} - \overline{v^2} \tag{5.14}$$

Now we can calculate the lateral components of horizontal heat fluxes:

$$\overline{u\theta_v} = -3A_2l/q\left(\overline{uw}\left(\frac{d\theta_v}{dz}\right) + \overline{w\theta_v}\left(\frac{dU}{dz}\right)\right) \tag{5.15}$$

$$\overline{v\theta_v} = -3A_2l/q\left(\overline{vw}\left(\frac{d\theta_v}{dz}\right) + \overline{w\theta_v}\left(\frac{dV}{dz}\right)\right) \tag{5.16}$$

and the temperature variance as:

$$\overline{\theta_v^2} = -B_2l/q\;\;\overline{w\theta_v}\left(\frac{d\theta_v}{dz}\right) \tag{5.17}$$

The moisture fluxes are then

$$\overline{uq_v} = -3A_2l/q\left[\overline{uw}\left(\frac{dq_v}{dz}\right) + \overline{wq_v}\left(\frac{dU}{dz}\right)\right] \tag{5.18}$$

$$\overline{vq_v} = -3A_2l/q\left[\overline{vw}\left(\frac{dq_v}{dz}\right) + \overline{wq_v}\left(\frac{dV}{dz}\right)\right] \tag{5.19}$$

The horizontal heat flux terms can be calculated using the following expressions:

$$\overline{u\theta} = \overline{u\theta_v} - 0.608T_{skin}\,\overline{uq_v}/(1 + 0.608q_v) \tag{5.20}$$

$$\overline{v\theta} = \overline{v\theta_v} - 0.608T_{skin}\,\overline{vq_v}/(1 + 0.608q_v) \tag{5.21}$$

This completes diagnosing the 13 turbulent covariances. These surface boundary conditions were implemented in the 3D PBL parameterization. The TKE observed at 10 m above the surface was compared to the TKE obtained using the Mellor-Yamada and MYNN surface layer parameterization as well as surface boundary conditions implemented in the 3D PBL scheme described above. In addition, a parameterization accounting for the buoyancy is assessed. Figure 5.4 demonstrates that the 3D PBL implementation results in more accurate estimation of the TKE near the surface in comparison to other approaches.
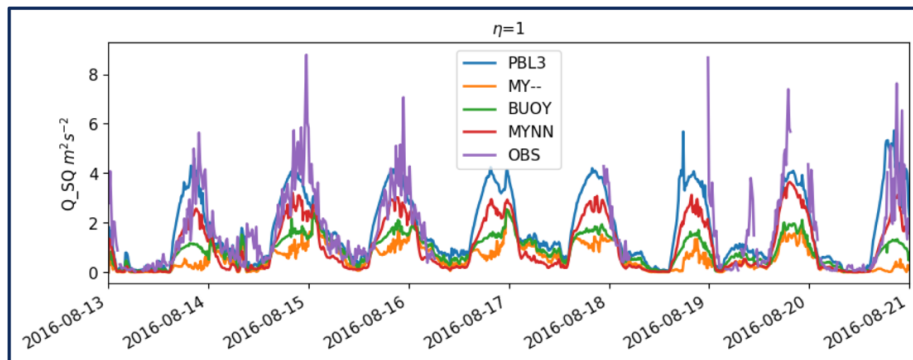
Figure 5.4. Comparison of TKE at 10 m using the 3D PBL parameterization of surface stresses (blue), Mellor-Yamada (MY) surface layer parameterization (orange), surface layer parameterization, including buoyancy effects (green), MYNN surface layer parameterization (red), with observations (purple).

6.0   Comparing Coupling Models

In FY19, the Mesoscale-Microscale Coupling Methods group both further developed MMC methods and began a more formalized assessment of the various coupling methods being developed. It is important to stress that there are a variety of different coupling methods that the MMC team is developing and using. Because wind energy is so interdisciplinary, there is also a variety of different applications. There is no one coupling method that stands superior to the others. Rather, different coupling methods excel at different applications. The Mesoscale-Microscale Coupling Methods group sees its role as pursuing new methods and uncovering the advantages and limitations of each coupling method for different applications, then sharing that knowledge so that others can choose coupling methods appropriate for their unique problem.

When considering mesoscale-microscale coupling, we tend to classify methods by four attributes that all coupling methods embody, shown graphically in Figure 6.1:

- Communication Directionality: This attribute simply defines the direction of information transfer between the mesoscale and the microscale. One-way or downscale communication directionality means that information from the mesoscale solution (or even field data) informs the microscale. Two-way or down/upscale means that the mesoscale information informs the microscale, and the microscale solution then feeds back to inform the mesoscale solution.

- Communication Strategy: This attribute describes how information from the mesoscale and microscale simulations is shared. For example, within a single WRF simulation, WRF mesoscale can be run with an embedded WRF-LES microscale nest and information can be shared via the computer's memory, which is referred to as online coupling. On the other hand, a mesoscale simulation may be run (or even observational mesoscale collected), and the generated data saved to hard disk. It is then later accessed by a microscale simulation code, which is referred to as offline coupling.

- Information Transferred: This attribute describes what type of information is transferred between the mesoscale and microscale simulations. Measurable or solved-for quantities—including velocity, temperature, pressure, turbulent stresses, surface fluxes, etc.—are referred to as "direct quantities." On the other hand, "indirect quantities" are quantities such as mesoscale momentum transport equation terms (e.g., advection), that are not direct quantities but highly influence the direct quantities. This is termed the "budget" approach because they derive from the mesoscale momentum and thermodynamic budgets.

- Information Transfer Location: The information transferred has to be transferred at specified locations, which this attribute describes. The most common transfer locations in the methods we use are on the microscale domain boundaries ("boundary-forced" methods), so two-dimensional surfaces that are the edge of the microscale control volume, or over the entire microscale volume ("internally forced" methods). With boundary-forced methods, quantities including velocity and temperature are extracted from within the mesoscale domain and applied over the entire microscale domain boundary in a time-varying fashion. Boundary-forced methods usually require some sort of additional perturbation, which is the topic of Chapter 7.0. Internally forced methods treat the microscale domain as periodic, much like with canonical atmospheric boundary layer simulations, but time-height-varying source terms are applied to capture the influence of the mesoscale forcing on the microscale flow.
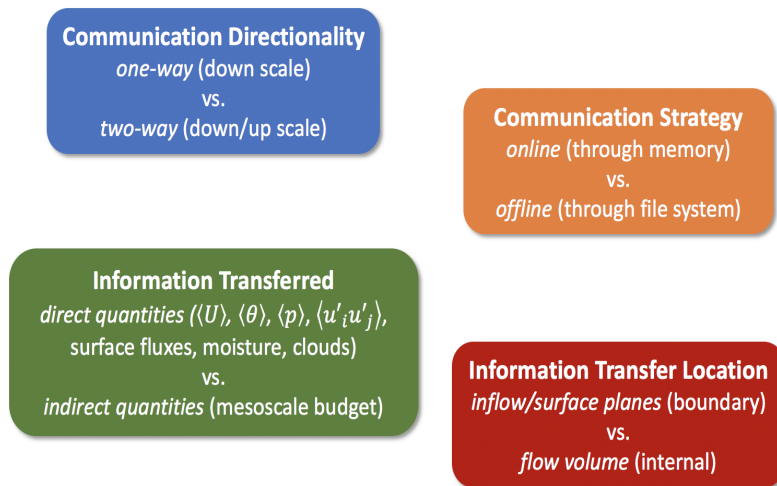
Figure 6.1. The four attributes of mesoscale-microscale coupling techniques and each attribute's current possible options.

In FY19, significant effort was placed on 1) the development of the "profile assimilation technique", 2) further exploring and developing the "budget component" approach, and 3) inflow-turbulence-generation methods. An overview of efforts (1) and (2) is given in Section 6.1. Effort (3) is extensive, so all of Chapter 7.0 is devoted to it.

Both methods from efforts (1) and (2) are one-way, offline, and internally forced. They differ in that the profile assimilation technique utilizes the direct quantities of velocity and potential temperature derived from mesoscale simulations or observations whereas the budget component approach uses the indirect quantities of large-scale advections and pressure gradient forces from the mesoscale transport equations. Effort (3) has been applied to one-way, online and offline, boundary-forced methods.

The overall roadmap for comparing coupling methods is a multiyear effort. The plan is to apply the various coupling methods to atmospheric flows over flat terrain, complex terrain, and offshore. In FY19, we focused on the flat terrain situation covered in Section 6.2, but we also performed side studies in the complex terrain situation described in Section 6.3, gravity wave treatment outlined in Section 6.4, and the effect of including microphysics in the microscale domain detailed in Section 6.5.

6.1 FY19 Coupling Method Development

6.1.1 Budget Component Approach

Prior to FY19, we tested the "budget component" approach, which is an internal information transfer coupling method that uses the indirect information of terms from the mesoscale momentum and potential temperature budgets. Namely, for momentum, the pressure-gradient force and the advective term, and for temperature, the advective term are taken from the mesoscale model. These quantities are extracted as time-height histories, which are then used as input to the LES. From the microscale point of view, these terms are applied as time-height varying source terms, and the LES is treated as horizontally periodic. This method only applies to cases that have a significant degree of horizontal homogeneity.

In FY19, we rigorously tested the budget component approach, resulting in a publication (Draxl et al. 2019). We direct the reader to this article for details. The following gives a short summary of the work.

The approach was tested on the SWiFT November 8, 2013, diurnal cycle. Figure 6.2 shows the results of the predicted mean wind speed, wind direction, potential temperature, and turbulent kinetic energy at a typical turbine hub height from the microscale simulation (blue) as compared to WRF predictions (orange) and meteorological tower data from the site (green). It is clear that the microscale predictions are highly influenced by the mesoscale input data. However, both the microscale and mesoscale predictions are in error compared to the field data to some degree. Interestingly, however, the microscale wind speed predictions better agree with the field data during daytime conditions than do the mesoscale predictions, hinting that the microscale solver is able to correct deficiencies in mesoscale predicted shear. This brings up an important consideration, though, that if the mesoscale model simulation is in error, which is almost always the case, how do we separate coupling error seen in the microscale predictions from mesoscale error?
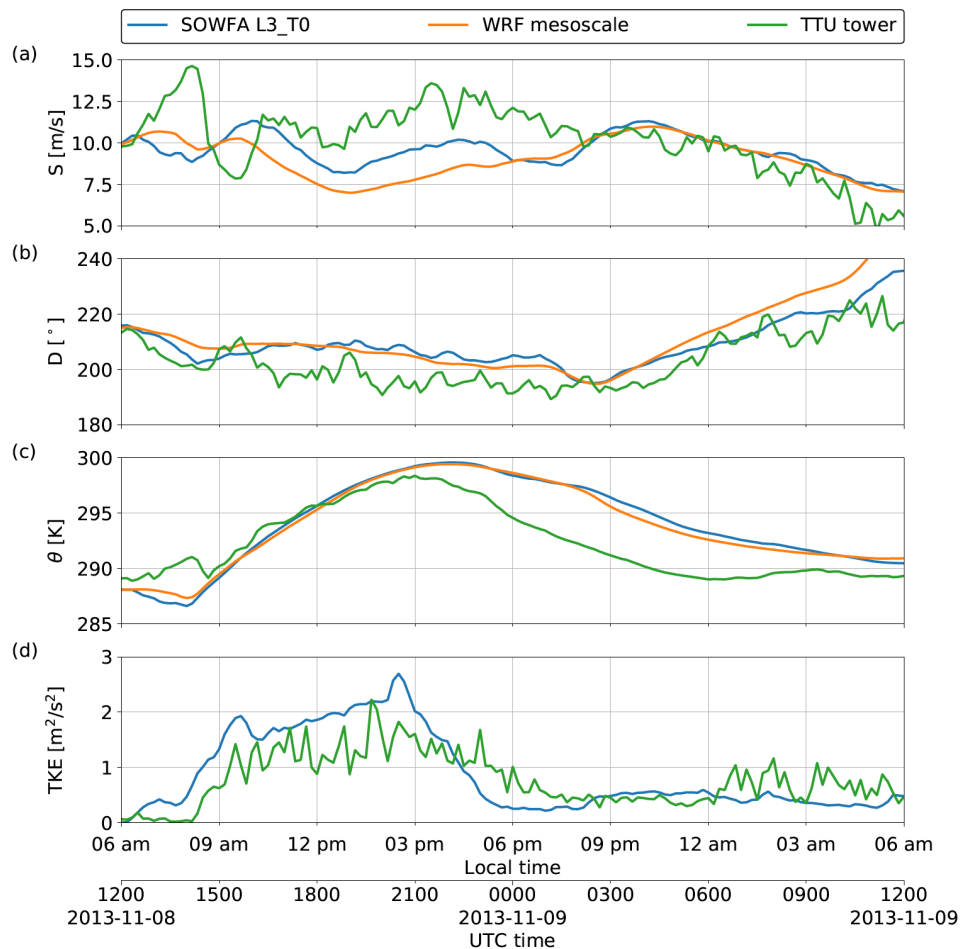
Figure 6.2. Time histories of (a) wind speed, (b) wind direction, (c) potential temperature, and (d) TKE from the mesoscale simulation (orange), the budget-component coupled microscale simulation (blue), and field data (green).

6.1.2   Profile Assimilation Technique

Prior to FY19, we developed an MMC technique in which a stand-alone, periodic microscale simulation is driven to strongly match given time-height histories of velocity and potential temperature in the planar-averaged mean via internal information transfer. In other words, the planar-averaged profile of velocity and temperature from the microscale LES was forced to follow given profiles using time-height-varying volumetric source terms, and the turbulence responds accordingly.

We developed this method because we had already seen the utility of internal information transfer with the budget-component approach outlined in Section 6.1.1. Although the budget-component approach shows promise, we do not always have access to budget components from the mesoscale solver (WRF has to be modified to output these quantities) and much more commonly we have profiles of measured variables. Moreover, sometimes we have field-observed profiles with which we may desire to inform a microscale simulation; for example, if we want to simulate a real observed day. Finally, mesoscale simulations of a particular event may not correctly capture quantities of interest.

The source-term mean-following enforcement was very strong, and the resultant computed turbulence compared to measurements could be in great error, as shown in Figure 6.3. In that figure, one can observe that during the daytime, computed TKE is two to three times as large as in the observations. The source of this error is the fact that the given daytime potential temperature profiles from WRF are superadiabatic all the way through the mixed layer, where they should be more constant with height. Strong enforcement of this superadiabatic condition leads to excessive buoyancy production of turbulence. This led to the FY19 development of a variant of this coupling technique termed the "profile assimilation technique" (PAT).
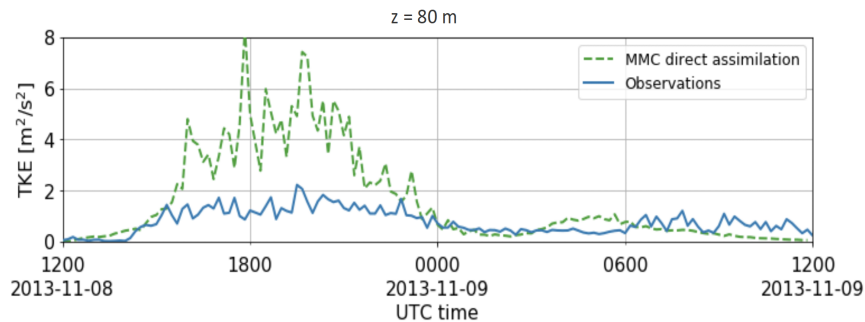
Figure 6.3. Computed and measured TKE at 80 m above the surface from a simulation and observations of the SWiFT site for the November 8, 2013 diurnal cycle.

With the PAT, the same general internal coupling idea is used, but rather than strongly enforcing that the microscale planar-averaged velocity and temperature time-height histories match given time-height histories, the enforcement is weaker. For each time step, the error between the given and computed planar-averaged profile is computed. Rather than specifying a source term that drives the error to zero at all heights, a polynomial fit to the error profile is computed, and source terms are computed based on this fit. Because the source term is proportional to a fit of the error profile, which is a much simpler profile than the actual error profile, it provides for vertical coupling of the source term, which was not present before. The result is that the LES-generated profiles of velocity and temperature are freer to respond to the turbulence they contain. This allows, for example, the LES to correct for the erroneous

superadiabatic conditions WRF predicted for the daytime SWiFT case as shown in Figure 6.4. The profile assimilation technique is documented in a recent publication (Allaerts et al. 2019).
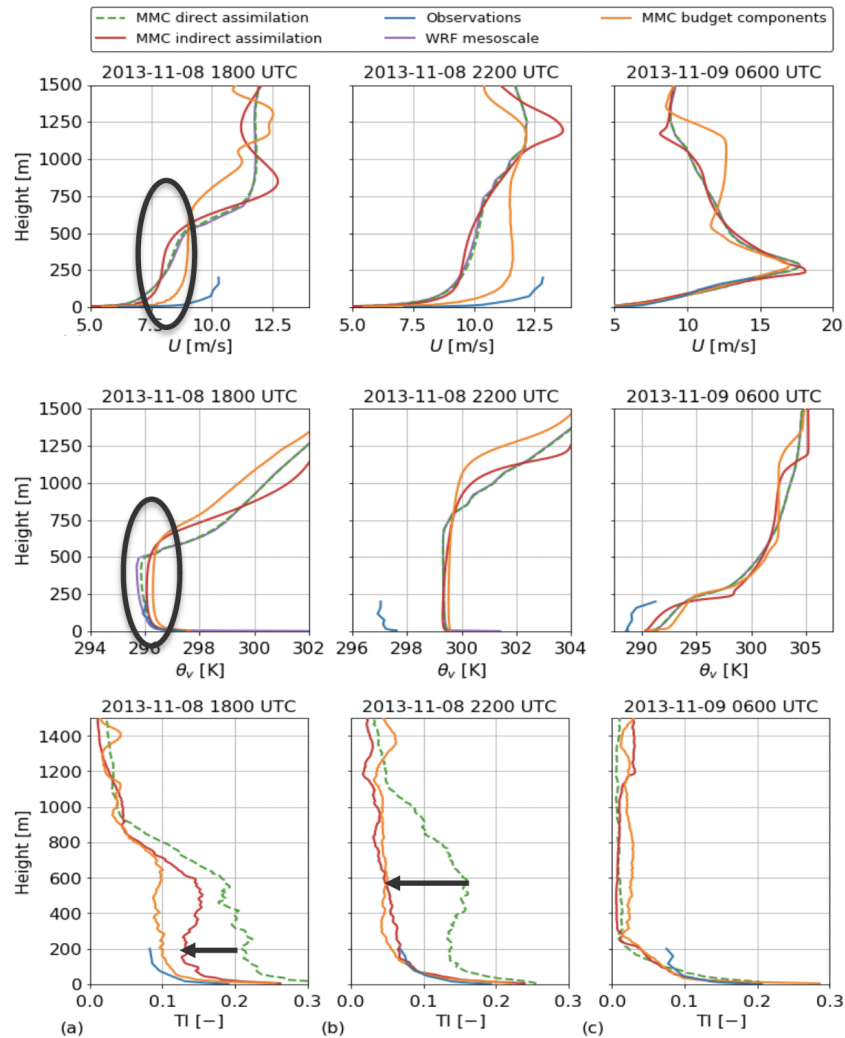
Figure 6.4. Profiles of wind speed (top row), potential temperature (middle row), and turbulence intensity (bottom row) in the late morning (left column), midafternoon (middle column), and night (right column) from observations, WRF mesoscale, and SOWFA using various kinds of coupling, including the profile assimilation technique (labeled here as MMC indirect assimilation in red).

Not only can the PAT method be driven with WRF-derived time-height histories, but with any given time-height history. This means that if one has field data, one can simply drive the microscale LES using those field data, which is a very powerful tool.

6.1.3   Other Coupling Method Development

Two coupling methods that underwent significant testing and development in FY19 are discussed in the previous two subsections, and they both use internal information transfer. The alternate class of coupling methods transfer information from the mesoscale to the microscale at the microscale domain boundaries. That class of method is more general and more

straightforward than internal information transfer methods, except that the inflowing mesoscale information contains no resolved turbulence as it is fed into the turbulence-resolving microscale domain. Therefore, the challenge is to produce realistic resolved turbulence with as little distance from the inflow boundary as possible. That problem merits enough research that Chapter 7.0 of this report is completely devoted to inflow turbulence generation.

6.2   Formal Coupling Method Study

The formal coupling method study initiated in FY19 was a comparison of methods in a flat-terrain diurnal cycle, namely the SWiFT, November 8, 2013, benchmark case. The coupling method study is currently in progress, so we are not able to report final results here. This section is meant to be an introduction to our study and a snapshot of current progress.

A variety of methods across the WRF, SOWFA, and Nalu-Wind codes is being compared. A summary of the coupling methods and their respective codes is shown in

Table 6.1 below. Each column of this table represents a different coupling configuration, and the rows below it describe the attributes of the particular coupling configuration. The title of the coupling configuration (in white) is of the format [Mesoscale Source] -> [Microscale Code]. The colored squares below each coupling configuration indicate which aspects of coupling that particular coupling configuration will compare. For example, the configuration "WRF -> Nalu-Wind" uses WRF-generated mesoscale data to inform the Nalu-Wind microscale solver. It utilizes one-way directionality of information transfer from mesoscale to microscale (i.e., there is no feedback from Nalu-Wind back to WRF). The communication strategy is offline, meaning WRF data are saved to disk and available for use at any later date; Nalu-Wind can read that data from disk while the microscale simulation is running. The "budget component" approach, described in Section 6.1.1, is used, meaning that the information transferred includes the momentum and temperature advective terms, and pressure-gradient force from the mesoscale budget, with the mode of information transfer being internal (except at the lower boundary where skin potential temperature from WRF is used to compute microscale surface flux). This method can be compared to the WRF->SOWFA 3 case, which is run in the same configuration to compare the effect of the choice of microscale solver code.

The remainder of this chapter details some of the coupling configurations included in this comparison. Not all configurations have been run as of this writing.

Table 6.1. A summary of the coupling methods studied in the coupling study initiated in FY19 and extending into FY20. The columns represent the different coupling configurations titled by [Mesoscale Source] -> [Microscale Code]. The rows define the different attributes of each coupling configuration. The colored squares below each configuration indicate which aspects of coupling a particular configuration aims to compare.

Legend:
- 🟥 code, boundary coupling
- 🟩 boundary vs. internal coupling
- 🟦 internal coupling approach
- 🟨 code, internal coupling
- 🟪 WRF vs. obs. meso input

	WRF -> WRF-LES	WRF -> SOWFA 1	WRF -> SOWFA 2	WRF -> SOWFA 3	WRF -> Nalu-Wind	Obs -> SOWFA
Communication Directionality	1-way	1-way	1-way	1-way	1-way	1-way
Communication Strategy	offline	offline	offline	offline	offline	offline
Information Transferred	All	$\langle U \rangle, \langle \theta \rangle, k, q_s$	$\langle U \rangle, \langle \theta \rangle, q_s$	mom./temp. budget, q_s	mom./temp. budget, q_s	$\langle U \rangle, \langle \theta \rangle, k, q_s$
Information Transfer Location	Boundary	Boundary	Internal	Internal	Internal	Internal
Perturbations	Turbsim	Turbsim	None	None	None	None

Comparison indicators below columns:
- WRF -> WRF-LES: 🟥
- WRF -> SOWFA 1: 🟥 🟩
- WRF -> SOWFA 2: 🟩 🟦 🟪
- WRF -> SOWFA 3: 🟨 🟦
- WRF -> Nalu-Wind: 🟨
- Obs -> SOWFA: 🟪

6.2.1 Mesoscale Simulation

Several mesoscale simulations over the SWiFT site are performed to generate initial conditions and forcing for the internal and boundary forced microscale simulations. While holding the model setup constant, various reanalysis data sets are utilized in an attempt to produce the most realistic simulation possible of the case day, Nov. 9, 2013. These reanalysis data sets include: ERA-Interim, GFS, NARR, and ERA5. The first three of these data sets are well known and have been used extensively within the meteorology community, while ERA5 is a new data set that has shown promise in improving reanalysis representation.

The mesoscale domain setup consists of three domains with respective grid sizes of 27, 9, and 3 km and centered roughly over the SWiFT site. Domain extents (west-east by north-south) are 3,186 km x 3,000 km for domain 1, 1,386 km x 1,197 km for domain 2, and 354 km x 300 km for domain 3. Model physics include the MYNN 2.5 level PBL parameterization, Morrison double moment microphysics (Morrison et al. 2009), and Rapid Radiative Transfer Model for climate model applications radiation on all three domains. For domain 1, the Kain Fritsch cumulus parameterization is employed. The WRF and WPS namelists for this case are available on the MMC GitHub (https://github.com/phawbeck/WRF-setups/tree/master/SWiFT_20131108_GFS).

Figure 6.5 shows the wind speed and wind direction at around 10 m for the SWiFT tower (black) and each of the reanalysis data sets tested herein. It can be seen that all of the reanalysis data sets fail to capture the peak winds within the wind ramp event. However, the wind speed in the ramp down period are captured fairly well by the GFS and NARR. Wind direction is consistent between each of the reanalysis data set cases with GFS having slightly better timing with the wind shift during the end of the ramp down period.
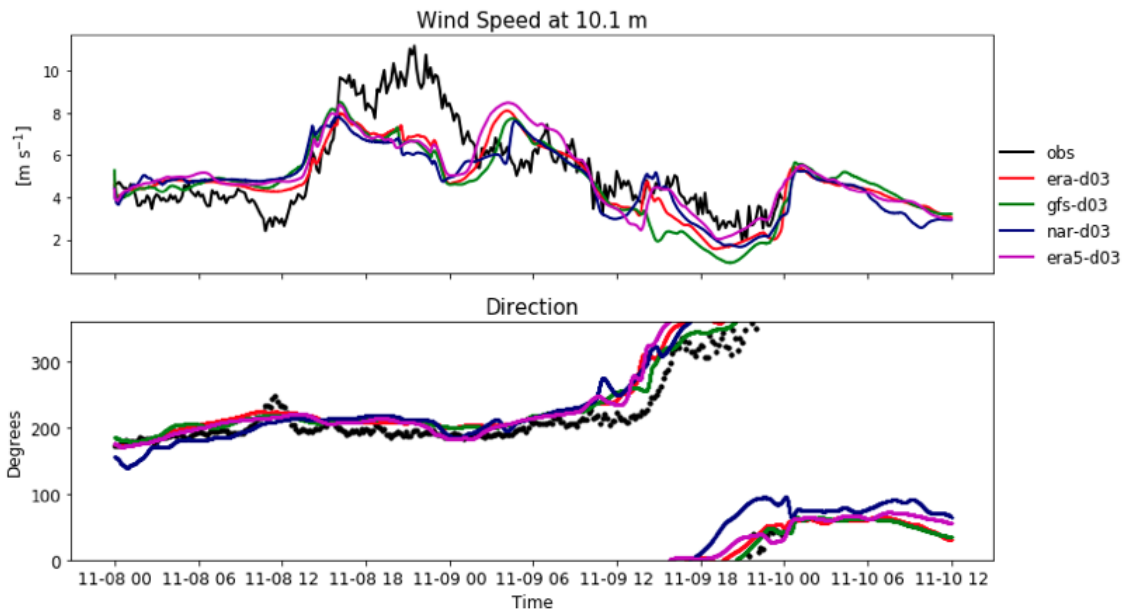
Figure 6.5. Wind speed (top) and direction (bottom) from Nov. 8 0 UTC to Nov. 10, 2013 0 UTC for SWiFT tower observations at 10.1 m (black), and the model grid on domain-3 that encompasses the SWiFT tower location in the mesoscale simulations driven by ERA-Interim (red), GFS (green), NARR (blue), and ERA5 (magenta) at 10 m.

Checking closer to hub height, Figure 6.6 shows roughly the same outcome, where the magnitude of the wind ramp is underpredicted (or possibly delayed by several hours) and the wind speed in the down ramp is overpredicted by each case. Wind direction is close for all cases, but slightly better for the GFS simulations.

Additional simulations consisting of larger parent domains, different boundary layer schemes, and additional or less spin-up time were also carried out (not shown) but little improvement was achieved between the other available cases. Thus, no model setup was able to provide very close agreement with observations for this case day. However, of the cases considered, the GFS performed somewhat better than the others and was chosen to be the mesoscale simulation moving forward.
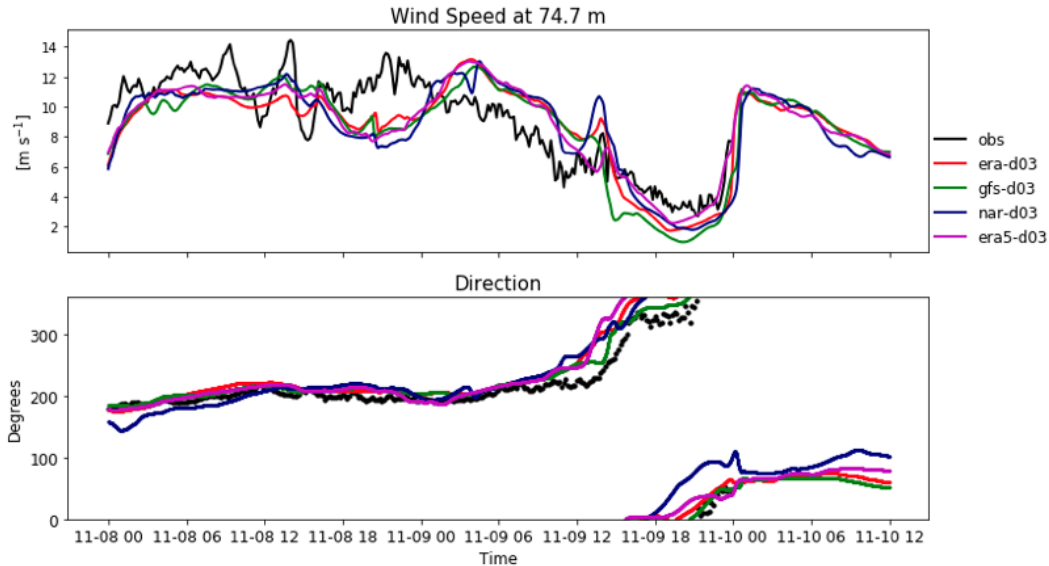
Figure 6.6.   Same as Figure 6.5 but for a height of 74.7 m and the closest WRF model level.

6.2.2   Boundary Information Transfer Coupled Cases

In the WRF->WRF-LES coupling configuration, the WRF framework is used so there is no need to transfer mesoscale data derived from one code to another. Here, WRF is run in mesoscale mode, as outlined in Section 6.2.1, and the data are saved to disk. As this is an offline coupling configuration, WRF-LES then reads in that data as boundary conditions.

The WRF->WRF-LES case will be carried out using two separate simulations as depicted in Figure 6.7. First, a simulation with two domains, d01 and d02, will be run using the online approach to produce the meteorological variables that provide boundary condition to the third domain, "doff" using offline approach. The region 2 km x 2 km (dashed line) within doff domain represents an area of interest for analyzing the results. The outer domain d01 obtains the boundary forcing from GFS reanalysis product and it runs in mesoscale mode (i.e., one-dimensional parameterization [MYNN 2.5 scheme]). The inner domain d02 runs in LES microscale mode (1.5 TKE closure) and receives boundary forcing through its parent domain in each time step. The horizontal grid spacing of domains d01 and d02 are 1.65 km and 150 m, respectively. Both domains use 159 vertical layers, with 10 m uniform grid spacing for the first 75 vertical grids and stretched grid spacing from 10 m at 750 m height to 950 m at the model top. The domain d02 starts 4 hours later than domain d01, and the data are saved for 24 hours from domain d02, which will be used later to provide boundary forcing to domain doff (with horizontal grid spacing of 10 m) in the separate simulation. Time-varying turbulence produced by a synthetic method (Turbsim) is ingested through the west and south boundary planes (shown by dashed line) to develop turbulence flow. The first two domains, d01 and d02, run concurrently. The domain doff runs independently from d01 and d02, but couples with d02 using its flow field as boundary forcing (called offline coupling). The results of the offline domain doff depend on the state of the flow field of the outer domain d02, but not the other way around (called one-way nesting). The offline method may require frequent data to update its boundary forcing to obtain similar results as from online method (in which all domains runs concurrently).
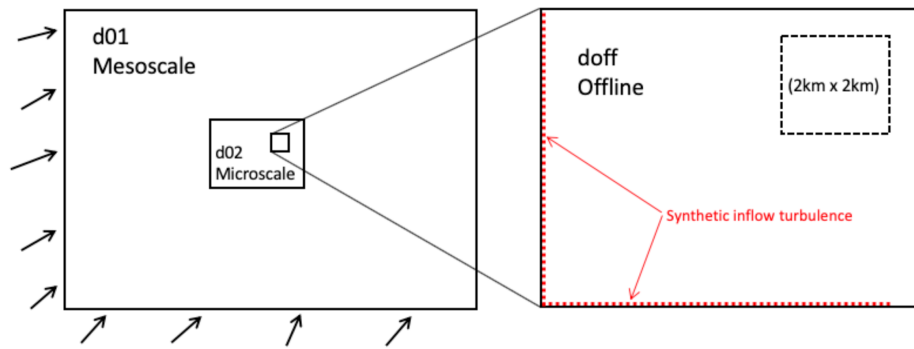
Figure 6.7. Schematic diagram of domains d01 and d02 that runs concurrently (left) and a domain doff that runs separately (right). The area with dashed line represents the area of interest for analysis.

The WRF->SOWFA 1 coupling configuration currently has not been performed, but it differs from the WRF -> WRF-LES case most markedly in that the coupling takes place across two completely different codes, WRF mesoscale and SOWFA microscale. The two codes have completely different numerics. WRF is fully compressible; SOWFA is incompressible with Boussinesq buoyancy effects. WRF contains many additional modules for atmospheric and surface physical processes beyond the basic flow equations, whereas SOWFA does not.

The plan is to use a SOWFA domain that is of 5-10-km horizontal extent and 2-km vertical extent with 10 m resolution. The south and west sides will be inflow sides upon which velocity and potential temperature are specified by bilinearly interpolating from saved WRF flow fields every 10 to 30 minutes. Superimposed upon that WRF inflow data is synthetic turbulence generated using the TurbSim tool. The same TurbSim-generated synthetic turbulence is used in the WRF->WRF-LES case for consistency.

6.2.3   Internal Information Transfer Coupled Cases

Four internal-coupled cases have or will be run. Two use SOWFA as the microscale solver and the only difference in the cases is whether the budget-component approach of Section 6.1.1 or the profile assimilation technique of 6.1.2 is used. A third case that uses the budget-component approach is run with Nalu-Wind as the microscale solver.

Last, another profile-assimilation technique case is run with SOWFA as the microscale solver, but the mesoscale source here includes profiles observed using the Texas Tech University 200-m tower and radar sounding system. This case is unique because it does not rely on WRF to generate simulated mesoscale data, but rather is informed by real-world field-observed mesoscale data. We find that, in most cases, the budget-component and profile assimilation techniques follow the general trends provided by WRF mesoscale data quite well. However, if the WRF mesoscale data contain significant errors, which is sometimes the case, it is difficult to separate coupling error from mesoscale model input data error. The Obs -> SOWFA case avoids this WRF error by directly using observed data. The error in the SOWFA microscale results should hence provide an improved indicator of error induced by the coupling method.

6.3   Role of Terrain in Microscale Turbulence Generation

To investigate how complex terrain generates turbulence within the boundary layer, we consider a semi-idealized case using SOWFA with a domain centered over the National Wind Technology Center at the National Renewable Energy Laboratory. The numerical domain includes roughly 10 km of the Colorado Rocky Mountains followed by several kilometers of the foothills and Great Plains. When the full complexity of the terrain was included within the model, gravity wave development and complexities within the inflow and outflow conditions on the model boundaries generated noise that greatly impacted the simulation results. To alleviate this issue, a large-windowed convolution was performed over the terrain and the large-scale terrain signal was removed. This left a domain with realistic peaks and valleys that oscillate about zero. Next, this terrain was smoothed with another window to test how rugged terrain needs to be to generate turbulence.

The inflow conditions considered are a neutral boundary layer with a capping inversion and another neutral layer above in the free atmosphere. This upper neutral layer was applied to prevent any gravity waves from forming near the model top. The horizontal pressure gradient is fixed to ensure that wind speeds within the boundary layer stay somewhat constant throughout the simulation at moderate wind speeds. Coriolis forcing is set to zero to guarantee that inflow is coming strictly from west to east (over the mountains).

A flat, periodic precursor simulation is performed to generate turbulent inflow conditions to the simulation including the terrain (Turbulent Case; TC). This precursor is also averaged every one second to produce nonturbulent inflow conditions (Nonturbulent Case; NTC). Lastly, a version of the stochastic cell perturbation method (see Chapter 7.0) is added on to the nonturbulent inflow (Cell Perturbation Case; CPC) to assess whether perturbations are necessary for complex terrain cases. Between these cases, TC serves as a control where the turbulence is fully developed at the inlet of the domain and then is augmented by the complex terrain. For both NTC and CPC, turbulence must develop with fetch and can be compared to the result from TC to assess how well the turbulence matches.

Results from this set of simulations indicate that at the lower model levels, complex terrain generates fairly consistent turbulence despite the inflow condition. However, once the analysis is performed throughout the depth of the boundary layer, the NTC produces large overshoots in TKE, and the mean TKE field does not closely match the mean TKE field from the TC simulations. By adding the perturbations at the inlet, the TKE overshoot is decreased and more of the domain is closer to matching that of the TC simulation.

By smoothing out the terrain, the TC again produces a boundary layer that is filled with turbulence due to the turbulent inflow. However, the NTC is only able to produce turbulence near the surface and fails to grow throughout the boundary layer. By adding perturbations, this is, again, improved. However, the magnitude of the cell perturbations was not adjusted to produce optimal results.

Similar cases were performed to assess the impact of boundary layer height on turbulence generation and wind speed on turbulence generation over complex terrain. The results indicate that as boundary layer height increases, there is a larger distance over which the turbulence generated by shedding off of the complex terrain features needs to travel to reach the boundary layer top. Further, as wind speed increases, more turbulence is tripped but there is less resonance time within the domain so it, too, takes more fetch before the turbulence can reach the top of the boundary layer. In all cases, adding perturbations improved performance.

6.4   Atmospheric Gravity Wave Treatment

A focus of our coupling work in FY19 was on how to treat atmospheric gravity waves that may form within the microscale domain, particularly when the microscale solver is separate from WRF. A problem arose in FY18 when gravity waves improperly interacted with domain boundaries of our SOWFA simulations of the Biglow Canyon/WFIP 2 site. To better understand the problem, in FY19, we devised a simplified 2D, nonturbulent case. The case consists of a variable length domain (up to 200 km, but as short as 40 km) that is 15-km tall. At the midpoint of the lower surface of the domain is a small, 100-m tall hill. The background temperature stratification is stable throughout the domain. As uniform 10-m/s flow passes over the hill, it generates significant gravity waves, as shown in Figure 6.8. Two appealing aspects of this simple test case are that there is a semi-analytical solution for the steady-state gravity waves and it is computationally inexpensive so many cases can be run.
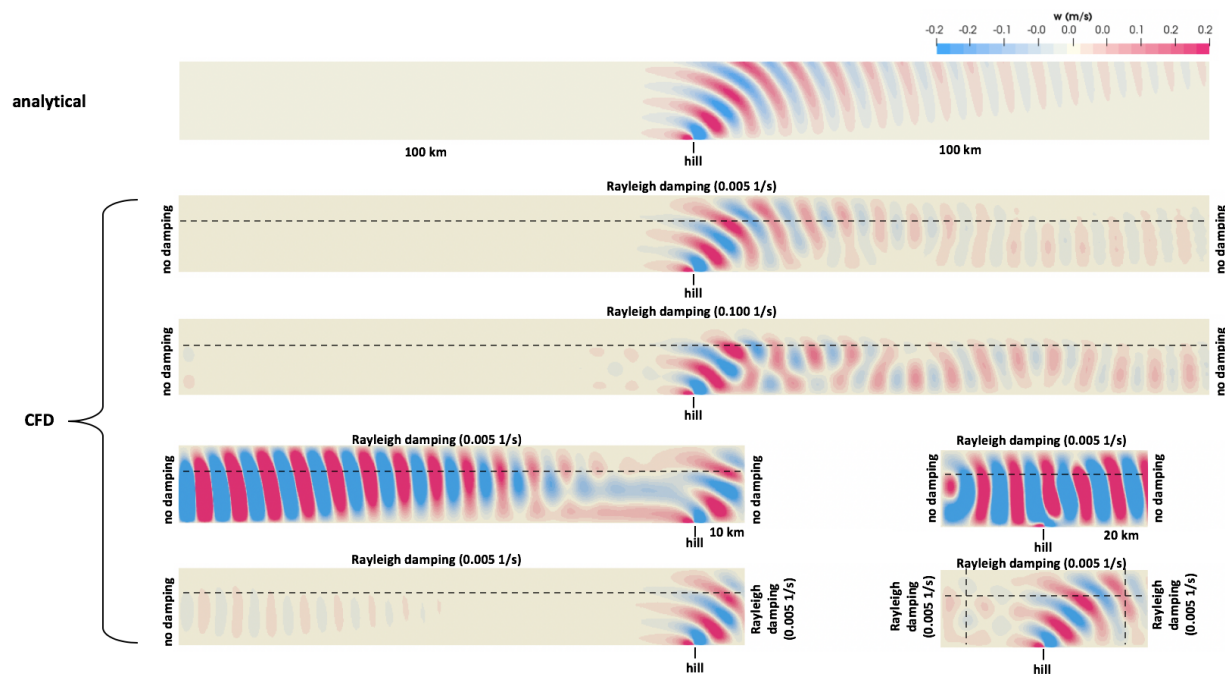
Figure 6.8. Contours of vertical velocity of a flow-over-hill case that generates atmospheric gravity waves. The upper contour plot is the analytical solution and all others are from the SOWFA microscale solver. The effect of domain length and Rayleigh damping is compared.

The main idea we examined was to add Rayleigh damping layers to study their effect at mitigating undesirable interaction of the gravity waves with domain boundaries. Damping layers of 5-km thick were placed at the top, inflow, and outflow sides of the domain. Each layer can be independently activated or varied in strength.

Figure 6.8 is an overview of the results that shows contours of vertical velocity, which well illustrates the gravity waves. The top contour plot is the semi-analytical solution; all other contour plots come from SOWFA solutions. (As a side note, we tried some cases with Nalu-Wind and obtained nearly identical solutions to SOWFA.) The next two contour plots show the effect of using only a top damping layer and how damping-layer strength affects the solution. With a 200-km-long domain, the lack of inflow or outflow damping layers does not matter, but an

upper damping layer is critical. A damping strength of about 0.005 1/s worked well. Too strong a damping layer causes the gravity waves to reflect off of the damping layer.

Next, we examined the effects of domain length and inflow and outflow damping layers (always with the top damping layer engaged). Interestingly, if we shortened the downstream side of the domain and did not use any outflow damping, spurious wave patterns formed upstream of the hill that very closely resemble the spurious wave patterns originally seen in the Biglow Canyon/WFIP 2 case. However, engaging Rayleigh damping on the outflow side nearly completely mitigates this problem, which is a key finding. Finally, we shortened the upstream domain length as well and use Rayleigh damping on the inflow, outflow, and upper domain boundaries; the solution reasonably well agrees with the analytical solution.

6.5 Sensitivity of Coupled WRF/WRF-LES Computations to Simplified Model Physics

To accurately predict mesoscale flow, numerical weather prediction models must account for the complexities of the moist atmospheric thermodynamic system and provide parameterizations for a number of physical processes that affect that system, such as radiative transfer and precipitation. In contrast, microscale computational fluid dynamics solvers that are used to resolve much finer scale details of the flow through wind plants often more roughly approximate, or even neglect altogether, these physical processes. These approximations decrease simulation cost and can also permit greater flexibility in the discretization and numerical schemes used by the microscale solver. However, it is unclear what impact these approximations have on predicted wind speeds and turbulence levels relevant for wind energy applications.

One goal of the MMC project is to provide guidance for users to determine the right approach for coupling between the mesoscale and microscale solvers, including the right grid resolution at which to transition to the microscale solver. An underlying premise of turbulence modeling is the concept of the energy cascade: TKE is expected to be transferred downscale, via the nonlinear momentum advection terms of the Navier-Stokes equations, from the largest eddies to progressively smaller ones. Therefore, it may be possible to capture the level of TKE in larger-scale boundary layer motions using a mesoscale solver with detailed atmospheric physics and then rely on the microscale solver to represent the primarily kinematic process of downscale energy transfer. However, atmospheric flows are complicated by the importance of buoyant production and destruction of turbulence in addition to shear production. Consequently, we must assess at what scale (if any) the errors associated more approximate treatments of buoyancy become acceptably small for flow quantities of interest to wind energy.

To address this question, we performed a series of simulations using WRF-LES at fine resolutions driven by boundary conditions extracted from coarser WRF-LES simulations. This procedure emulates the approach that could be used to drive a stand-alone microscale computational fluid dynamics solver such as Nalu-Wind. Various combinations of physical approximations were considered, as described in Table 6.2. These were compared to the offline-coupled "full physics" case, which was in turn compared to an online-coupled fine LES simulation. The approach is illustrated schematically in Figure 6.9. In addition to varying the treatment of surface fluxes, microphysics, and radiation, two additional sensitivity tests were performed using the full physics setup and varying only the value of the coefficient c_k used by the subgrid-scale turbulence closure by ±33% from its default value. Increasing this coefficient

strengthens the diffusive mixing effect associated with small-scale turbulent eddies that are not directly resolved in LES.

Table 6.2. Summary of the options used in each of the physics sensitivity test cases. Some options may be invoked by modification of WRF namelist entries, while others required source code changes. Specifically, the Morrison two-moment scheme (Morrison et al. 2009) is activated by WRF namelist option mp_phyics=10, the MYNN surface scheme is sf_sfclay_physics=5, and the Rapid Radiative Transfer Model for climate applications scheme for long- and short-wave radiation is ra_lw_physics=4, ra_sw_physics=4.

Case	Microphysics	Surface Fluxes	Radiation	Moisture Variables
Full Physics	Morrison 2-Mom[2]	MYNN[3]	RRTMG[1]	Unmodified
No Microphyiscs	None	MYNN	RRTMG	Unmodified
Averaged Fluxes	Morrison 2-Mom	MYNN spatial means	RRTMG	Unmodified
Fixed Fluxes	Morrison 2-Mom	Constant SH, LH	RRTMG	Unmodified
No Radiation	Morrison 2-Mom	Constant SH, LH	None	Unmodified
Dry	None	Constant SH, 0 LH	None	$q_v \approx 0,\ \theta_m = \theta$
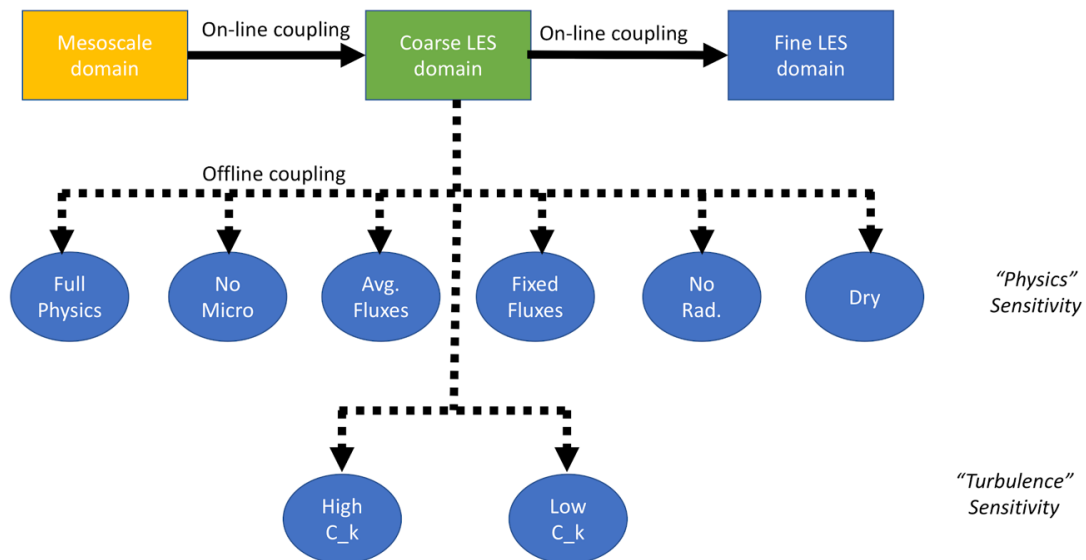
Figure 6.9. A schematic of the relationships between the simulations described in this section. Rectangular shapes indicate online-nested simulations which are connected to their parents with solid arrows; ovals indicate offline-nested simulations which are connected to their parents with dashed arrows. Blue color indicates the finest LES resolution; other colors denote coarser resolutions. The case names are explained in Table 6.2 and in the text.

For our study, we selected two time periods, representative of convective and stable conditions from the SWiFT diurnal cycle benchmark case that is used in other analyses by the MMC team. The SWiFT facility in western Texas is located in an area of generally flat terrain. The diurnal cycle benchmark case day of November 8-9, 2013 is associated with strong southwesterly winds and generally dry, clear conditions. These features make the diurnal cycle benchmark a

good starting point for understanding the impacts of various physical approximations on predicted boundary layer winds as greater complexity may be expected under conditions of stronger surface heterogeneity, higher humidity, and even cloudiness.

The convective scenario setup uses three nests: a mesoscale parent with 1.75-km horizontal resolution, an intermediate coarse LES domain with 250-m resolution, and a finer LES nest with 50-m resolution. The stable scenario set up uses four nests: a 990-m resolution mesoscale parent with nested LES domains at 90-m, 30-m, and 10-m horizontal resolutions. Sensitivity tests are performed on the highest resolution domain for each stability class (i.e., on the 50-m resolution domain for the convective scenario and on the 10-m resolution domain for the stable scenario).

Snapshots from the convective scenario simulations are shown in Figure 6.10. The finest, 50-m grid spacing domain is shown embedded in a portion of its 250-m resolution parent nest. Markers show a line of virtual tower locations at which profile data are extracted. For both convective and stable scenarios, the dominant low-level wind is from the south-southwest and the wind field of the convective scenario shows a clear "streaky" structure associated with convective rolls. Multiple tower locations are analyzed to gauge how errors might grow with distance from the inflow boundary and also to help establish robust comparisons between the physics sensitivity cases, since a slight shift in the position of a streak might cause a misleadingly large error at a single tower.
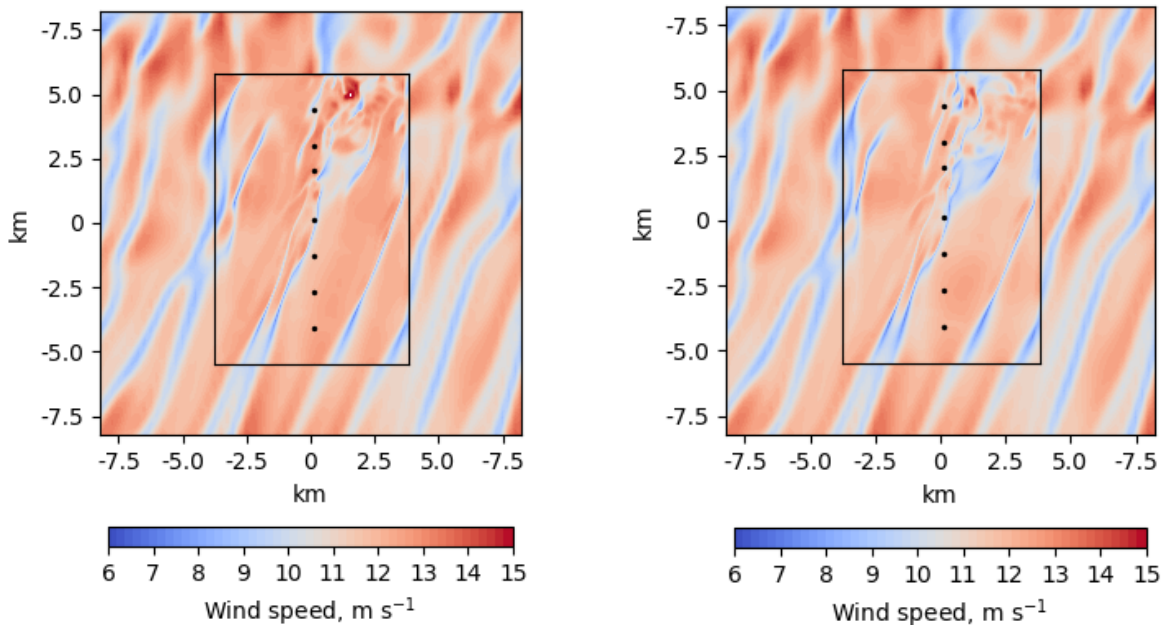
Figure 6.10. A snapshot of horizontal wind speed in the convective scenario at an approximately 90-m level after one hour of run time (Nov. 8, 2013, 19 UTC) of the offline-nested 50-m domain. The outer box is a portion of the 250-m parent domain, showing the alignment of flow structures across the nests. The "fully physics" case is shown on the left, and the "dry" physics sensitivity test is shown on the right. Dots indicate the virtual tower locations.

Means and variances of the velocity components and horizontal wind are computed over averaging windows of 30 and 10 minutes for the convective and stable scenarios, respectively. Time histories of absolute and relative errors and time-averaged root-mean-square errors

(RMSE) of 90-m wind speed and resolved turbulent kinetic energy were calculated for each of the sensitivity tests with respect to the offline-coupled, full physics simulation. The same analysis was repeated for the convective scenario using a 10-minute averaging window; this generally led to increased RMSE but did not change the relative ranking of the sensitivity test cases.

Figure 6.11 shows the relative difference in wind speed and resolved TKE at approximately 90 m above the surface as recorded at the fourth, centermost, virtual tower. The relative error of a variable is computed as the difference between the values of the variable obtained from the sensitivity test and full physics cases, divided by the value of variable in the full physics case. The ranking of error among the sensitivity cases was similar at each tower, although there is variability in the magnitude of the errors among the towers. Errors in wind speed did not show a clear pattern moving along the row of towers, but errors in TKE grew from the first virtual tower location, nearest the southern boundary, through the fourth tower. Moving northward from the fourth tower, the TKE errors either flattened or decreased. The temporal variations of the relative error of the wind speed and resolved TKE are similar, consistent with the magnitude of the velocity fluctuations being correlated with the magnitudes of the velocities themselves. However, while the relative error in 90-m wind speed is typically below 5% and does not exceed 10% over the analysis period, the relative error in TKE can be greater than 60% at this central virtual tower location.
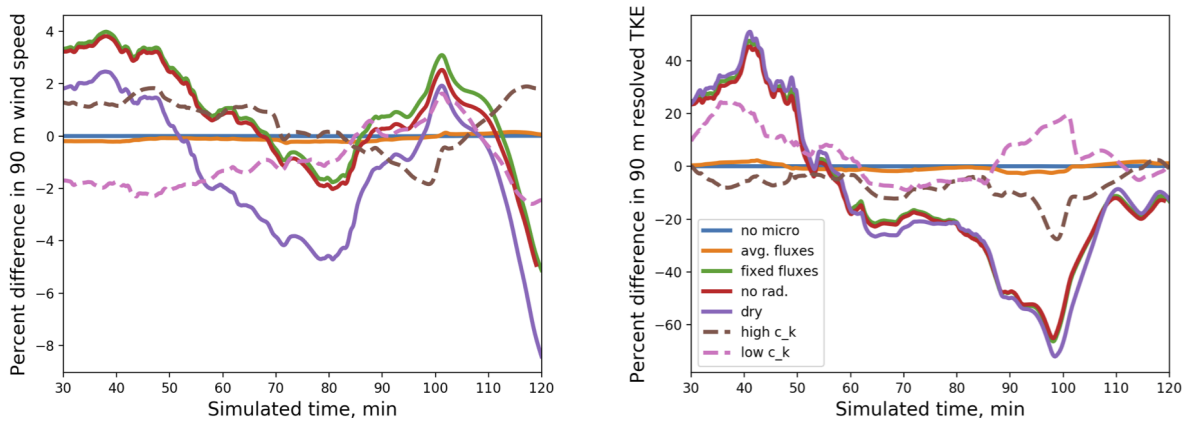
Figure 6.11. Percent differences in horizontal wind speed (left) and resolved 3D TKE (right) at a 90-m level as extracted from the centermost virtual tower during convective scenario simulations. Differences are computed relative to the full physics, offline-nested case. Note that the "no micro" case result (blue line) is mostly obscured by the "avg. flux" result (orange line) in both panels. Likewise, the "fixed fluxes" result (green line) is covered by the "no rad." result (red line) in the right panel.

As expected, in the absence of significant cloudiness and precipitation, turning off the microphysical scheme had virtually no effect on the results. Averaging the surface fluxes of latent and sensible heat in space, but retaining their temporal variation, also had a negligible effect on the predicted 90-m winds and turbulence. However, fixing the surface fluxes at their spatial and temporal mean values had a significant effect, producing errors in the wind speed of several percent. Additionally, neglecting radiative transfer had only an extremely minor impact. Also, neglecting virtual temperature effects (the "dry" sensitivity test) shifted the values of the error in 90-m winds while keeping the same pattern of peaks and valleys in the time history. Note that the mean value of sensible heat flux was 207.6 W m^{-2}, while the standard deviation of the domain mean over the period was just over 10% of the mean value at 26.6 W m^{-2}.

As a point of comparison, the sensitivity of the wind speed to changes in the surface flux specification is roughly commensurate with the sensitivity to the ±33% change in the turbulence model coefficient, c_k.

The same analysis is presented in Figure 6.12 for the stable scenario. A few features are notable. First, the magnitude of the errors in the 90-m wind speed are comparable to those obtained in the convective scenario, in both an absolute and relative sense. Percent errors in the TKE peak at values above 100%. However, it should be noted that the absolute error in the TKE is only about one-tenth as large as the absolute error of the TKE in the convective scenario, corresponding to an overall very low level of turbulence in the stable scenario. Notably, the errors in the wind speed show a very smooth temporal variation, despite the shorter 10-minute averaging window. This suggests that a flow feature that has a spatial scale comparable to the size of the LES domain is responsible for the differences in wind speed, rather than a mismatch in prediction of smaller scale turbulent variations. Inspection of snapshots of the flow field across the approximately 90-m vertical level (Figure 6.13) shows this is indeed the case. An anomalous structure forms near the western boundary of the finest domain in the sensitivity cases with fixed fluxes (bottom) that is not present in the full-physics offline (top) or online (not shown) nested domains. The anomalous structure extends through most of the depth of the domain and is observable in all velocity components as well as the potential temperature field. It is hypothesized that disturbances in the flow due to differences in the specified boundary conditions and the predicted interior flow field are amplified in the stable case in the absence of turbulent mixing.
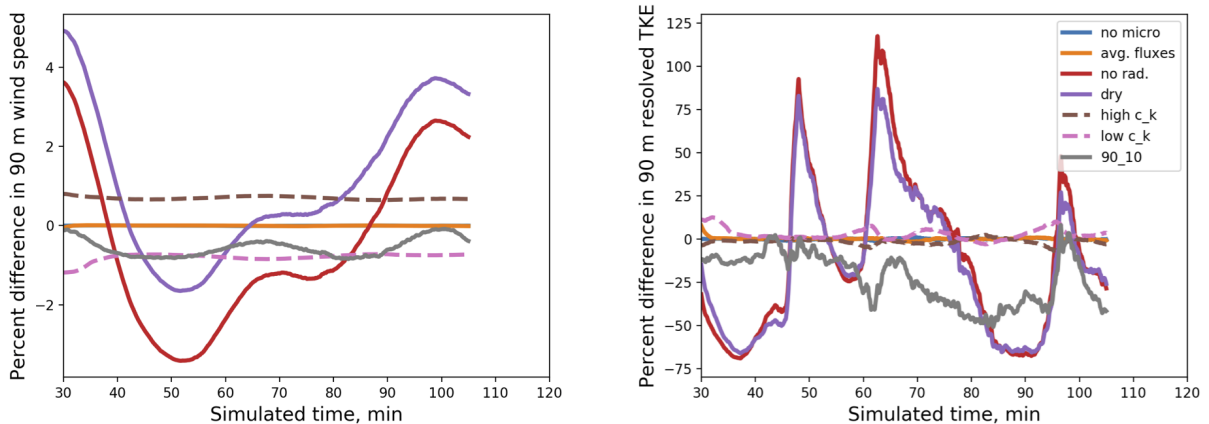
Figure 6.12. Percent differences in horizontal wind speed (left) and resolved 3D TKE (right) at a 90-m level as extracted from the centermost virtual tower during stable scenario simulations. Differences are computed relative to the full physics, offline-nested case. Note that the "no micro" case result (blue line) is obscured by the "avg. flux" result (orange line) in both panels.

Finally, we note that the differences in predicted wind speed produced by increasing or decreasing the turbulence model parameter, c_k, are generally slightly weaker than the differences produced by the same change in the convective case, and the magnitude of the difference is comparable to the change in wind speed observed when nesting from a 90-m resolution parent (the "90_10" case in Figure 6.12) rather than the 30-m parent used by the other stable cases.
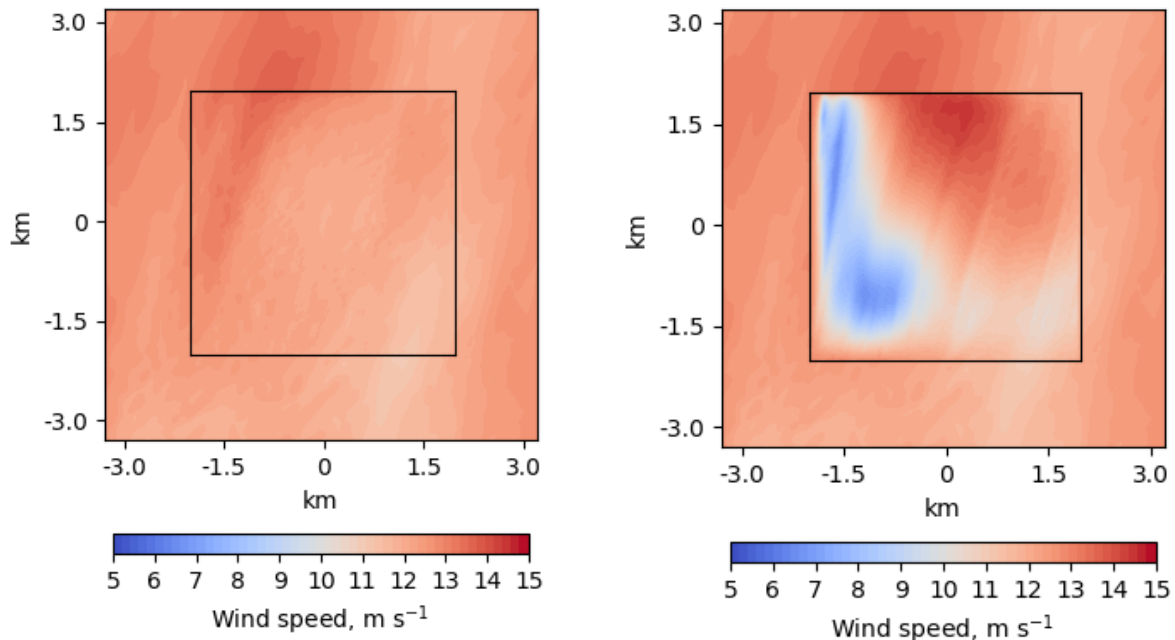
Figure 6.13. A snapshot of horizontal wind speed in the stable scenario at an approximately 90-m level after 1 hour run time (Nov 9, 2013, 2 UTC) of the offline-nested, 10-m domain. The outer box is a portion of the 30-m parent domain to allow the alignment (or misalignment) of flow structures across the nests to be seen. The "full physics" case is shown above the "dry" physics sensitivity test.

In summary, we undertook a study of the sensitivity of hub-height wind speed and turbulence levels to the treatment of atmospheric physical processes in high-resolution LES. Our approach to this study offers a framework that can be used to identify the appropriate range of resolutions at which to couple mesoscale and microscale atmospheric flow simulations. Using WRF-LES, which is equipped with a comprehensive suite of atmospheric physics parameterizations, we selectively simplified or turned off these parameterizations to mimic the typical capabilities of a microscale computational fluid dynamics solver such as Nalu-Wind. These WRF-LES sensitivity tests were driven by coarse WRF-LES inflow, emulating the boundary forcing approach that can be used to provide a microscale simulation with realistic inflow. Convectively and stably stratified flow regimes were considered based on the SWiFT diurnal cycle benchmark case previously identified and analyzed within the MMC project.

In both regimes, we found that hub-height wind speed and TKE were most sensitive to the representation of the temporal variation of the surface heat fluxes. While errors in wind speed were typically within a few percent of the mean wind speed, relative errors of the TKE were much larger. To give a scale for the importance of these errors, they were compared with the sensitivities associated with reasonable uncertainties in an important turbulence model parameter.

For this phase of our study, relatively simple conditions were selected, including flat terrain and clear, dry conditions. With greater surface heterogeneity, higher humidity, and cloudiness, physical processes that were not significant in this case study might grow in importance. We plan to examine this issue by expanding our study to additional sites in diverse environments that are relevant to wind energy.

7.0 Perturbation Methods

7.1 Overview

When forcing a turbulence-resolving LES with initial or boundary data that does not contain the full spectrum of turbulence motions that are resolvable upon the LES mesh, a transition occurs over which resolved-scale turbulence is generated within the flow. This transition region, referred to as a fetch, comprises the distance into the LES domain from the inflow boundary or boundaries over which the turbulence and other flow characteristics approach an equilibrium with extant forcing conditions.

The oldest and most common practice for simulating turbulent flow is to initialize a mean flow field with small amplitude perturbations to the velocity or, more commonly, potential temperature field and to run the simulation using periodic lateral boundary conditions (LBCs). Periodic LBCs permit flow exiting the domain to be recycled back into the upstream boundary or boundaries, creating an effectively infinite fetch over which turbulence can continue to develop until approaching a desired level of equilibration.

For highly idealized setups involving nearly steady and homogeneous forcing, statistics of the flow and turbulence fields, such as mean wind speed, turbulence kinetic energy, and spectral content, can be evaluated over time until those parameters converge to steady values. Those values can then be validated against either observations taken during similar forcing conditions or from a higher-fidelity simulation, such as a direct numerical simulation.

While the above approach to generating turbulent flow data works well for specific setups, it is limited to conditions that can be reasonably approximated with periodic LBCs. For general conditions not amenable to the approximation of periodicity, periodic LBCs cannot be used, and domain inflow and outflow must be prescribed differently. A primary implication of the inability to use periodic LBCs is that there is no longer an effectively infinite fetch over which the turbulence field can spin up and approach equilibrium, rather the fetch is constrained by the physical extent of the LES domain. This constraint places a premium on the ability of the simulation to spin up turbulence within a sufficiently short distance from the inflow to leave part of the domain available for analysis of the flow field and its interaction with turbines.

While turbulence eventually forms within the microscale simulation domain via nonlinearities in the governing flow equations, the process can be quite slow, especially when turbulence production mechanisms are weak relative to the speed at which flow traverses the domain. To address the sometimes slow rate of turbulence spin-up, various methods have been developed to accelerate turbulence development within LES domains not using periodic LBCs. Such methods can generally be classified among the following categories: 1) superposition of correlated turbulence motions onto a mean flow, 2) application of uncorrelated perturbations to flow field variables, and 3) use of turbulent flow generated from a precursor simulation, such as an offline LES. The inflow perturbation working group within the MMC project is evaluating representatives of these three categories of perturbation inflow methods, described below.

7.2 Description of Methods

7.2.1 Stochastic Cell Perturbation method (SCPM)

The stochastic cell perturbation method (SCPM, Muñoz-Esparza et al. 2014) entails application of rectangular patches of uncorrelated, stochastically generated perturbations to either the potential temperature (SCPM-T) or momentum (SCPM-M) field, along three consecutive strips extending into the domain from the inflow plane(s), as shown in Figure 7.1. Patches of correct sizes and amplitudes produce buoyant instabilities that rapidly amplify via the nonlinear dynamics represented by the governing flow equations, generating turbulence that is consistent with the forcing.
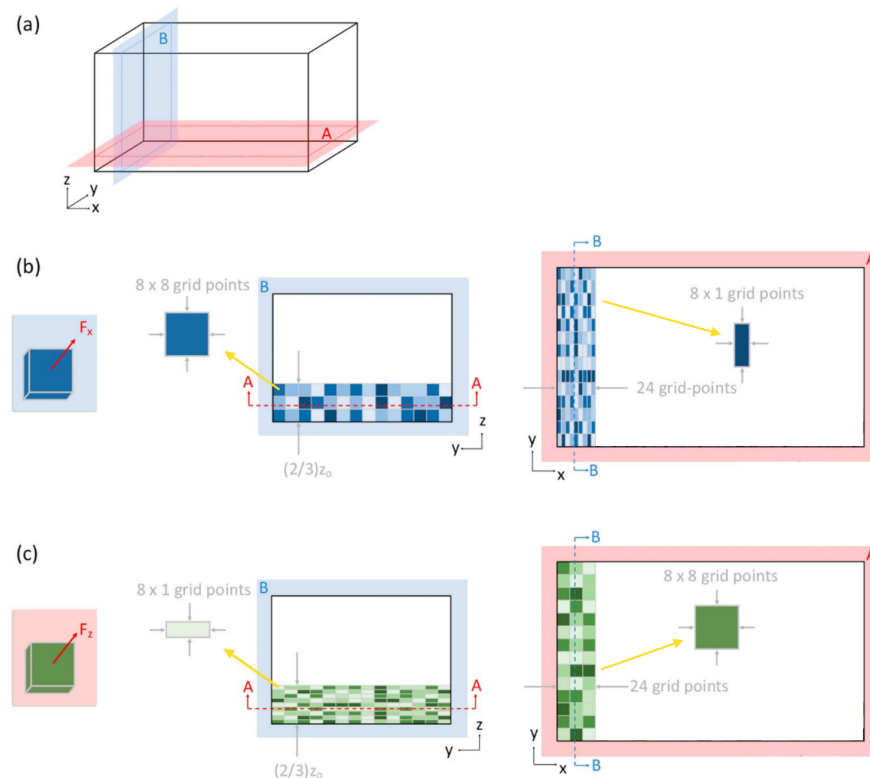
Figure 7.1. Domain schematic showing cross sections in the horizontal and vertical planes along which the stochastic cell perturbations (either thermal or momentum) are applied (modified from Mazzaro et al. 2019).

The approach is simple, computationally efficient, and highly general because the turbulence forms naturally based on the forcing and geometry of the domain rather than being imposed a-priori. The SCPM-T has been validated in idealized neutral (Muñoz-Esparza et al. 2014; Muñoz-Esparza et al. 2015), unstable (Muñoz-Esparza et al. 2014; Mazzaro et al. 2017, Muñoz-Esparza and Kosović, 2018), and stable conditions (Muñoz-Esparza et al. 2014; Muñoz-Esparza and Kosović, 2018). Optimal settings of the cell perturbation method were identified by Muñoz-Esparza et al. (2015) and Muñoz-Esparza and Kosović (2018) and its ability to produce realistic turbulence has been demonstrated in a variety of cases, including:

- A diurnal cycle in full-physics atmospheric simulations during the Crop/Wind Energy Experiment (CWEX-13) field campaign (Muñoz-Esparza et al. 2017),

- Multiple daytime scenarios corresponding to convective conditions during the Experimental Measurement field campaign (Muñoz-Esparza et al. 2018),

- A variety of semi-idealized scenarios dealing with ocean-island interactions and cloud formation (Jähn et al. 2016),

- A sea breeze over an urban-like coast (Jiang et al. 2017), and

- Flow over a real urban canopy (Lee et al. 2019).

Muñoz-Esparza et al. (2015) showed that SCPM-T performed better than the synthetic method of Xie and Castro (2008) in several metrics and significantly reduced computational overhead, as the Xie and Castro (2008) method requires either precursor simulations or analysis of high-frequency observations, to obtain required parameter values. SCPM-M has also been evaluated under neutral and unstable thermodynamic forcing in idealized flat terrain setups (Mazzaro et al. 2019), but has not been validated to the extent of SCPM-T.

Both SCPM-T and SCPM-M are examined herein, with the SCPM-T perturbation amplitude, timescale, and other aspects of the setup determined following Muñoz-Esparza et al. (2017), while those for SCPM-M followed the approach of Mazzaro et al. (2019), as shown in Figure 7.1.

7.2.2   Synthetic Mann method

Synthetic inflow turbulence methods, for which a correlated turbulence field is applied directly at the inflow plane(s), provide a means to potentially accelerate the generation of equilibrated turbulence significantly relative to methods requiring a nontrivial development fetch. However, as synthetic methods are predicated upon exact matches between the simulated flow conditions and the parameters used to generate the synthetic turbulence field, any mismatch will result in the need for a fetch over which the applied turbulence can equilibrate to the forcing. Additional computational demands and workflow complexity in obtaining parameter values to run the synthetic methods, either from precursor simulations or analysis of high-frequency measurements, should also be taken into account in evaluating the efficacy of such approaches. Herein we investigate one such method based on Mann (1998).

Synthetic turbulence generation methods, such as those of Mann (1998) and Kelley (2011), assume that the turbulence field is frozen in time and space. The spectral characteristics of the wind field at one point are determined using an empirical relation; for example, from Kaimal (1972). A coherence function is then used to estimate the spectra over the set of grid points defining the inflow plane. This frequency-domain description of the wind field is converted into the time- and space-domain using Fourier Transforms. These 2D planes of synthetic turbulence are generated ahead of time, archived, and applied at the inflow plane(s) of the domain during a simulation, at a specified time interval.

Herein, we use the Mann method to generate the inflow turbulence data. The Mann method is derived for sheared flow during neutral condition, for which shear production is the only TKE production mechanism. Figure 7.2 shows y-z and x-y slices of the u velocity generated from the Mann method. The spatial resolution is 12 m along the y-axis, and 10 m along the x and z directions. To generate turbulence that is comparable with that of the observations, the variance of wind velocity at hub height (~90 m) was obtained from the SWiFT tower observations. A length scale of 400 m (in this case not obtained from the tower observations) was also prescribed. The inflow plane is 6 km (500 grid points) in the crosswise (y) direction and 450 m

(45 grid points) in the z direction, covering approximately 60% of the boundary layer height, with the x-dimension containing 900 grid points. The turbulence structures occupy the entire plane and are statistically homogeneous along vertical and horizontal directions.
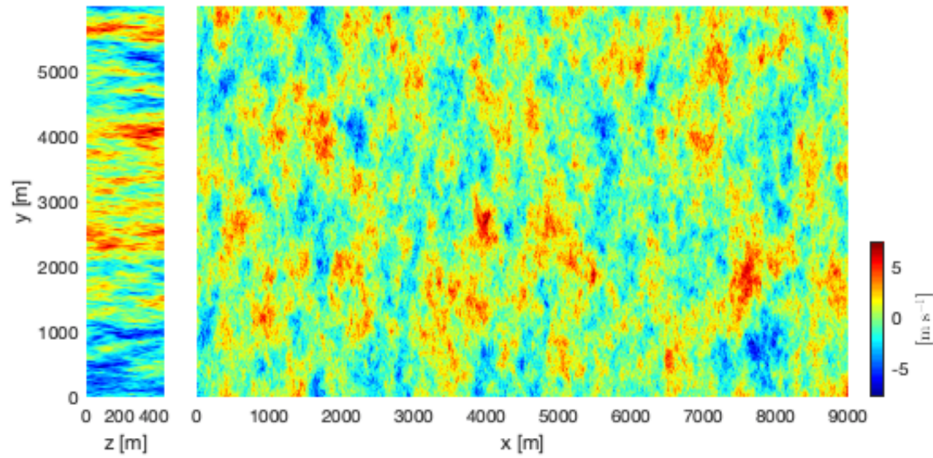
Figure 7.2. Representative (left) vertical and (right) horizontal planes of inflow turbulence data generated using the Mann method.

7.2.3   Synthetic TurbSim method

The project team also calculated a synthetic turbulent inflow velocity field using the TurbSim stochastic wind simulator. Output from this simulator is a time-varying inflow plane that is periodic in time. The velocity spectra of the turbulent field are dictated by the International Electrotechnical Commission (IEC) Kaimal model (Kaimal 1972), with an integral length scale of 340.2 m. A characteristic hub-height turbulence intensity (TI) of 10%, approximately the mean over the study period, was specified. This TI dictates the variance of the streamwise u velocity. Variances of v and w velocity (lateral and vertical components, respectively) are assumed to be related to the standard deviation of the streamwise velocity, σ_u; $\sigma_v = 0.8\sigma_u$ and $\sigma_w = 0.5\sigma_u$.

Spatial coherence in u is enforced between points in the inflow plane based on the International Electrotechnical Commission (IEC) coherence model; no coherence is enforced in v or w. Microscale simulation times are mapped to the TurbSim simulation that has a period of approximately 10 minutes (600 + δ s). For an input analysis period of 601 s and a perturbation frequency of 10 s, the small nonzero δ provides a longer unique series of inflow planes with which to perturb the flow.

The mean velocity profile, on which the turbulence simulation does not depend, is subtracted from the instantaneous inflow plane. The resulting velocity fluctuations are used as perturbations superimposed onto the mesoscale flow field. Three quantities calculated from the inner nest of the WRF mesoscale simulation were used: the resolved wind direction, modeled PBL height, and modeled TKE. The instantaneous magnitude of the velocity fluctuations is obtained from the hub-height TKE = $0.5(\sigma_u^2 + \sigma_v^2 + \sigma_w^2)$ and the assumed relationship between variances. At each timestep, the stress tensor is rotated to align u with the streamwise direction at hub height and then the velocity-component fluctuations are scaled by the square root of the ratio of the PBL- and TurbSim-modeled variances, noting that the TurbSim-simulated turbulence is stationary.

Because the TurbSim simulation does not account for the depth of the boundary layer, the fluctuating velocity field needs to be scaled such that the fluctuations vanish in the free atmosphere. We applied a hyperbolic-tangent scaling function centered at the PBL height. Fluctuations are scaled such that the magnitude of the fluctuations decreases from 90% to 10% over an ad-hoc distance of 100 m. To remain consistent with the simulated homogeneous turbulence field, the velocity fluctuations are uniformly scaled with height above the ground up to the capping inversion.

While the Turbsim method has undergone preliminary testing, formal assessment using the tools and methodology described below is not yet complete but is planned for early FY20.

7.3   Assessment Methodology

During previous years, methods based on the above approaches were developed and applied in various setups by different members of the project team. What has been lacking thus far is a systematic assessment of all the approaches in controlled setups, using the same assessment metrics. This year, the team developed a framework whereby each method could be examined using identical forcing and assessment, as required to evaluate strengths and weaknesses of various approaches. Below is a brief description of the simulation and analysis framework, presentation of preliminary results and analyses, and plans for future assessment activities.

7.3.1   Common framework for assessment

With multiple team members participating in development and evaluation of inflow perturbation methods, several different versions of the WRF model were being used, either to generate mesoscale inflow for offline LES, or to provide inflow to nested LES using online coupling. Analysis of the team workflow revealed an inability to perform the same idealized mesoscale runs, starting with common domain setups, modifications to various physics subroutines, and ingestion of initialization and forcing data sets. These discrepancies complicated the attribution of errors in assessment of the various perturbation methods under analysis. Moreover, each entity was using its own analysis scripts to compute various metrics, such as spectra and TKE, introducing another potential source of ambiguity into the assessment process.

In a parallel task during FY19, the MMC team undertook development of a community code and database repository in which the team would archive all of the components (including forcing and evaluation data sets, codes, and data processing scripts) required to set up, run, and analyze test cases using our codes that is described in Chapter 4. While this repository was being developed to facilitate engagement with the larger research and industry communities, we realized that our collective team required just such a framework to facilitate our own assessment. As such, the team decided to develop the inflow perturbation intercomparison study within this new framework, both to help with our own analysis and to demonstrate its efficacy to other potential users of our tools and procedures.

The three components of this framework include simulation codes, data sets, and analysis scripts. For the simulation codes, we instantiated our own branch of WRF, version 4.1, within the repository. We stipulated that all modifications to force the simulations, as well as the perturbation methods undergoing testing, be implemented into this code base, with formal vetting of correct implementation. This ensures both that each group can produce identical mesoscale inflow condition to test their perturbation methods, and that all perturbation methods are available to all members of the team, and others, for subsequent development or analysis.

The data sets utilized for the first assessment include observations from the TTU tower near the SWiFT facility during the diurnal cycle case of November 8-9, 2013. These data, while archived on the DAP, contain missing values, and also do not contain certain derived quantities useful to our analyses. We therefore developed a common set of data and simulation processing tools using a Python-based Jupyter Notebook environment, enabling the team to process raw input data in exactly the same manner and to compute and compare analysis metrics unambiguously.

Standing up this new common code development and analysis framework required nontrivial investments, both by the team members who created the repository and the scripts, and from team members who needed to learn new procedures involving GitHub, Python, and Jupyter Notebooks, as required to adhere to project-wide standard workflow practices. While the learning curve was substantial, the team now has a repository and set of procedures that can both facilitate all future team code development and analysis efforts, but also build in usability by other members of the community, as demonstrated below.

7.3.2   Assessment of Nov 8-9, 2013, diurnal cycle case

As described above, our assessment activity for FY19 focused on examining the various perturbation methods within the common assessment framework case studies based on the diurnal cycle occurring during November 8-9, 2013, at the SWiFT facility. As a first step, we tested the various methods using idealized convective, neutral, and stable case studies based on observed conditions at SWiFT. The case studies were constructed from analysis of 50-Hz data obtained at 10 heights between the surface and 200 m on an instrumented tower. The data were subsampled to 1 Hz and averaged to obtain mean and turbulence quantities over the 2 days. Time series of 10-minute average values of temperature, wind speed, wind direction, and TKE from November 8, 2013, are shown in Figure 7.3.
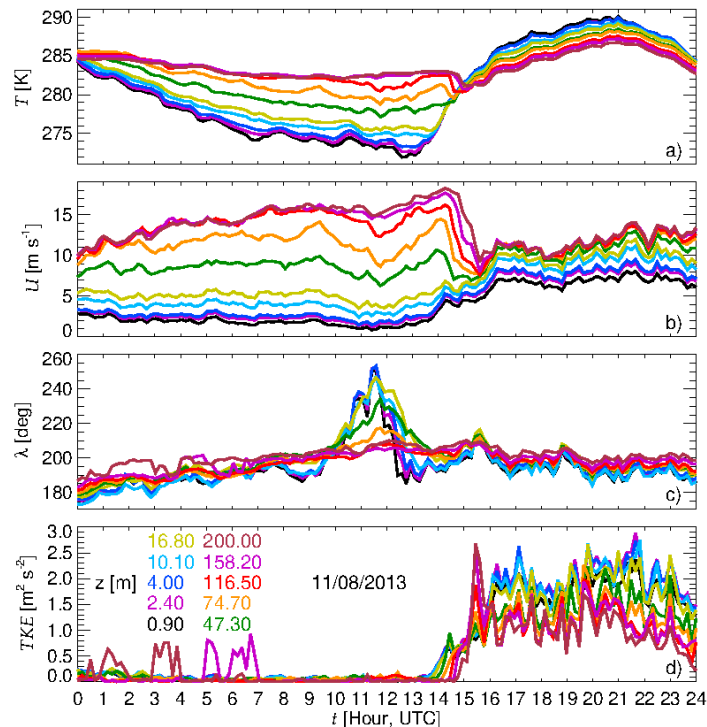
Figure 7.3. Ten-minute average (a) temperature, (b) wind speed, (c) wind direction, and (d) TKE from Nov. 8, 2013, observed at the SWiFT tower.

While the goal for FY19 was to complete examination of the various inflow turbulence generation methods in all three stability classes, the expenditure of resources to move to the common code and assessment framework prevented completion of the neutral and stable case studies at the time of the writing of this report. However, the convective case represents a template that the team will follow for the other stability classes, to be undertaken in early FY20.

The convective case study comprised the afternoon of November 8 from hours 18-20 UTC. This period was chosen due to the existence of high data acquisition and nearly steady wind speed, wind direction, and potential temperature profiles across the tower depth, with potential temperature increasing at a nearly constant rate due to surface heating (see Figure 7.3).

7.3.3   Computational setup

The mesoscale simulations used for the perturbation comparison were obtained using the MMC version of WRF from the team GitHub repository. The code includes modifications to the initialization and surface layer routines to allow user specification of latitude, roughness length, and heat flux values to enable idealized setups under a range of conditions, including variability of the Coriolis forcing, which influences rotation of the wind vector with height. This study used the standard Monin-Obukhov surface layer scheme (sf_sfclay_phys = 1) and the Yonsei University (YSU) PBL scheme (bl_pbl_physics = 1), while all other physics options (radiation, cloud, and surface) were turned off. The domain setup used 480 and 88 grid points in the horizontal and vertical grid directions, with grid spacings of 240 and approximately 4 m, respectively, with the vertical grid spacing stretched by approximately 5% per index with height, resulting in a domain top of 1606.5 m. The initial condition utilized a neutral potential temperature profile of 288 K up to 250 m, capped by a thermal inversion of 3.3 K km^{-1}, to prevent turbulence from reaching the domain top. This profile is an idealization based upon a mesoscale WRF simulation of the period at the time of local sunrise. A Rayleigh damping layer was used over the upper 400 m of the domain to damp oscillations and to force the free tropospheric temperature and wind fields toward specified values, the latter representing the geostrophic wind used to force the mean flow.

Because of the absence of measured values of key initial and forcing parameters, the initial temperature, geostrophic wind, surface heat flux, and surface roughness parameters were varied about a representative range of values, consistent with the observations and known characteristics of the site, and informed by previous mesoscale simulations of the period. The combination that provided the closest agreement with the observed wind speed and potential temperature profiles across the depth of the instrumented tower, representing processes most important to the generation of TKE, included z_0 = 0.01 m, H_S = 175 W m^{-2}, and Vg = 18.0 m s^{-1}. Rather than attempting to duplicate the observed wind direction, the angle of the geostrophic wind vector was instead modified to 297.6 degrees (yielding zonal and meridional values of (u_g, v_g) = (15.952,-8.3393) m s^{-1}) to align the flow with the x-axis of the simulation domain during the time period of interest, hours 6 to 8 of the simulation. This rotation allowed for a simplified setup, requiring application of inflow perturbations over the west inflow plane only, while also enabling the use of a rectangular LES domain, elongated in the streamwise direction, permitting a large fetch over which turbulence could develop, at a low computational cost. The change of angle has no impact on the solution, since all forcing parameters are horizontally homogeneous.

Figure 7.4 shows the evolution of the domain-averaged wind speed, wind direction, potential temperature, and vertical velocity profiles from the mesoscale simulations used to force the LES

domains, relative to the observed values of each quantity, 2 hours prior to, and spanning the 2-hour window during which assessment was performed.
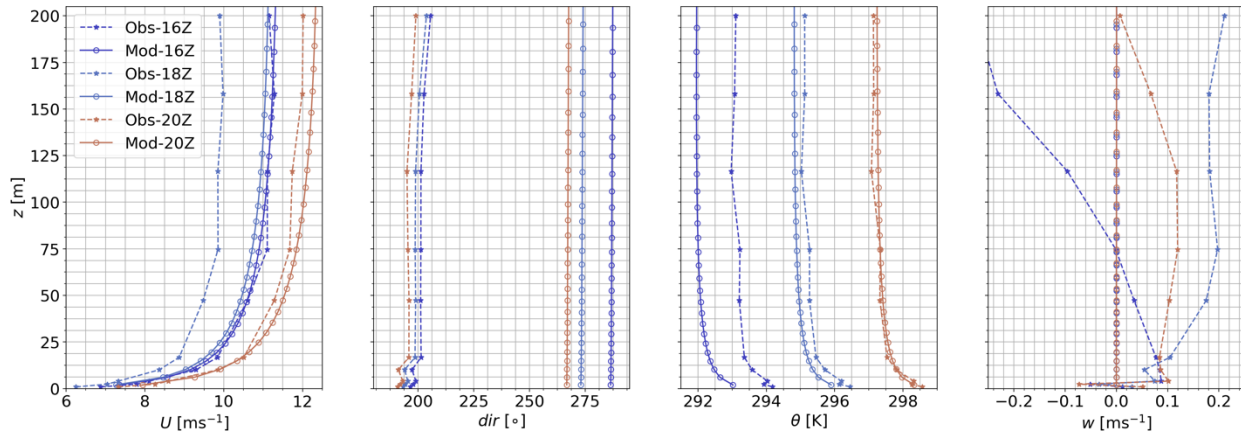
Figure 7.4. Mesoscale profiles at hours 16, 18, and 20 Z (=UTC) comprising the spin-up (16-18Z) and assessment (18-20Z) periods, versus centered 30-minute-averaged quantities observed at the SWiFT.

7.3.4   Assessment of perturbation methods

Although a goal of this study is to compare the simulated turbulence field to observations during the case study, a complicating factor in such comparisons is the absence of measured values of above discussed forcing parameters influencing the evolution of the turbulence field. While sensitivity experiments were performed to obtain representative values of these forcing parameters, showing good agreement with observed mean wind speed and potential temperature profiles across the tower, perfect agreement between simulated and observed turbulence data is neither expected nor achieved. This gap between the real and simulated forcing environments thus requires a tiered assessment approach. As the primary goal of the perturbation methods is to accelerate development of the turbulence field, assessment begins with comparison of the various perturbation methods to identical simulations conducted without any perturbations. Subsequent analysis will additionally compare the perturbed simulations against corresponding stand-alone LES conducted with the same forcing, but with periodic LBCs (such as employed by Muñoz-Esparza et al. (2015) and many others). This method provides a good proxy for the expected far-field behavior of the perturbed solution, since the perturbed and periodic setups are identical, and thereby embody the same assumptions and departures from real data, but with the periodic stand-alone domain providing an essentially infinite fetch for turbulence development. Comparison against observed turbulence data will augment these assessment methods, providing a rich global assessment of the performance of the various inflow perturbation techniques, relative to uncertainties in the forcing parameters and limits of the computational setups.

7.3.4.1   SCPM using online WRF

The SCPM was examined by nesting an LES domain directly within the described mesoscale domain, all within the WRF model. The grid size in the nest was reduced by a factor of 20, yielding a horizontal grid spacing of 12 m and a grid aspect ratio of 3 at the surface, which has been shown to work well in many WRF-LES studies. The nest contained 960 x 480 grid cells in the x- and y-directions, respectively. The velocity and temperature fields were output at 1-

minute increments over the entire domain, while an array of 20 x 10 vertical columns equally spaced in the x- and y- directions were also output at 10 Hz for comparison against high-frequency tower data. The LES utilized the 1.5-order TKE subgrid-scale (SGS) model to facilitate comparison against other codes used within the project that also employ this closure.

7.3.4.2   NO-SCPM

For the first phase of assessment, a simulation was performed with no perturbations at the inlet ($x = 0$) of the LES domain (NO-PERT). A summary of the results from NO-PERT is shown in Figure 7.5 within which several flow parameters and analysis metrics from approximately 90 m above the surface are displayed. The top left panel shows instantaneous contours of the streamwise flow component (u), overlayed by colored lines indicating 11 distances from the inflow at which the quantities shown in the other figure panels are computed. The fourth panel from the top in the left column shows instantaneous values of the vertical velocity (w). Between the two contour plots are spectra of the u velocity, and cospectra of the u and w velocities, computed along the y-direction, and averaged over all times, at each of the 11 analysis locations. The right column shows relative frequency distributions approximating probability density functions (PDFs) of w over the 2-hour analysis window at each of the 11 locations, whereas the lower left panel shows values of the skewness and kurtosis of w as functions of distance from the inlet.

The results displayed in Figure 7.5 indicate the slow development of turbulence, even under moderately strong convection, in the absence of inflow perturbations. Neither the u nor w velocity contours show turbulence features until beyond 5 km from the inflow, after which other metrics indicate very slow development of the turbulence field with distance. The spectra and cospectra demonstrate this slow development via a surplus of energy at small wavelengths following the first appearance of turbulence, followed by gradual increases at larger wavelengths with increasing distance. The PDFs indicate even more clearly than the spectra and cospectra how the turbulence field evolves, as the PDFs continue to change as the flow approaches the end of the domain. For NO-PERT, the fetch dependence of the skewness and kurtosis are difficult to discern from the lower left panel, due to the large kurtosis value occurring prior to turbulence initiation. However, the skewness and kurtosis values shown on the insets within the PDFs indicate that convergence has not been achieved within the extent of the domain.

7.3.4.3   SCPM-T

Figure 7.6 shows the same fields and analyses from the NO-SCPM simulation setup, but with SCPM applied to the potential temperature field at the inflow plane. All panels in Figure 7.6 indicate significantly earlier onset of turbulence using SCPM-T, followed by much faster equilibration, with quasi-convergence of all parameters by approximately 6 km from the inflow. Furthermore, comparison of the PDFs between Figure 7.5 and Figure 7.6 highlights the much more rapid appearance of non-Gaussianity following application of SCPM-T, as expected under convective forcing, which gives rise to relatively fewer but larger magnitude convergent and updraft flow motions, versus relatively more numerous but weaker diverging downdraft flow motions.
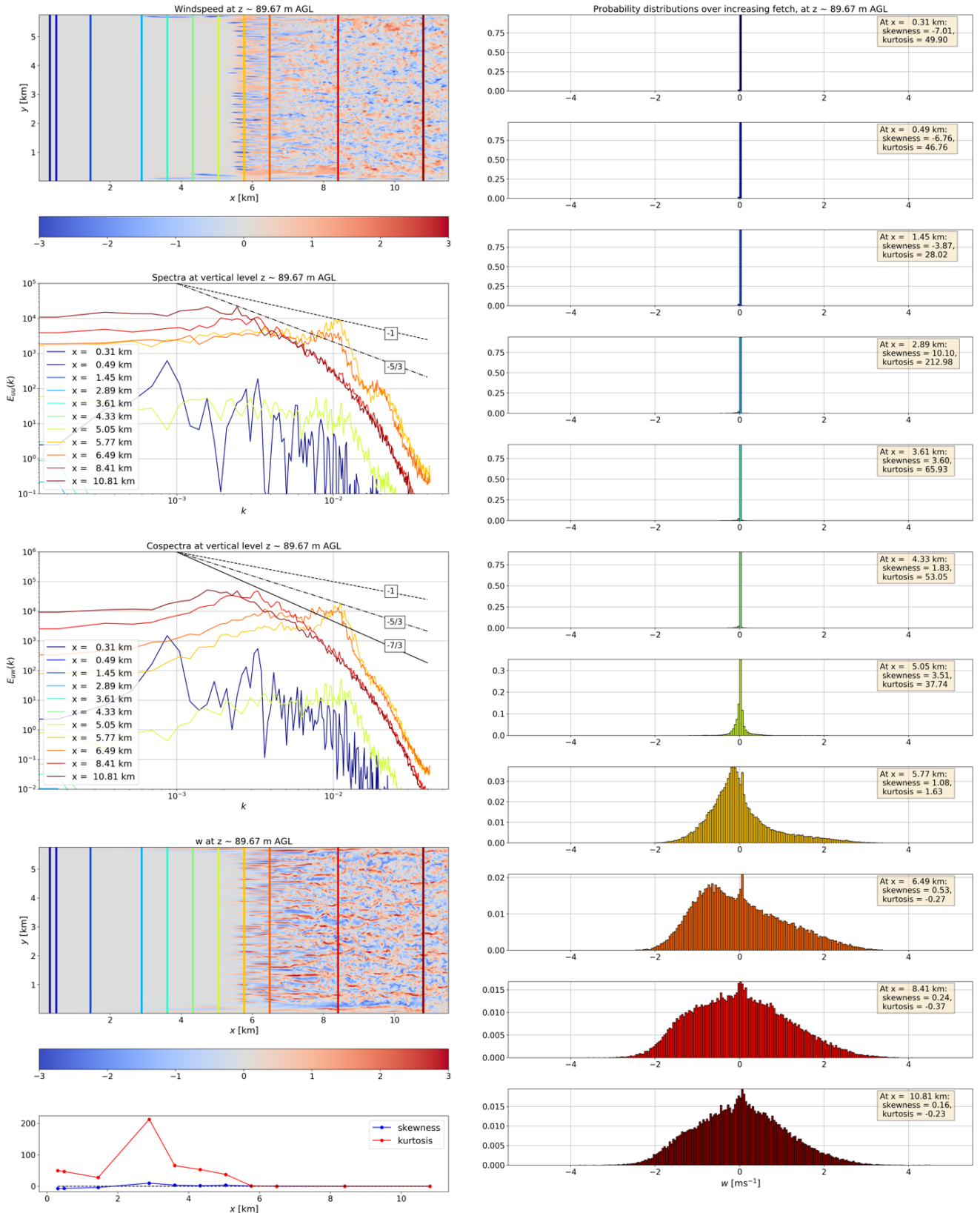
Figure 7.5. Microscale assessment results from the base case without any turbulence instigation methodology (NO-SCPM).
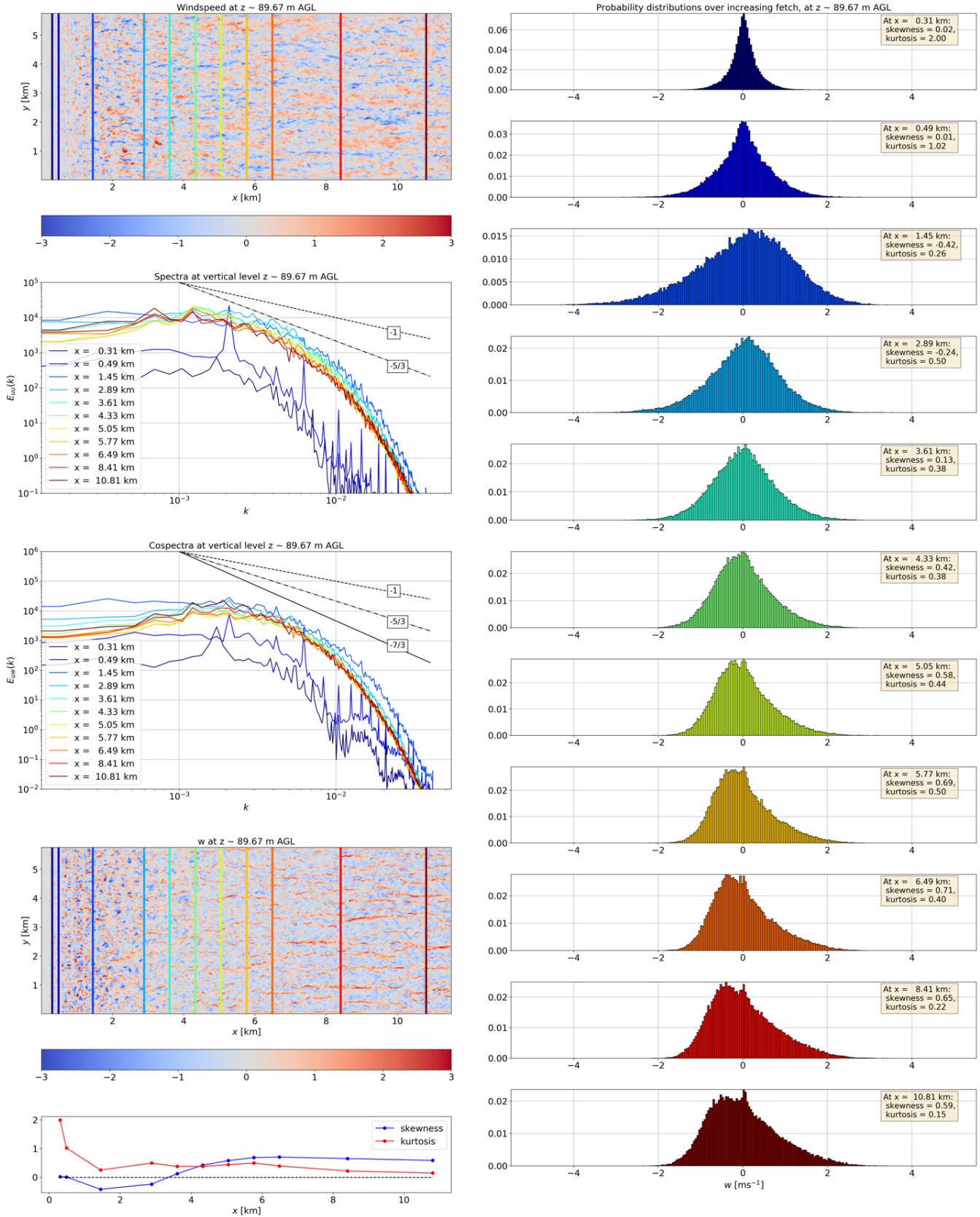
Figure 7.6.   Microscale assessment results using the SCPM-T approach.

7.3.4.4   SCPM-M

Although the SCPM-T uses buoyancy forcing to initiate fluid motions that then evolve into turbulence, an alternative application of the SCPM is to perturb the velocities directly, using the "force" or "momentum" approach, SCPM-M. The motivation for SCPM-M is a capability to accelerate turbulence formation, relative to SCPM-T, by proving an ability to more rapidly generate larger fluid motions nearer to the inflow plane(s). However, a concern of the SCPM-M is that the fetch required for this perturbed velocity field to subsequently develop into coherent turbulence, consistent with the governing flow equations, may be larger since SCPM-M imposes a velocity field that is not initially consistent with the governing equations, rather than working through the buoyancy forcing mechanism as SCPM-T does.

To compare these two approaches, momentum perturbations were introduced into the flow via a method similar to SCPM-T with a few key differences. First, although SCPM-T imposes thermal perturbations immediately and directly onto the potential temperature field, leading to immediate buoyant forcing as the equations are integrated forward in time, SCPM-M is implemented via application of a tendency, or time rate of change, to the prognostic equation governing the affected velocity component(s). Hence, SCPM-M requires several model time steps to influence the velocities, with the rate of influence controlled by the amplitude of the forcing. Since WRF's governing equations prognose the product of the velocity and the mass contained in the vertical column containing each model grid point, the optimal amplitude for the momentum perturbation depends upon the mass in each column, which in turn, depends upon the pressure field and the depth of the computational domain. Since, as yet, no general formula exists for computing the optimal magnitude for SCPM-M based on those physical and computational factors, we follow Mazzaro et al. (2019) and investigate a range of coefficient values that multiply the stochastic perturbations, obtained from a random number generator in the range of [-0.5, 0.5], centered about 0. While we analyzed simulations using all six of the forcing amplitudes examined in Mazzaro et al. (2019), here, for brevity, we discuss results using a subset of those runs.

Figure 7.7 and Figure 7.8 show results from SCPM-M applied to the horizontal momentum components only, using amplitudes of 2,000 and 5,000, respectively, whereas Figure 7.9 and Figure 7.10 show results applied only to the vertical momentum component using amplitudes of 5,000 and 10,000, respectively, with all results presented in the same format as for NO-PERT and SCPM-T.

As Figures 7.7–7.10 demonstrate, all of the simulations using SCPM-M feature accelerated turbulence generation relative to NO-SCPM (Figure 7.5). For all cases, the larger amplitudes, whether acting on the horizontal (Figure 7.7 and Figure 7.8) or vertical momentum components (Figure 7.9 and Figure 7.10), generate turbulence nearer to the inflow, with the largest-amplitudes results comparing qualitatively well with the SCPM-T results (Figure 7.6). However, a careful examination of the spectra and the PDFs reveal that aspects of turbulence development arising from SCPM-M differ from those of SCPM-T. For example, SCPM-M applied to w produces the most rapid equilibration of the smallest wavelengths of turbulence, while the application to w with the largest amplitude also achieves the most rapid convergence of the skewness. However, all of the SCPM-M results show slower convergence of the large-wavelength spectral energy, which continues increasing with fetch, and to higher values than for SCPM-T. Further examination, described in the following section, is required to better understand the differences between SCPM-T and SCPM-M.
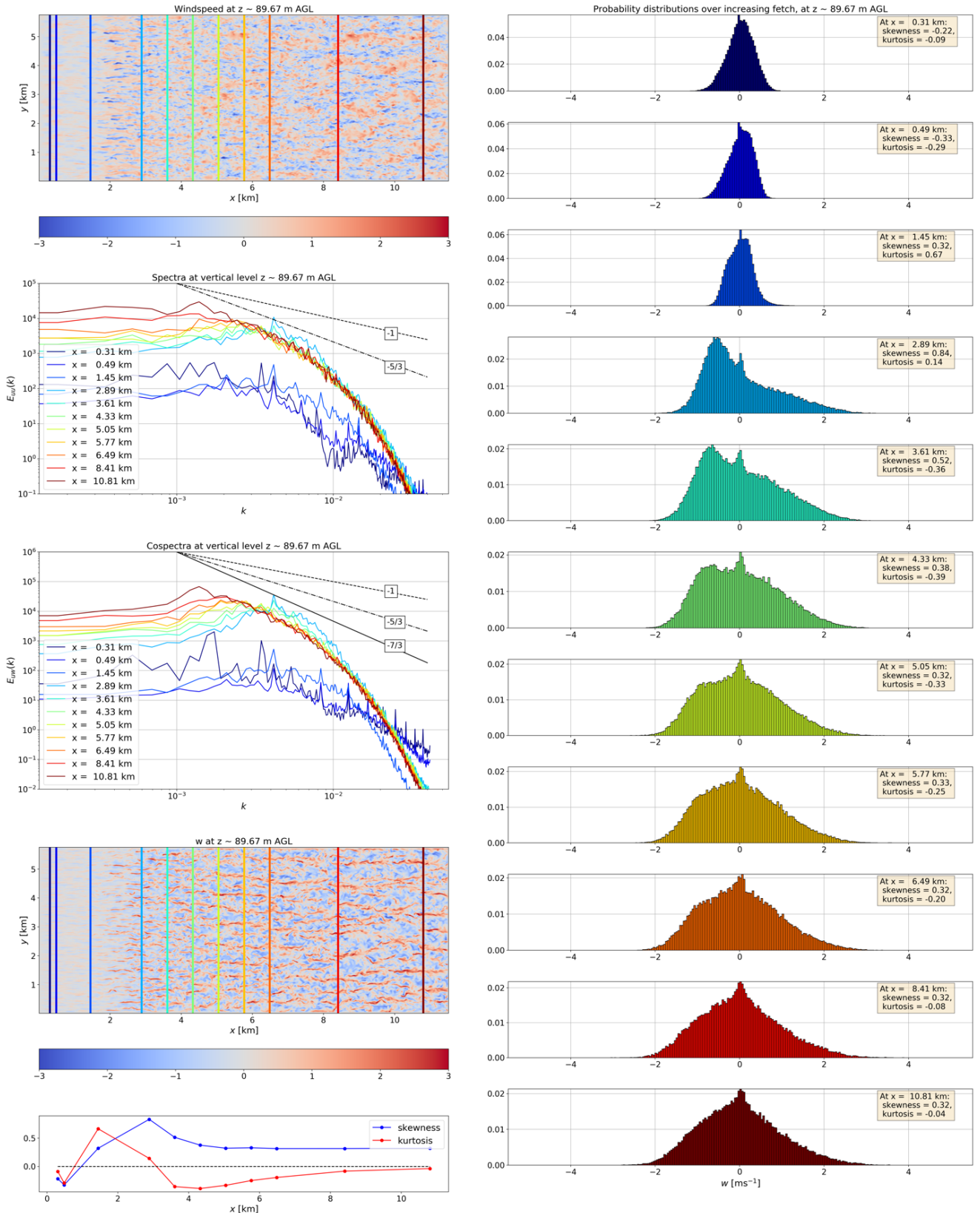
Figure 7.7. Microscale assessment results from SCPM-M applied to the horizontal momentum components, with a perturbation amplitude of 2,000.
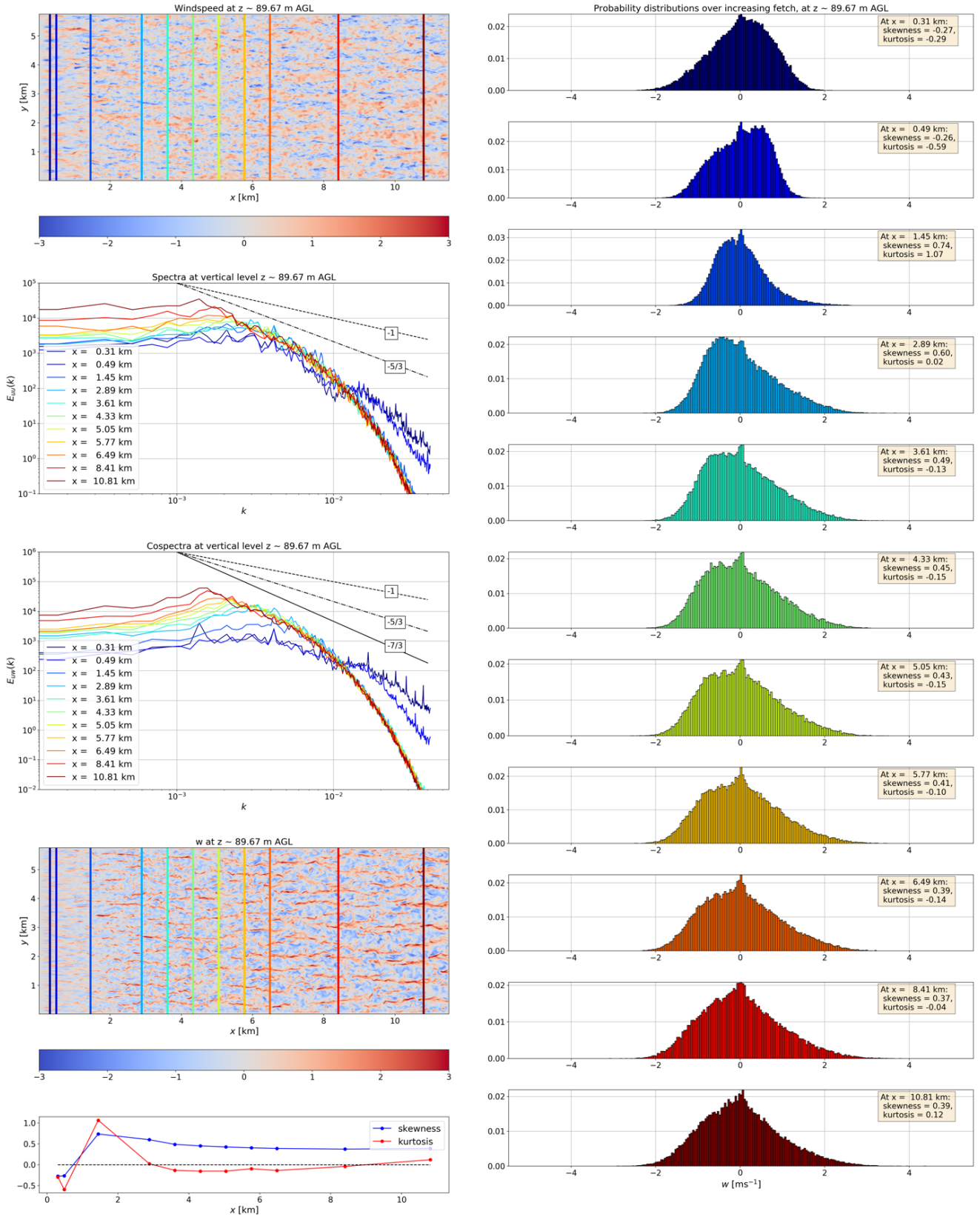
Figure 7.8. Microscale assessment results from SCPM-M applied to the horizontal momentum components, with a perturbation amplitude of 5,000.
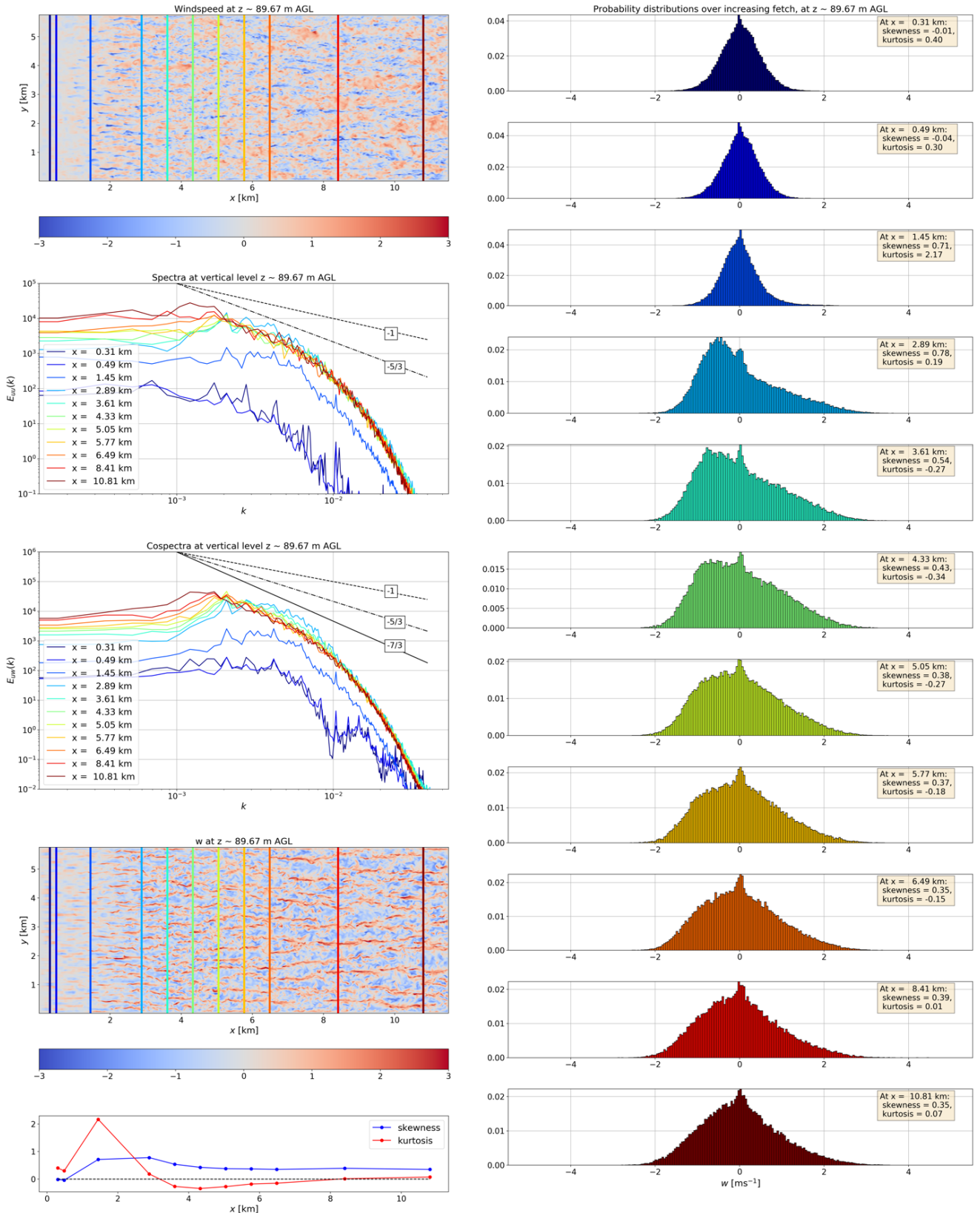
Figure 7.9. Microscale assessment results from SCPM-M applied to the vertical momentum component, with a perturbation amplitude of 5,000.
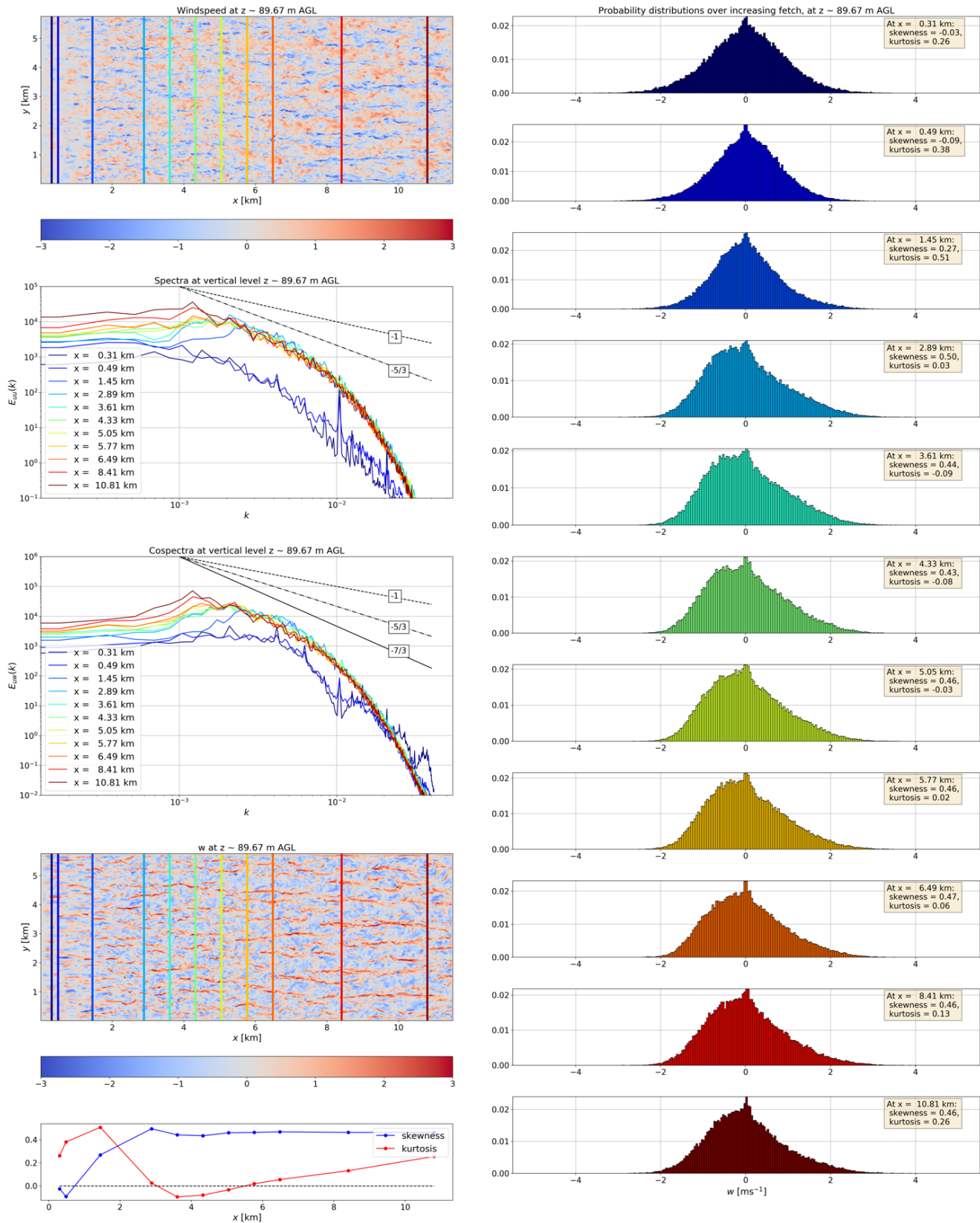
Figure 7.10. Microscale assessment results from SCPM-M applied to the vertical momentum component, with a perturbation amplitude of 10,000.

7.3.4.5　Synthetic Mann method

Figure 7.11 shows an example of application of the Mann method for the same idealized setup as used for the SCPM analysis, with the synthetic inflow turbulence again applied to the west inflow boundary of nested domain d02. In this implementation, the synthetic inflow data are provided at 2-minute frequency and linearly interpolated in time to the simulation time. The simulated flow field was saved in the same format as the SCPM simulations. The top panel in Figure 7.11 shows a horizontal slice of u-component of velocity at 100 m above the surface at 1900 UTC after 9 hours of applying synthetic turbulence. The bottom panel in Figure 7.11 shows the vertical slice of u-component of velocity that passes through the middle of the west boundary. Both flow fields show the presence of turbulent flow structures immediately at the location of the inflow boundary, after which the turbulence persists throughout the extent of the domain.
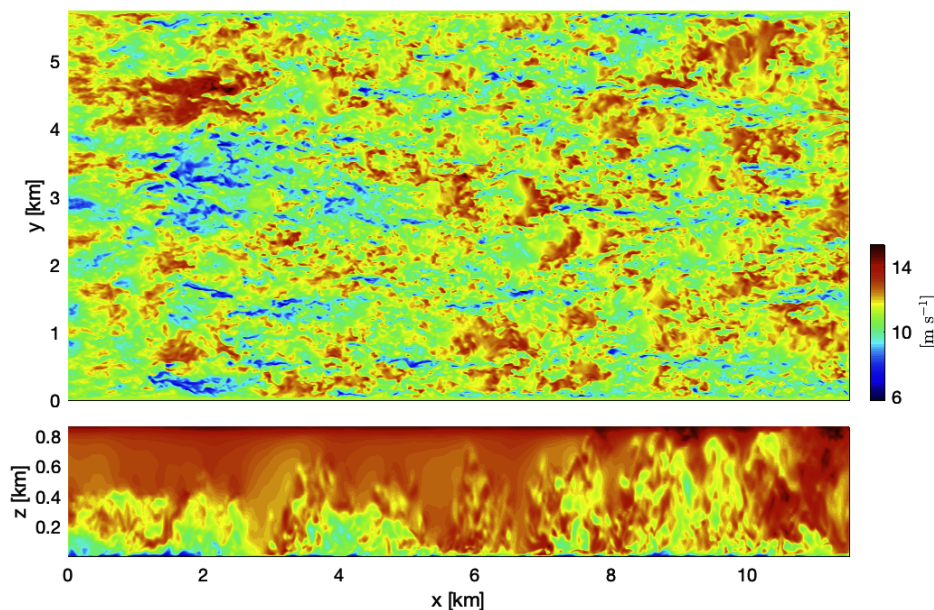
Figure 7.11.　Horizontal (top) and vertical (bottom) slices of u-component of velocity from simulated flow field using the synthetic Mann method.

7.3.4.6　Application of the MMC tools framework to the synthetic Mann method

While Figure 7.11 shows that the synthetic Mann method readily imparts flow structures that appear turbulent immediately at the inflow into the domain, differences in the turbulence morphology relative to the NO-PERT and the SCPM solutions are apparent. The project assessment tools and metrics framework was applied to these simulation results, providing both a more thorough understanding of the nature of these differences and, importantly, identification of a parameter value used in the synthetic method that can be rescaled to potentially improve agreement with the SCPM approaches. This analysis, in turn, motivated the introduction of additional metrics that can better inform the overall assessment process in quantifying the strengths and weaknesses of various approaches going forward.

Figure 7.12 provides assessment of the Mann method in the same framework as the other methods (Figs. 7.5–7.10) to facilitate comparison. Key differences include spectra and cospectra that are between one and two orders of magnitude greater for the Mann than the other methods and noticeably broader PDFs throughout most of the domain. As described earlier, the length scale of 400 m used in the synthetic turbulence generation is hypothesized to

be responsible for the bulk of these differences, having been prescribed a value that is likely much larger than is appropriate for the extant forcing conditions. Determination of a more appropriate value from the SWiFT tower data is underway.
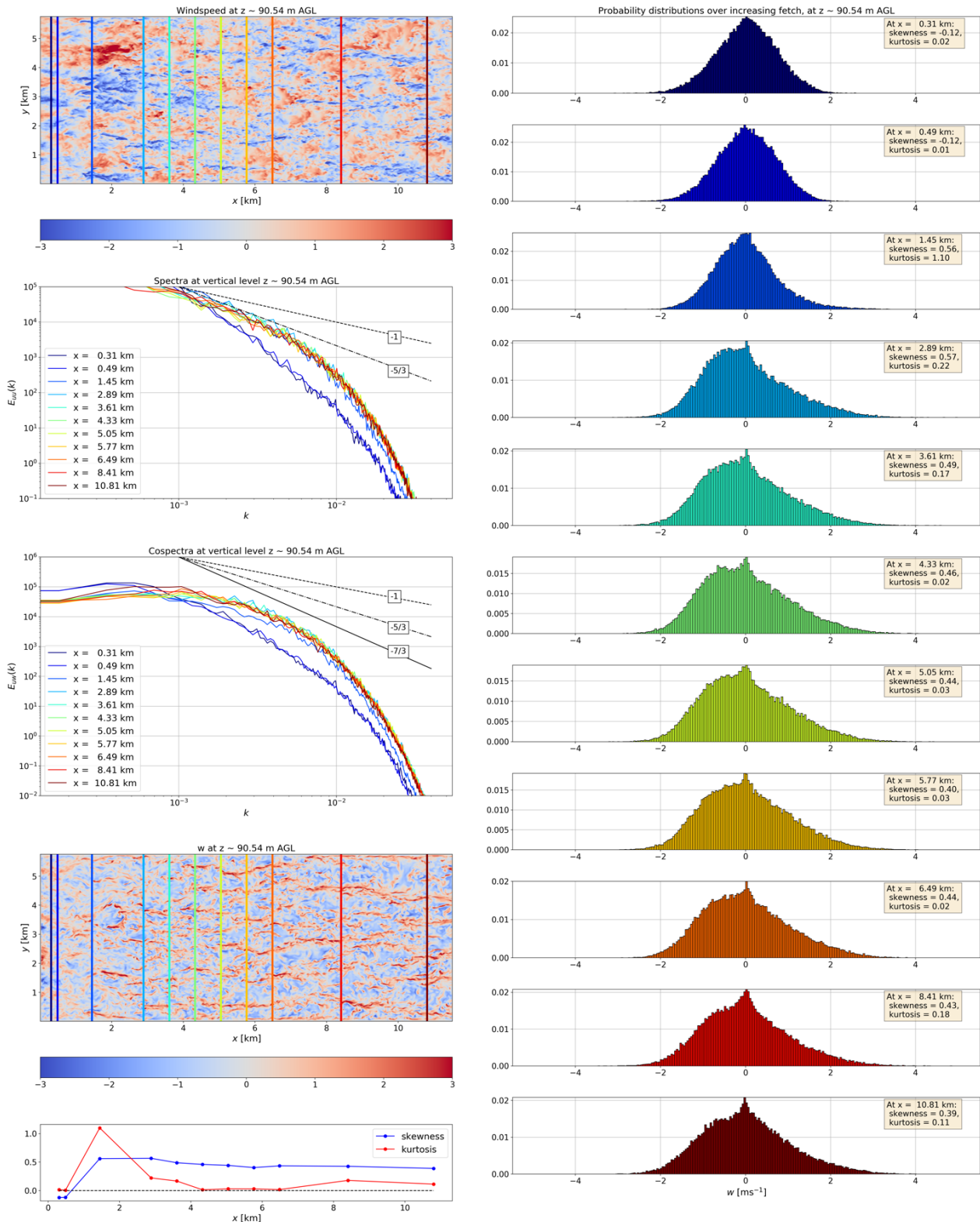
Figure 7.12.   Microscale assessment results from the synthetic Mann method.

7.4   Summary and Future Work

Herein, assessment of several inflow perturbation methods, intended to accelerate the formation of turbulence in turbulence-resolving LES forced by mesoscale inflow data, was performed. This assessment was performed using a new simulation and assessment framework developed by the team this year to facilitate formal assessment of codes and procedures applicable to MMC. The new simulation and assessment framework was demonstrated in a case study from the SWiFT facility, a site with relatively uniform surface cover and smooth terrain, comprising the convective portion of a typical diurnal cycle, under quiescent meteorological conditions.

Three different inflow perturbation methods were examined, relative to an unperturbed "control" simulation, all using identical mesoscale forcing and using the same assessment scripts and resulting performance metrics. Analysis reveals that, in the absence of any inflow perturbations, turbulence initiation requires about 5 km to develop, after which the developing turbulence slowly evolves through the remainder of its transit through the domain, never achieving steady values of key turbulence parameters within the extent of the domain. Each perturbation method examined herein significantly accelerates the onset and evolution of turbulence, producing nearly equilibrated turbulence statistics over the same distance as required just to initiate the turbulence field in the absence of any treatment at the inflow boundary.

Among the methods examined, the stochastic cell perturbation method, applied to the potential temperature field (SCPM-T), has undergone the most development and validation in similar atmospheric-boundary-layer flow simulations to those conducted herein. Application of the method with the published optimal parameter settings herein yielded results consistent with those presented in the literature. A variant of the SCPM for which the perturbations are applied directly to the momentum field (SCPM-M) was also assessed. In the absence of similar published guidance on the optimal perturbation amplitude, SCPM-M was run with several different amplitudes. While the study demonstrates the potential of SCPM-M to perform similarly to SCPM-T, provided the correct amplitude information, the absence of practical guidance on optimal perturbation amplitudes complicates application of the method, relative to SCPM-T.

Analysis of the synthetic Mann method likewise demonstrated applicability to turbulence inflow generation, producing results that were comparable to the other methods. Notable differences between the Mann method relative to the SCPM variants included the appearance of turbulence nearer to the inflow plane of the microscale domain, somewhat wider PDFs, and significantly larger spectral energy contents. The latter two differences are hypothesized to have resulted from the large value of the length scale used by the turbulence generation algorithm, with testing underway to evaluate the impact of reducing that parameter.

The study also demonstrated an important new element of the team workflow, the common code and assessment framework. The ability of the team to produce identical forcing and run identical assessment scripts eliminated ambiguities in the detection and attribution of differences that had previously arisen from inconsistencies in how various members of the team chose to set up and force their simulations and conduct and present analyses. Examples of the payoffs resulting from the collective investment by the team into a common evaluation framework include the ability to rapidly assess the impacts of different perturbation amplitude values for SCPM-M and the straightforward identification of the length-scale as a likely factor in the enhanced spectral energy contents and wider PDFs using the Mann method.

It is important to emphasize that the assessment described earlier does not, by itself, determine the ultimate accuracy of any of the above described methods. Other metrics and approaches

must be incorporated to assess accuracy. However, the analysis described thus far does clearly demonstrate how the use of a common simulation and assessment framework can greatly assist both the detection of differences that would be difficult to ascertain in similar but nonidentical setups and analyses and generate hypotheses regarding the sources of those differences.

Additional metrics under development to augment the evaluation of these and other methods include TKE and fluxes of heat and momentum, each highly applicable to wind energy applications. An additional method to assess the methods will be to conduct stand-alone LES with the same forcing but with periodic LBCs, a technique to provide proxies for the expected far-field equilibration values of many of the previously described assessment metrics, including PDFs and their characteristics, spectral content, TKE, and fluxes. Finally, the simulations will be compared against the observed data to provide a rich qualitative and quantitative comparison of the various perturbation methods under examination by the team.

The capability of analyzing these and other metrics in the time domain is undergoing final testing prior to incorporation into the MMC assessment toolkit repository. For the current scenarios under investigation, where the domain is flat and inflow conditions evolve slowly, spatial characterizations as performed herein yield more robust statistical convergence than time domain analysis. However, under more general environmental conditions, including unsteady meteorology, complex terrain, and heterogeneous surface characteristics, such as waves and land-sea contrasts, time domain analysis will be required. Evaluation of these and other perturbation approaches in complex terrain and offshore conditions is planned for FY20.

8.0   Improvements in Near-Surface Physics

8.1   Using Artificial Intelligence for Surface Layer Parameterization in WRF

The MMC team is exploring using a machine-learning approach to represent the atmospheric surface layer in replacement of Monin-Obukhov Similarity Theory (MOST; Monin and Obukhov 1954). Its goals are to: (1) determine the best representation of heat, momentum, and moisture fluxes by training random forest and artificial neural networks and (2) test these auto-encoded representations in WRF compared to standard parameterizations that use MOST. We use surface layer data sets for the KNMI-mast at Cabauw, Netherlands, and the National Atmospheric and Oceanic Administration Field Research Division tower in Idaho. Our data are split so that two-thirds of the years were used for training and one-third for testing. Both random forecast (RF) and artificial neural networks (ANN) were tested. The mean absolute error and correlation (R^2) were used to compare the machine-learning predictions and the observations on the test data set. We found that the RF and ANN models generally improved upon MOST for estimating friction velocity, temperature scale, and moisture scale. Additionally, we found that a model trained on Idaho data and applied to Cabauw's test data set (and vice versa) showed generally lower errors and higher correlations than MOST, which provides evidence of the robustness of the machine-learning models.

We implemented the random forest surface layer parameterization subroutine in WRF and performed initial WRF single column runs using the second global energy and water cycle experiment atmospheric-boundary-layer study (GABLS-II; Beare et al. 2006) idealized forcing. The initial analysis represents a series of 3-day WRF runs with different random forest and WRF settings and compares them to the default WRF surface layer scheme and idealized slab land surface model. We further reduced the number of input variables and removing counter-gradient fluxes resulted in the best-performing WRF run so far in the preliminary analysis. We have begun writing a manuscript to be submitted to the *Journal of Advances in Modeling Earth Systems*, titled, *Machine Learning Parameterization of the Surface Layer*.

As part of the MMC project, we plan to address remaining issues with the land-based machine-learning surface layer parameterization and transition the approach for use in the offshore environment. First, we will test the ANN parameterization in WRF and determine whether its smoother predictions produce better or worse results within WRF than the random forest. We will perform regime-based interpretation of the machine-learning models to determine how the importance and sensitivity of different variables change when transitioning from unstable to stable regimes. To support offshore wind prediction, we will develop an ocean surface layer parameterization using available meteorology and flux data from buoys and potentially ship-based field programs. We will then implement both the land surface layer and offshore surface layer parameterizations together in WRF and evaluate them across selected case studies covering a range of weather regimes.

8.2   Additional Surface Layer Methods for the Marine Environment

Two additional methods that can be applied to improving the surface boundary condition over water include those based on the addition of forcing terms to the momentum equations and immersed boundary methods. Each of these approaches can enable the representation of

surfaces of arbitrary shapes, such as waves of any amplitude, and furthermore, can enable those features to change shape in time and space.

Methods based on supplying a force to the momentum equations typically utilize drag coefficients to retard the flow, either in applications involving forest canopies, for which drag terms approximate the effects of vegetation extending into the surface or boundary layer (e.g., Shaw and Patton 2003) or in urban areas where large momentum sink terms can approximate the effects of buildings, causing the flow to deflect around and over such "virtual buildings" (e.g., Chan and Leach 2007). Moreover, canopy methods have been shown to be extensible to idealized flat, rough surfaces where they can provide improved fidelity relative to the standard MOST approach (Arthur et al. 2018).

While wave height can be specified as the explicit bottom boundary in any computational fluid dynamics model, simpler approaches may generate sufficient fidelity, depending upon the application, and moreover, allow models such as WRF that use a terrain-following vertical coordinate, to represent the effects of steep wave slopes without incurring increased numerical errors (e.g., Lundquist et al. 2012).

Canopy approaches could potentially be modified to the marine environment to account for unresolved drag and pressure effects, either in applications for which the wave features are entirely subgrid, or at higher resolution where the canopy shape profiles could be modified in time and space to represent resolved sea-state features. For wave-resolving simulations, the application of large momentum sinks could be applied to generate virtual waves, analogous to the virtual building approach. These approaches could potentially be combined, whereby canopy methods could approximate, for example, the impacts of smaller surface waves superimposed on resolved virtual swell. Such an approach could likewise be modified to provide momentum augmentation in cases where waves moving relative to the flow aloft can increase the momentum of the flow field.

In addition to momentum-based approaches, immersed boundary methods could also be used to characterize the marine boundary interface and its changes over time and space using a more exact implementation than methods based on momentum, while also permitting arbitrary slopes without leading to numerical errors in models that use terrain-following vertical coordinates. As with the virtual building approach, canopy methods could likewise be combined with immersed boundary methods to add fidelity.

Exploration of these previously described methods will be undertaken by the team to provide improved sea-surface effect parameterization, addressing a range of sea-state applications, model resolutions, and fidelity requirements.

9.0   Uncertainty Quantification

Mesoscale-microscale-coupled simulations are sensitive to the parameterizations used in each of the mesoscale and microscale solvers. In particular, these parameterizations typically include a number of uncertain parameters. Ideally, uncertainties propagating from both the mesoscale and microscale models should be taken into account when attempting to quantify the overall uncertainty in mesoscale-microscale-coupled simulations. However, due to the large number of parameters plus the relatively high computational cost of LES, it is more feasible to employ a tiered strategy to assessing the uncertainty of coupled simulations by first identifying the most critical parameters in each of the mesoscale and LES closures before attempting a combined analysis. Using WRF in a mesoscale configuration, Yang et al. (2017) analyzed the sensitivity of predicted turbine-height wind speeds to 12 parameters of the MYNN planetary boundary-layer scheme and 14 parameters of the MM5 surface-layer scheme. Promisingly, this study found that most of the uncertainty in predicted wind speeds was attributable to just a few of the parameters in each of the boundary- and surface-layer schemes. Here, using nested WRF/WRF-LES simulations, we evaluate the sensitivity of predicted boundary layer winds and turbulence to parameters of a 1.5-order, TKE-based SGS turbulence closure and of a surface flux scheme. We sample a range of parameter values to generate an ensemble of coupled mesoscale-microscale model runs using a nested WRF/WRF-LES computational approach. This set of WRF/WRF-LES model runs is then used to determine which LES closure parameters most strongly influence predictions of hub-height winds.

9.1   Case Selection and Set Up

We simulate a period on Aug. 21, 2016, during the WFIP 2 in the Columbia Basin region of Washington and Oregon (Shaw et al. 2019). This period has also been simulated and compared to lidar observations using a proper orthogonal decomposition technique by MMC project team members, as described in Chapter 10.0 of this report. The selection criteria that were applied to identify this case are described in Section 3.2. This analysis indicates that nested WRF/WRF-LES simulations can generate coherent turbulent structures that are generally consistent with the observed structures.

Simulations are run with three levels of nested domains. The outermost domain has a horizontal grid spacing of 1.35 km and uses a typical suite of physical parameterizations appropriate to mesoscale resolutions. Initial and boundary conditions of this domain are generated from the GFS reanalysis. We also evaluated the National Centers for Environmental Prediction's NARR for this purpose but did not find consistent improvement in the agreement between observed and simulated wind speeds. The two inner domains have horizontal grid spacings of 150 m and 50 m, respectively, and both are treated as LES. The outermost domain is spun up for 6 hours before initiating the inner domains, then all three domains are run for an additional 3 hours, spanning 18:00-21:00 UTC. This mid-day period, which is characterized by strong positive surface heat fluxes, experiences convective conditions.

The simulation domains are positioned so that all three encompass two key measurement locations from the WFIP 2 campaign. Sodar, lidar, and radar wind observations were obtained at the Wasco State Airport in Oregon, whereas sonic anemometer measurements of wind and temperature at 50-m and 80-m levels were collected at the nearby Physics site-12 (PS-12).

9.2   Determination of Parameter Ranges

Although a few SGS turbulence closures are available in WRF-LES, we focus on the 1.5 order TKE-based closure that largely follows the model presented by Deardorff (1980), as similar types of closures are implemented in many microscale atmospheric models, including Nalu-Wind. For clarity of the following discussion, we present some key equations of this closure.

In particular, eddy viscosity, K_m, is determined (at each grid point) from the SGS TKE e and an eddy length scale as $K_m = c_k e^{1/2}$. The eddy length scale equals the grid-based filter scale, Δ, when (grid-scale) stratification is neutral or unstable and is reduced under stable stratification according to $c_n = e^{1/2} N^{-1/2}$, where N is the Brunt-Väisälä frequency. The ratio $l\Delta^{-1}$ is used in the closure as a measure of the local level of flow stability.

The SGS TKE itself is determined by solving a prognostic equation that includes terms for resolved and SGS transport, production of TKE by resolved shear, production/destruction of TKE through buoyancy, and dissipation, ϵ. The closure for dissipation is $\epsilon = c_\epsilon e^{3/2} l^{-1}$ and the coefficient, c_ϵ, is modified in response to local stability according to $c_\epsilon = (c_{\epsilon N} - c_{\epsilon S})l\Delta^{-1} + c_{\epsilon S,}$ where subscripts N and S refer to neutral and stable stratification. The coefficient, $c_{\epsilon S}$, is difficult to directly constrain through physical arguments. However, the coefficients of the closure can be related to a critical Richardson number, Ri_c (de Roode et al. 2017), then $c_{\epsilon S}$ can be determined.

The SGS TKE closure interacts with the surface layer scheme in several ways, most notably through setting the near-surface value of e. Therefore, we also consider the effect of varying the surface roughness. This is accomplished by enhancing the default roughness length by a multiplicative factor, $z_{f,}$ ranging between 1 and 2, following Yang et al. (2017). We frame our analysis in terms of the logarithm of z_f to be more consistent with how this factor is used within the surface scheme.

Modifications to the WRF source code were required to explicitly define and expose all parameters (except c_k) as options in the namelist input file. This code is available at https://github.com/cmkaul/WRF/tree/les_uq and is a fork of the A2e-mmc version of WRF. The parameters tested, their uncertainty ranges, and their default values in WRF are summarized in Table 9.1.

Table 9.1. Parameters varied in the uncertainty analysis. Symbols are defined in the text. The uncertainty quantification (UQ) range is the range of values input to the Latin Hypercube sampling algorithm. The WRF default is the default version used in WRF v4.1.2. Note that in the standard WRF release, only c_k is available as a namelist option. The other parameters are not explicitly defined, but rather implicitly fixed within the code base.

Parameter	UQ Range	WRF Default
c_k	0.08–0.3	0.15
c_n	0.5–0.82	0.76
$c_{\epsilon N}$	0.8–1.5	0.93
Ri_c	0.1–1	0.23313
z_f	1–2	1

9.3   Simulation Ensemble

We generate an ensemble of 64 nested WRF/WRF-LES simulations. This number of simulations is needed to adequately sample across the uncertainty ranges of the five parameters identified for our analysis, provided the sample values are selected through an efficient technique. Here, we employ a Latin hypercube sampling algorithm (Stein 1987; Helton and Davis 2003).

All ensemble runs use an identical configuration of the outermost mesoscale domain and each uses the same set of LES parameter values in the 150-m and 50-m domains. Thus, uncertainty quantification analysis can be performed using output from either domain. In particular, scale dependence of the parameter sensitivity can also be investigated. Our initial analysis focuses on the 10-minute average wind speed and its variance.

Time series of these quantities at the PS-12 location are shown in Figure 9.1. For both simulations and observations, we compute means and variances of 1-Hz instantaneous wind speed values over 10-minute windows. Simulated wind speeds are biased low relative to the observed wind speeds. The one standard deviation range of 10-minute averaged simulated wind speeds is narrow; however, the variance of the 1-Hz simulated wind speeds is large, which is consistent with the observations. Simulated wind speeds were also found to be biased low at the Wasco State Airport location.
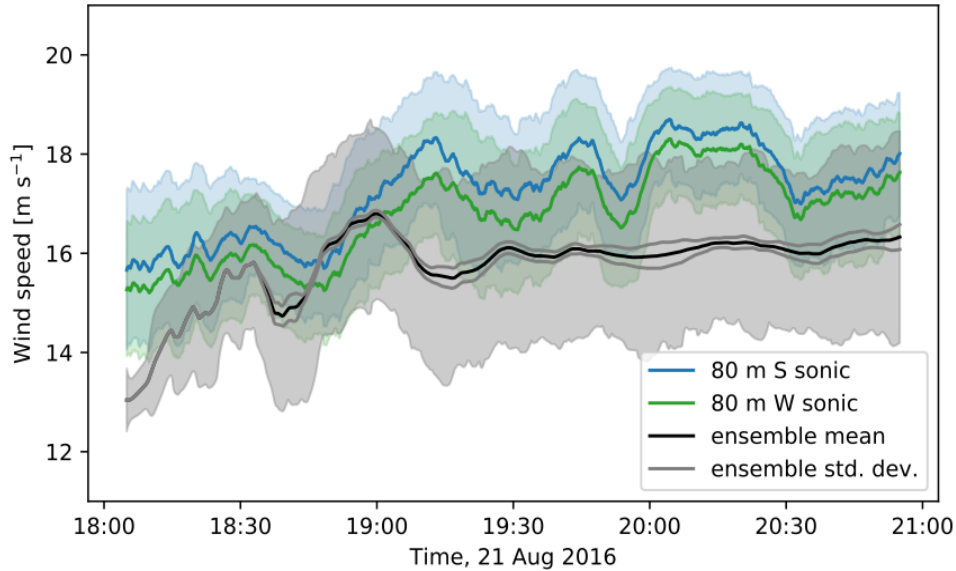
Figure 9.1. 80-m wind speed at PS-12 from WRF simulations and observations. Data from south and west sonics are shown in blue and green, respectively; solid lines indicate the 10-minute average wind speeds, and shading indicates their one standard deviation range. The solid black line shows the mean 10-minute average wind speed of the simulation ensemble at 150-m resolution, gray lines indicate the one standard deviation range of the ensemble, and gray shading shows the one standard deviation spread about the ensemble mean considering the maximum wind speed variance of any of the ensemble members.

9.4 Parameter Importance Ranking

Valuable information can be gained by ranking the relative importance of the five tested parameters in determining the ensemble spread. For example, any parameters that show a low level of importance could be excluded in future analyses, whereas parameters with a high level of importance can be targeted for performing model calibration. While there are a number of possible approaches to performing importance ranking, here we use two approaches.

The first approach, which is very similar to the methodology used by Yang et al. (2017), is based on a generalized linear model (GLM). This approach is best suited to identify the parameters that have strong linear effects on the model output.

The second approach is based on regression with random forests (RF). A description of the method can be found in Genuer et al. (2010), and the implementation in the R environment is discussed by Liaw and Wiener (2002). In contrast to the GLM approach, the RF approach is better suited to identify parameters that affect the model output nonlinearly.

Briefly, the method begins with the construction of a set of learning data with vectors of explanatory variables, X_i (here, the values of c_k, c_n, $c_{\epsilon N}$, Ri_c, and z_f) and vectors of responses, Y_i. In our study, these Y_i are WRF-LES predictions of 10-minute running means and variances of wind speed at 50-m and 80-m vertical levels. Specifically, we analyze the values obtained at 10-minute intervals between 19:20 UTC and 20:50 UTC, at the PS-12 and Wasco State Airport

locations, and consider both the 150-m ("d02") and 50-m ("d03") resolution domains. The index i runs from 1 to 64, to account for all 64 ensemble members.

The method proceeds by growing regression trees to describe the learning data. A procedure called permutation importance ranking (Genuer et al. 2010) can then be used to determine the relative importance of the explanatory variables. Parameter sensitivity scores can be computed with respect to each of the response variables, Y_i (again, these are means and variances of wind speed in our analysis), then summed across the response variables. The results of this analysis are shown in Figure 9.2. Each of the bar plots shows the result of one of the analysis methods ("GLM" or "RF") for a given location ("PS-12" or "Wasco"), computational domain ("d02" or "d03"), and vertical level ("50 m" or "80 m"). Several interesting features emerge from Figure 9.2. First, the results do not show a strong dependence on vertical level, at least over this narrow range. Second, the GLM and RF analysis methods yield different results, indicating the significance of nonlinear interactions among the parameters. With the details depending on the analysis method used, we also note differences between the parameter rankings on the coarser and finer grids.
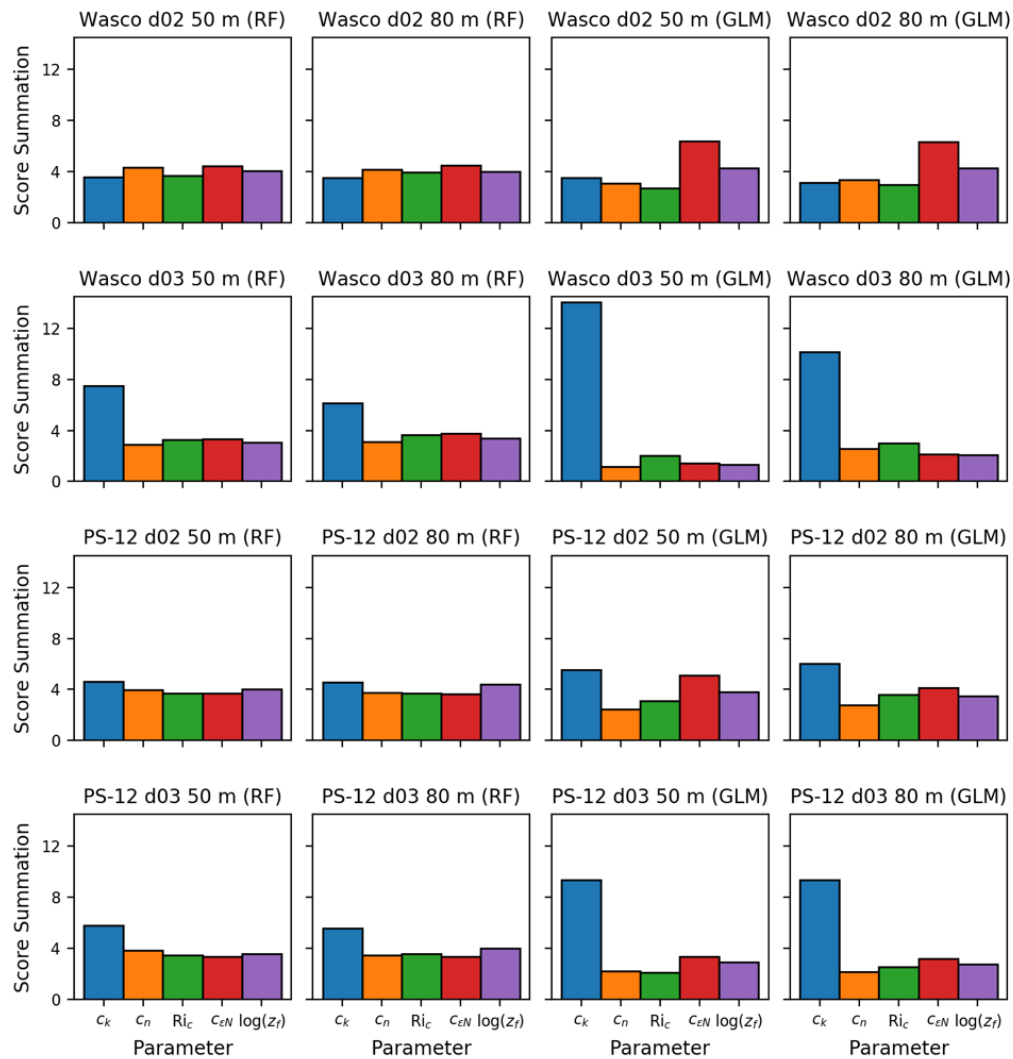
Figure 9.2.   Comparison of the aggregated sensitivity scores for each parameter.

Using the RF method, all parameters show nearly equal importance for the coarser grid predictions of both means and variances at the two sites. Differences in the sensitivity scores are certainly too small to allow any of the parameters to be excluded from future analysis. However, a slightly different pattern emerges on the finer grid. Here, the RF method more clearly identifies c_k as the most important parameter, while sensitivity to the remaining parameters is about equal.

The GLM method identifies $c_{\epsilon N}$ as the most important parameter at the Wasco site for the coarse domain simulation, and c_k followed by $c_{\epsilon N}$ at the PS-12 site. However, there are no obviously excludable parameters. On the finer grid, c_k strongly predominates as the most important variable at both locations when the GLM method is used. Considering the roles each of the parameters plays in the model, it is reasonable that c_k receives larger sensitivity scores under the GLM method that identifies linear effects as it directly multiplies local gradients to determine the subgrid-scale fluxes of momentum and scalar quantities.

It should be recalled that the coarser resolution domain provides the lateral boundary conditions for the higher resolution domain (i.e., here d02 provides the boundary conditions to d03). Thus, it is interesting that the parameter sensitivity scores differ as much as they do between the domains with 150-m and 50-m horizontal grid spacing. Since 150-m resolution is a relatively coarse resolution for LES, even LES of convective ABLs, it is not entirely surprising that the parameter importance shows resolution dependence. However, it needs to be assessed whether the parameter importance tends to stabilize over the more typical range of resolutions at which LES is performed (i.e., horizontal grid spacing spanning roughly 10 m to 100 m).

9.5 Summary and Next Steps

Our results indicate that all five of the parameters we considered influence predictions of hub-height winds. While the eddy viscosity coefficient, c_k, seems to be the single most important parameter for this case, all remaining parameters remain influential when we use a random forest analysis approach that can capture nonlinear interactions between variables. While these results do not support excluding any parameters from subsequent UQ analyses, we note that the number of parameters remains relatively tractable.

The preceding results raise a few outstanding questions. First, how generalizable are these findings? Here, we analyzed a single case study of a convective boundary layer. Although the computational cost of generating the simulation ensemble precludes consideration of a large number of cases, it is important to examine other scenarios. In particular, we plan to evaluate at least one more convective period observed during WFIP 2 as, intuitively, the parameter sensitivities found for that case should be similar to those documented here. As already mentioned, we would also like to further examine resolution sensitivity of the parameter rankings.

Second, what additional output variables should be considered? Higher-order statistics, such as turbulent momentum fluxes, are relevant to issues such as wake recovery into which LES can provide important insights.

It is interesting to note that, even under the convective conditions simulated here, the results are sensitive to parameters that are used only in the presence of local stable stratification. We plan to investigate this finding more closely to better understand the cause(s) for this dependence. The TKE-based SGS model implemented in the Nalu-Wind model is simpler than that in WRF and does not include explicit stratification dependence. In other words, of the five parameters

we examine here, only c_k and z_f are relevant for Nalu-Wind's current formulation. Based on these results, we would like to assess the potential consequences of using this simplified closure form. Ongoing with our UQ analyses using WRF, we are participating in verification tests of Nalu-Wind's predictions of atmospheric boundary layers, which is important preparation for performing uncertainty quantification studies of coupled WRF/Nalu-Wind simulations.

10.0 Lidar Simulator

In our previous work (Rai et al. 2019), LES horizontal wind velocity contours near the surface showed streak-like structures orienting along the mean wind direction. For instance, Figure 10.1 (left) for the u-component of velocity 90 m above the surface shows such elongated structures occupying the entire area and orienting west to east. This flow field was generated using WRF-LES with 30-m grid spacing during daytime with moderate heat flux and winds. These structures play a significant role in transferring the heat and momentum over space and time. However, it is difficult to validate their existence in a real atmosphere using traditional measuring instruments, such as anemometers. The scanning lidar can provide data at more spatial locations. Therefore, this work uses lidar scanning data collected during the WFIP 2 campaign at Wasco State Airport, Oregon, to observe the turbulence structures and evaluate the flow field from the simulation. Figure 10.1 (right) shows the location and the scope of plan position indicator (PPI) scanning for the lidar. PPI scanning at three elevation angles (2.4, 4, and 6 degree) has been used. The scanned grid points shown here only cover the east-sector data for which the flow is approximately westerly, and the radial velocity would provide truer magnitude of u-component of velocity. The spatial resolution along the line of sight (LOS) is 100 m, and the LOS moves $1°$ azimuthal angle in each second for 25 seconds. Here, only 19 radial locations are considered as the quality of data worsens for larger radial distance from the lidar.
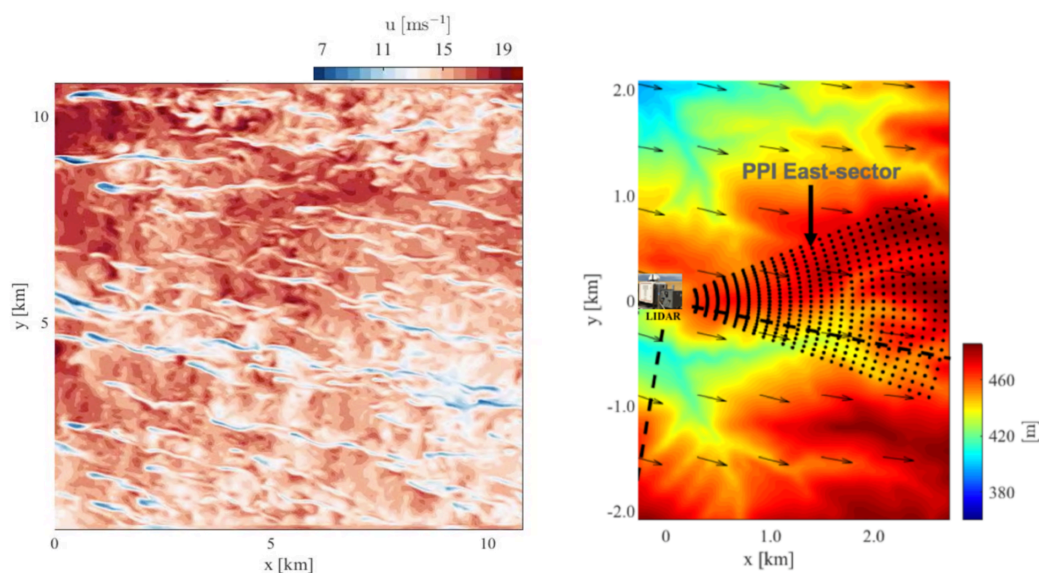
Figure 10.1. u-component of wind velocity 90 m above the surface (left); location of scanning lidar and east-sector area for analyzing lidar data on the top of elevation contour (right).

To evaluate the streak-like structures seen in the simulated flow, we prepared simulated lidar data (east-sector) using a highly resolved wind field from LES (30-m grid spacing) by interpolating the simulated data into the corresponding grid locations of the lidar. The data were interpolated each second to match the corresponding scanning rate of the lidar. Then, the east-sector data from our simulated lidar were compared against the east-sector data from the Wasco scanning lidar. The wind data consist of a 2-hour period (i.e., total data length) with

unstable conditions that were simulated for August 21, 2016, using three nested domains in the WRF model. The east-sector PPI data that were scanned at two elevation angles—2.4 and 4 degree—were added together to increase the number of east-sector data (i.e., 16 east sectors). Fluctuating velocities about the mean for both measured and simulated lidar data were calculated using the east-sector data (Figure 10.2). The instantaneous velocity from both the scanning lidar data and simulated data exhibits similar magnitude of the fluctuating radial velocity. The flow structures in both cases are oriented west to east along the mean wind direction. Qualitatively, the radial velocity contours show that the simulation for this date is able to capture the flow features of the lower atmospheric boundary layer.
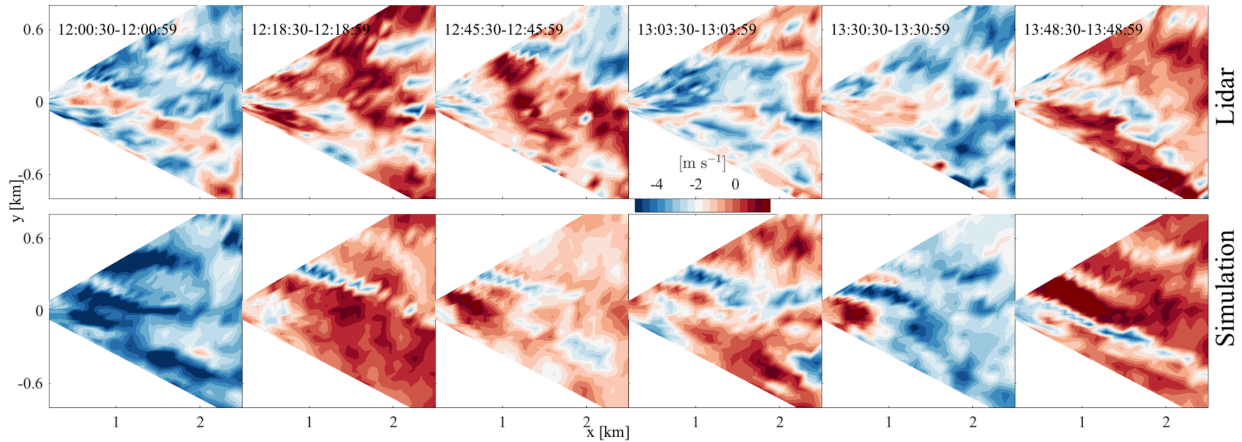
Figure 10.2. Fluctuating radial velocity about its mean, derived from a 2-hour unstable period for the scanning lidar data (top) and simulated data (bottom).

Proper orthogonal decomposition (POD) analysis of the flow field containing coherent structures can segregate the energetic structures of the flow into the first few POD modes and, hence, they can be used to reveal the amount of turbulent structures present in the different mode numbers. The POD decomposes the flow field into basis functions (i.e., POD spatial mode) and its coefficients. Figure 10.3 shows the first six spatial POD modes obtained using the fluctuating velocities of east-sector data described above for the 2-hour period. The first spatial POD mode for both simulated and observed cases shows positive magnitude in the entire sector area, suggesting that the first POD mode represents the largest amount of energy and size of turbulent structures. As the POD mode number increases, the magnitude of POD modes starts to fluctuate about zero mean, and the size of the spatial structures decreases. The energy contained in these higher POD mode structures are smaller compared to that of the lower POD mode structures. Moreover, the orientation of the flow structures in both simulated and measured cases are similar, mostly orienting along the mean wind. However, the POD energy (not shown here) for most of the modes of the simulated case shows little mismatch with that of the observed case, except for the second and third modes.
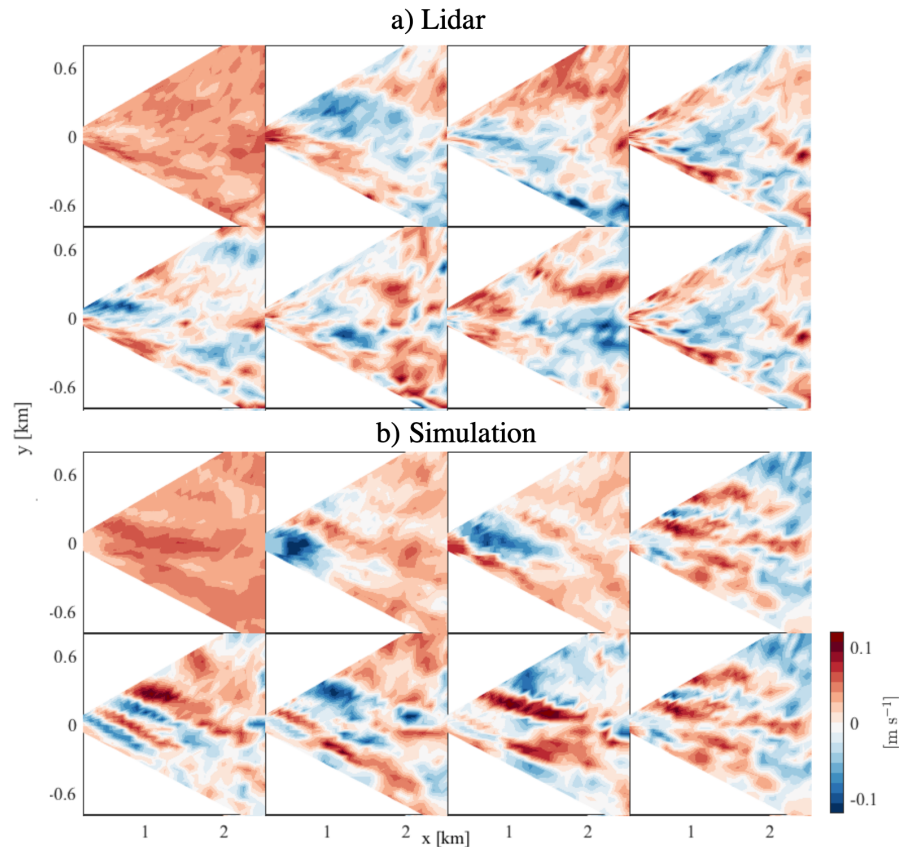
Figure 10.3. Spatial POD modes derived from fluctuating radial velocity from a) scanning lidar data and b) simulated data.

The results for the POD analysis discussed above were derived from the scanning lidar data from a single day and from 2 hours of simulated data (that provide 16 east sectors). The POD results derived from these few east-sector data may not well represent the unstable case due to the lack of convergence of the second-order statistical moment. To make the east-sector ensemble data, we have used all 36 days of data for the POD analysis that allows more than 500 east-sector snapshots for each case. As the mean and variance of radial velocity of east-sector data vary with time, each east-sector scan was binned according to the range of mean and variance values (i.e., <5 m/s, 5-10 m/s, and >10 m/s for mean and <1.5 m^2/s^2 and >3 m^2/s^2 for variance of the radial velocity). The spatial POD modes and energy were computed using the east-sector data for the period of 2000-2300 UST, representing daytime unstable conditions. Note that these modes are derived from using more than 500 east-sector data (from 36 days), different from that depicted in Figure 10.2 and Figure 10.3, which resulted from a single day of data (i.e., 16 east sectors). Figure 10.4 shows four representative spatial POD modes (1st [top row], 4th [second row], 10th [third row], and 19th [bottom row]) for various groups of mean and variance of the east-sector data. The POD modes help to evaluate the type and size of flow structures for each different POD mode number. The results show that the POD modes for the smaller mode number for all five cases exhibit large and similar spatial structures. However, the size of the spatial structures decreases as POD mode number increases, irrespective to the type of case. The large structures in the lower mode numbers indicate that most of the energy of the flow is distributed over the first few modes. Although the size of the turbulent structures decreases with an increase of mode number in all cases, the shape of the structures differs

between them. Cellular-like structures dominate for the small mean and variance, whereas the more streak-like structures become more common for the large mean and variance of the radial velocity. This indicates that the different size of structures resulted from varying wind conditions and contributes to energy exchange, which varies in magnitude and rate of energy transfer over space and time.
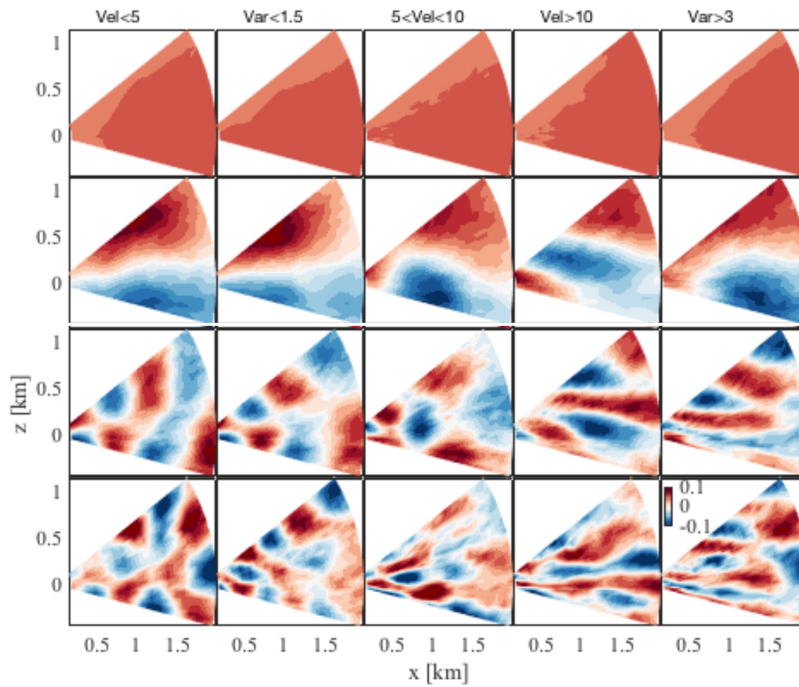
Figure 10.4. Spatial POD modes derived from scanning lidar data using mean—less than 5 m/s (579 east sectors), 5-10 m/s (598 east sectors) and greater than 10 m/s (619 east sectors), and variance – less than 1.5 m^2/s^2 (799 east sectors) and greater than 3 m^2/s^2 (333 east sectors) of the radial velocity (shown in columns) for the 1st mode (top row), 4th mode (second row), 10th mode (third row), and 19th mode (last row).

11.0 Evaluation of Nalu-Wind as a Microscale Solver

11.1 Introduction

Evaluation of candidate mesoscale and microscale solvers was an early activity of the MMC project team. Results of the microscale solver evaluation were published in Mirocha et al. (2018) (hereafter, M18) and feature a comparison of simulations of idealized neutral and convective boundary layers using WRF-LES (Skamarock et al. 2008), SOWFA (Churchfield et al. 2012), and HiGrad (Sauer et al. 2016). Since this study was conducted, Nalu-Wind has been developed as a microscale solver with advanced capabilities for wind farm simulation. Thus, the major objective of the work presented in this chapter was to understand the performance of Nalu-Wind in simulating relatively simply configured atmospheric boundary layers in the context of the earlier analysis performed by the team, preparatory to using Nalu-Wind to perform more complex, coupled simulations. We focus on predictions of the mean wind speed and variance of the 10-minute averaged wind speed and do not replicate the analysis of turbulent fluxes and spectra performed in M18. As the following discussion will illustrate, even a quantity as simple as the mean wind speed shows sensitivity between (and within) models that is difficult to fully explain.

11.2 Approach

This section reviews key aspects of the formulation of Nalu-Wind, describes the simulation setups, and outlines the suite of sensitivity tests.

11.2.1 Nalu-Wind Formulation

Nalu-Wind is a generalized unstructured solver for the Boussinesq equations of atmospheric motion. Like its parent code, NaluCFD/Nalu (Domino 2015), it employs a finite-volume discretization approach but includes a number of enhancements targeted to wind energy applications. Documentation of Nalu-Wind may be found at https://nalu-wind.readthedocs.io/en/latest/index.html.

Nalu-Wind offers two options for spatial discretization: a control volume finite element method (CVFEM) and an edge-based vertex-centered (EBVC) scheme that is similar to the discretization approach used by OpenFOAM and, by extension, SOWFA. Broadly speaking, the EBVC scheme offers good accuracy at lower computational cost for highly structured meshes while the CVFEM scheme is recommended for lower-quality meshes. The EBVC scheme is used here, unless specifically noted.

Advection stabilization is implemented as a blend between generalized central and higher-order upwind interpolation/extrapolation operators for the advected quantities, including the three velocity components, potential temperature, and SGS TKE. The blending function depends on the cell Peclet number. Most of the simulations presented here choose parameters of the blending function such that velocity interpolation uses central operators and interpolations of other variables are upwinded.

An implicit, second-order backward difference formula (BDF2) scheme is used for time integration, and all simulations use a 1-s time step unless stated otherwise.

Nalu-Wind has a few options for SGS turbulence closure. Most of the simulations performed here use Nalu-Wind's 1.5 order, SGS TKE scheme, but the Smagorinsky scheme is also used as a sensitivity test. Details of these schemes, and other aspects of Nalu-Wind's formulation, are provided in the code documentation.

11.2.2 Simulation Setup

M18 discuss the design of the simulations. In brief, neutral and convective scenarios were defined based on observations from a 200-m meteorological tower located at TTU's National Wind Institute near the SWiFT test facility.

Initial velocity profiles were set equal to the geostrophic velocity components. For the neutral case, the geostrophic velocity components are (u_g, v_g) = (-2.223 m s^{-1}, 6.108 m s^{-1}), yielding a geostrophic wind speed, U_g = 6.5 m s^{-1}. The potential temperature profile is initialized as θ= 300 K below 1 km and increases at a rate of 10 K km^{-1} above 1 km. The domain size is 2.4 km in each horizontal dimension with a 2-km vertical extent. A Rayleigh damping layer is applied above 1,600 m.

The convective case has (u_g, v_g) = (9 m s^{-1}, 0 m s^{-1}). The mean potential temperature equals 309 K below 600 m and increases at a rate of 4 K km^{-1} above 600 m. The surface potential temperature flux is H_S=0.35 K m s^{-1}. The domain size is 6 km by 3 km with a damping layer above 2,400 m.

Both cases use a surface roughness length of 0.05 m and calculate Coriolis forcing with respect to a latitude of 33.5°.

11.2.3 Sensitivity tests

For each of the neutral and convective cases, we define a "baseline" case that uses the initial conditions and surface forcing described in Section 11.2.2 and the following options in Nalu-Wind: EBVC discretization, TKE-based SGS scheme, and advection stabilization described in Section 11.2.1. We also perform sensitivity tests. In one set of these tests, aspects of the physical forcing are perturbed. In the second set of tests, we test different model configuration options: use of the CVFEM scheme, use of the Smagorinsky SGS scheme, and centered interpolations in the advection scheme.

Additionally, we look at sensitivity to the grid aspect ratio (AR), using the same choices as tested by M18. Here we hold the grid filter scale approximately constant while varying the ratio of horizontal and vertical resolutions.

The suite of neutral simulations is summarized in Table 11.1 and convective simulations are described in Table 11.2. The simulation naming convention uses four attributes of the simulations, as follows: simulations using the "baseline" options begin with "N" for Nalu-Wind; other simulations are named by the modified option. The second part of the name indicates the neutral or convective case ("N" or "C"). The first number indicates the forcing, "1" for the standard forcing and "2" or "3" for forcing perturbations. The second number is the grid AR.

Table 11.1. Neutral case simulations.

Run name	Δx (m)	Δz (m)	U_g (m s^{-1})	z_0 (m)	Comment
N-N-1-3.3	25	7.5	6.5	0.05	Baseline options
N-N-1-1	15	15	6.5	0.05	Baseline options
N-N-2-3.3	25	7.5	7.15	0.1	Forcing sensitivity
N-N-2-1	15	15	7.15	0.1	Forcing sensitivity
N-N-3-3.3	25	7.5	5.85	0.01	Forcing sensitivity
N-N-3-3.3	15	155	5.85	0.01	Forcing Sensitivity
CVFEM-N-1-3.3	25	7.5	6.5	0.05	uses CVFEM scheme
CVFEM-N-1-1	15	15	6.5	0.05	uses CVFEM scheme
CentAd-N-1-3.3	25	7.5	6.5	0.05	central advection interpolation
CentAd-N-1-1	15	15	6.5	0.05	central advection interpolation
Smag-N-1-3.3	25	7.5	6.5	0.05	uses Smagorinsky SGS closure
Smag-N-1-1	15	15	6.5	0.05	uses Smagorinsky SGS closure

Table 11.2. Convective case simulations

Run name	Δx (m)	Δz (m)	U_g (m s^{-1})	H_s (K m s^{-1})	Comment
N-C-1-3	30	10	9.0	0.3500	Baseline options
N-C-1-1	20	20	9.0	0.3500	Baseline options
N-C-2-3	30	10	10.0	0.4364	Forcing sensitivity
N-C-2-1	20	20	10.0	0.4364	Forcing sensitivity
CVFEM-C-1-3	30	10	9.0	0.3500	uses CVFEM scheme
CVFEM-C-1-1	20	20	9.0	0.3500	uses CVFEM scheme
CentAd-C-1-3	30	10	9.0	0.3500	central advection interpolation
CentAd-C-1-1	20	20	9.0	0.3500	central advection interpolation
Smag-C-1-3	30	10	9.0	0.3500	uses Smagorinsky SGS closure
Smag-C-1-1	20	20	9.0	0.3500	uses Smagorinsky SGS closure

11.3 Results

Following M18, we evaluate the results of our simulation using 1-Hz time series of vertical profiles extracted from one location within the periodic simulation domain. The simulation data are compared to observations from the TTU tower for August 17, 2012 (neutral case) and July 4, 2012 (convective case). WRF, SOWFA, HiGrad, and observational data were obtained from the A2e's Data Archive and Portal; digital object identifiers of the specific data sets are provided in M18.

The neutral case simulations are analyzed over a 2-hour window between hours 14 and 16 of the simulation. The convective case simulations also use a 2-hour window, between hours 1 and 3 of the simulation, taking advantage of the more rapid spin-up of this case.

11.3.1   Neutral Case

Instantaneous contour plots of the wind speed in the baseline, AR=3.3 simulation, are shown in Figure 11.1 and depict elongated flow structures aligned with the mean flow direction. The vertical extent of the turbulence is strongly limited by the imposed temperature inversion.

| (a) | (b) |

Figure 11.1. Snapshots at 14 hours simulated time of baseline neutral case with AR = 3.3 (N-N-1-3.3). The horizontal wind speed is shown (a) on a horizontal plane at a height of 100 m; (b) on an east-west plane through the center of the domain.

The mean wind speed, U, normalized by the friction velocity, u_*, is plotted in Figure 11.2. The WRF, SOWFA, and HiGrad results correspond, respectively, to the W1, S1, and H1 simulations defined by M18. These particular simulations are selected for comparison as they are most similar to the baseline Nalu-Wind simulations in terms of the grid geometry, forcing, and SGS modeling approach. All models tend to predict a faster increase of wind speed with height than the theoretical, logarithmic rate. Comparison of the N-N-1.3.3 and N-N-1-1 results shows the sensitivity of the results to the numerical grid, with the "overshoot" problem described by Brasseur and Wei (2010) being worsened at higher AR, as expected. In the version of Nalu-Wind tested here, the height above the surface is taken as one-quarter of the length of the nearest edge that intersects the boundary face. In newer versions of Nalu-Wind, the user will be able to specify the height at which to evaluate the similarity functions.
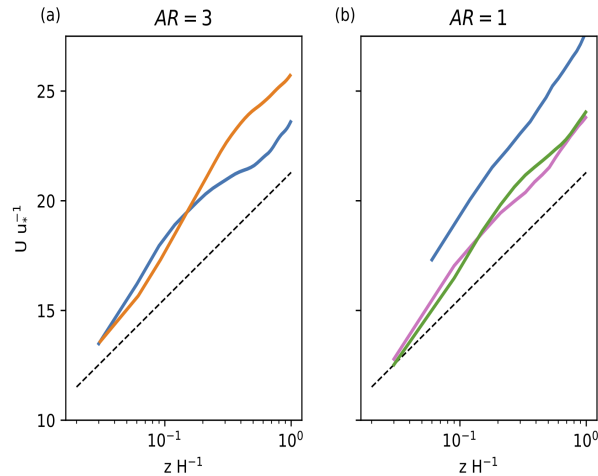
Figure 11.2. Comparison of mean wind speed, U, scaled by the surface friction velocity, u_*, to the theoretical log-law scaling with $\kappa = 0.4$ (black dashed line) for each model. $H = 250$ m and roughness height $z_0 = 0.05$ m. The left panel shows results for AR = 3.3 for Nalu-Wind (N-N-1-3.3, blue) and WRF (W1, orange). The right panel shows results for AR = 1 for Nalu-Wind (N-N-1-1, blue), SOWFA (S1, pink), and HiGrad (H1, green).

Figure 11.3 compares means of the 10-minute-averaged wind speed, U_{10min}, over the 2-hour analysis window (with the running averages assigned to the right edges of each 10-minute window.) Bars or shading show the one standard deviation range of U_{10min} around the overall mean. The models, particularly Nalu-Wind and SOWFA, show lower variance than the observations. This may be due to the fixed (rather than more realistically fluctuating) forcing, limited simulation domain size, and/or to tower wake errors in the observations (M18). To compute this variance, we use only the LES-resolved velocity and do not attempt to include SGS variability. However, this should not significantly affect the comparison with the observations at a 10-minute time scale: using the mean velocity and LES grid spacing, we can estimate the effective temporal filter scale of the simulations as being of the order of only a few seconds.

Figure 11.3. Wind speeds in the baseline neutral case for (a) Nalu-Wind (N-N-1-3.3, blue) and WRF (W1, orange); and (b) Nalu-Wind (N-N-1-1; blue), SOWFA (S1, pink), and HiGrad (H1, green). Averages of U_{10min} are shown as solid lines; their standard deviations are shown by the shaded regions. Means of the observed wind speeds are plotted as dots, whereas the bars show the standard deviations.

To assess sensitivity to forcing, we increase and decrease the surface roughness length, z_0, by a factor of 5, and vary the geostrophic wind by +/- 10% (see Table 11.1). Results are shown in Figure 11.4 and Figure 11.5. The response of the mean wind speed shows the expected trend where greater U_g drives greater U. However, the models vary in their sensitivity. For example, the change in WRF's hub-height wind speed is nearly in one-to-one proportion with the change in U_g, whereas HiGrad shows almost no change (Figure 11.5). Nalu-Wind and SOWFA show similar, intermediate responses. Differences between the models appear to be amplified as U_g is increased.
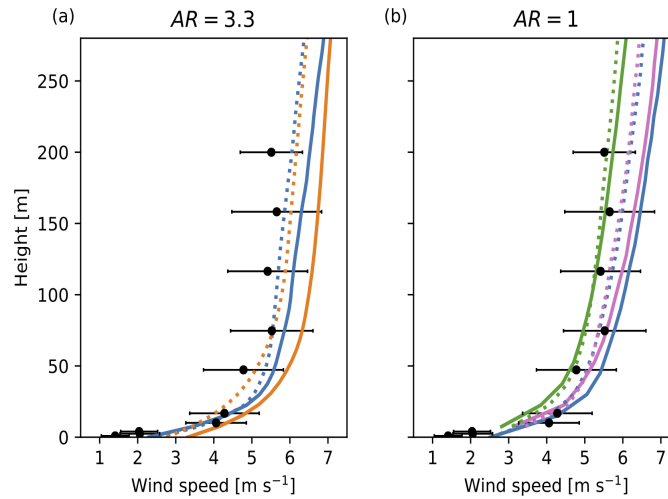
Figure 11.4. Effect of increasing U_g and z_0 on mean wind speed. Results plotted with solid lines have U_g = 1.1$U_{g,0}$, z_0 = 0.1 m (run "2" for each model), while dotted lines show the corresponding baseline case results. Panel (a) shows Nalu-Wind, AR = 3.3 (blue) and WRF (orange). Panel (b) shows Nalu-Wind, AR = 1 (blue), SOWFA (pink), and HiGrad (green). Observations are shown as in Figure 11.3.
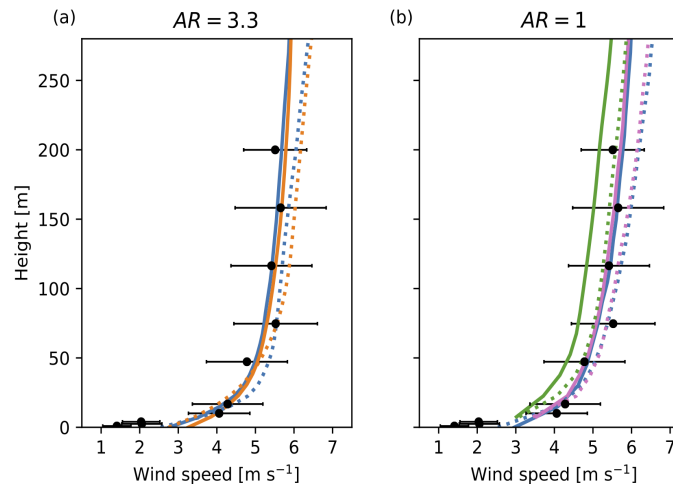
Figure 11.5.   As in Figure 11.4, but for U_g = 0.9$U_{g,0}$, z_0 = 0.01 m (run "3" for each model).

The final set of sensitivity tests for the neutral case looks at sensitivity to choices of numerical and turbulence closure schemes as listed in Table 11.1. Results are shown in Figure 11.6.
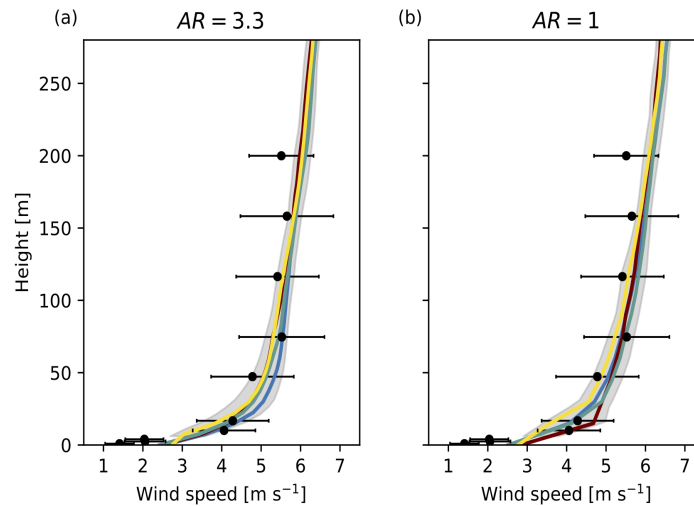
Figure 11.6. Sensitivity of mean wind speed (computed as in Figure 11.3) to solution options in Nalu-Wind. Shown are baseline options (N-N-1-3.3 and N-N-1-1, blue); CVFEM discretization (CVFEM- N-1-3.3 and CVFEM-N-1-1, maroon); central scheme for interpolation of advected scalars (CentAd-N-1-3.3 and CentAd-N-1-1, teal); and Smagorinsky SGS closure (Smag-N-1-3 and Smag-N-1-1, yellow). Gray shading is the maximum +/- one standard deviation range of U_{10min} among all simulations plotted in a panel. Means and variability of observed winds are plotted as in Figure 11.3.

Sensitivity to the model configuration depends on the grid configuration and the specific heights examined. Above about 50 m, the sensitivity is rather weak. The strongest sensitivity is associated with the choice of SGS closure, particularly near the surface. Note this sensitivity could likely be reduced (but probably not eliminated) by adjustments of the SGS closure coefficients.

11.3.2   Convective Case

Snapshots of horizontal wind speed in the convective case are shown in Figure 11.7. In comparison to the neutral case, fluctuations in wind speed are larger and correlated over the boundary layer depth. Quasi-cellular, instead of streaky, flow structures are shown in the plan view (panel a).
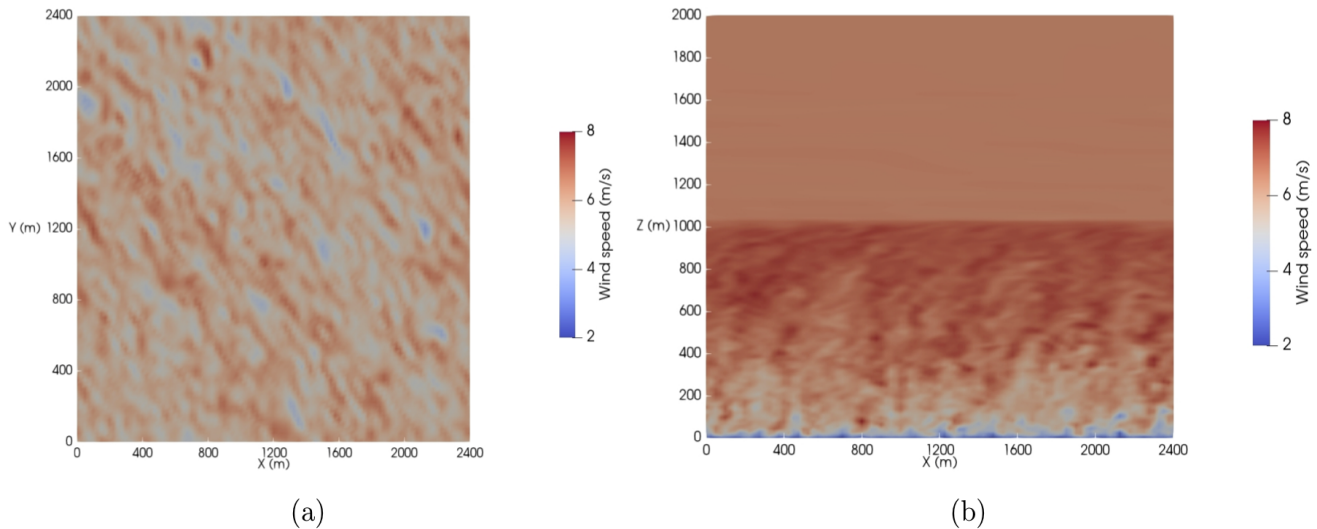
(a)

(b)
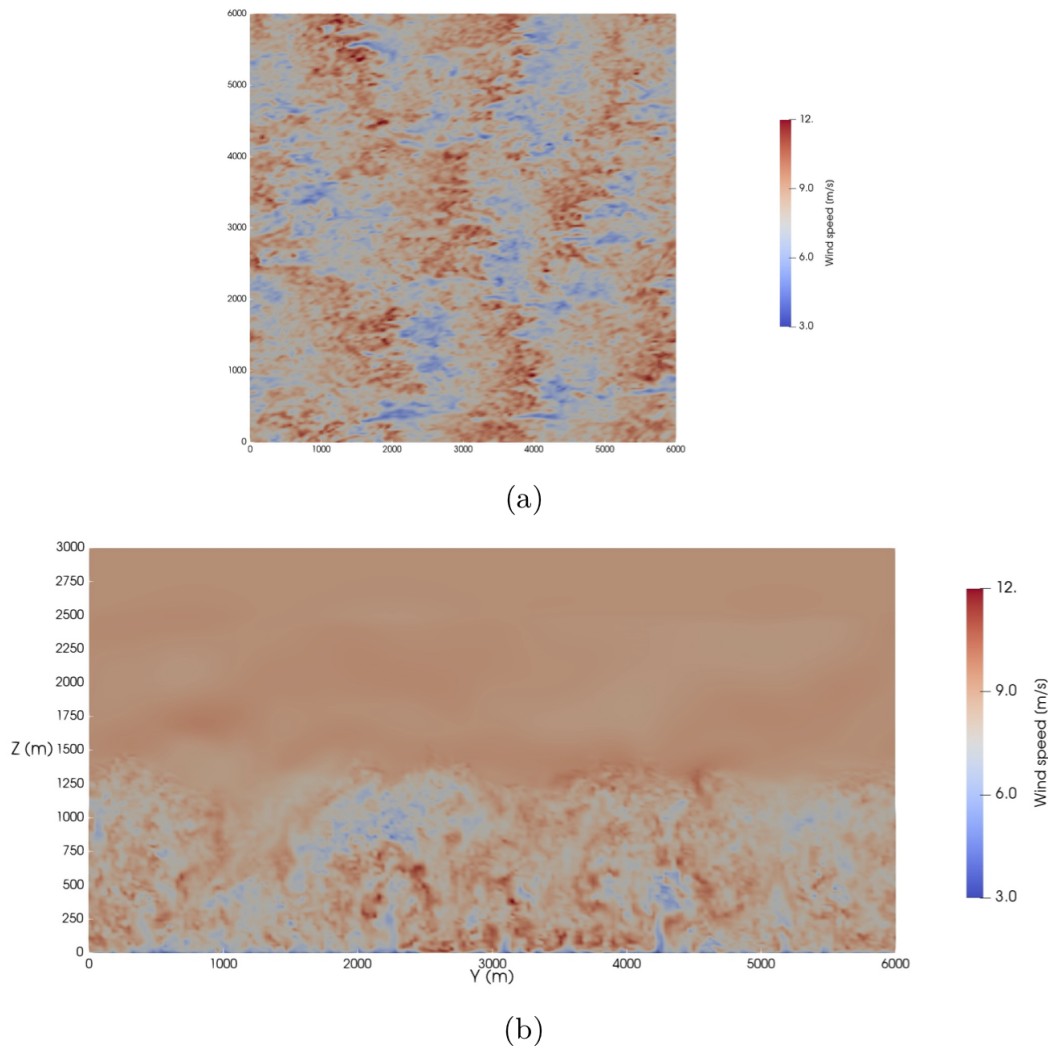
Figure 11.7. Snapshots at 1-hour simulated time of baseline convective case with AR = 3 (N-C-1-3). The horizontal wind speed is shown (a) on a horizontal plane at 100 m; (b) on an east–west plane through the center of the domain (b).

Baseline Nalu-Wind convective simulations are compared to the W1 and H1 convective simulations of M18 in Figure 11.8. Again, differing from the neutral case, the simulated variability of the 10-minute wind speeds is comparable to, or even greater than, the observed variability. Dependence of the mean wind speed to grid cell aspect ratio is small in the Nalu-Wind simulations, suggesting that the important flow structures are well resolved by either combination of horizontal and vertical resolutions.
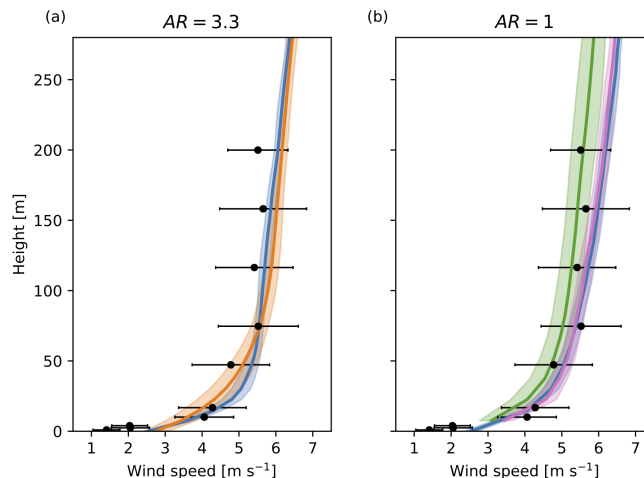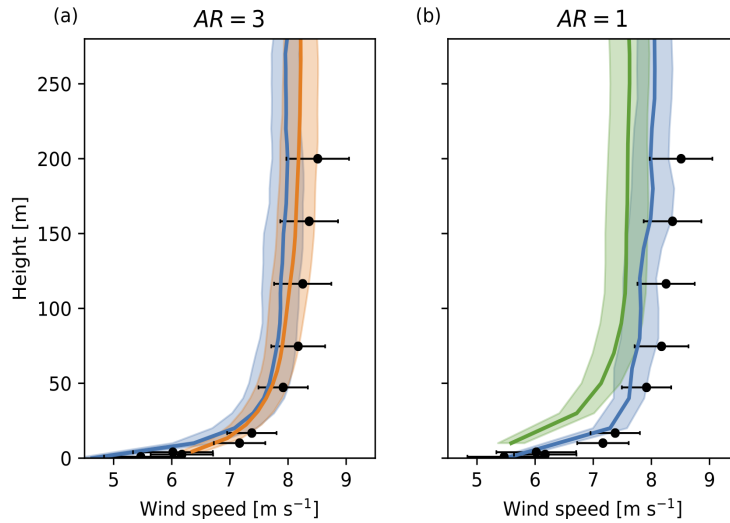
Figure 11.8. Mean wind speeds in the baseline convective case for (a) Nalu-Wind (N-C-1-3, blue) and WRF (W1, orange), and (b) Nalu-Wind (N-C-1-1; blue) and HiGrad (H1, green). The averages of U_{10min} are shown as solid lines; their standard deviations are shown by the shaded regions. Means of the observed wind speeds are plotted as dots, while the bars show the standard deviations.

To look at forcing sensitivity, we increase surface heat flux by 25% and increase U_g by 1 ms^{-1} (see Table 11.2). Figure 11.9 shows results from these simulations. In Figure 11.9(a), both Nalu-Wind and WRF show nearly proportionate change of hub-height wind speed with Ug. The perturbed Nalu-Wind simulation also shows enhanced variability of U_{10min} relative to the baseline.
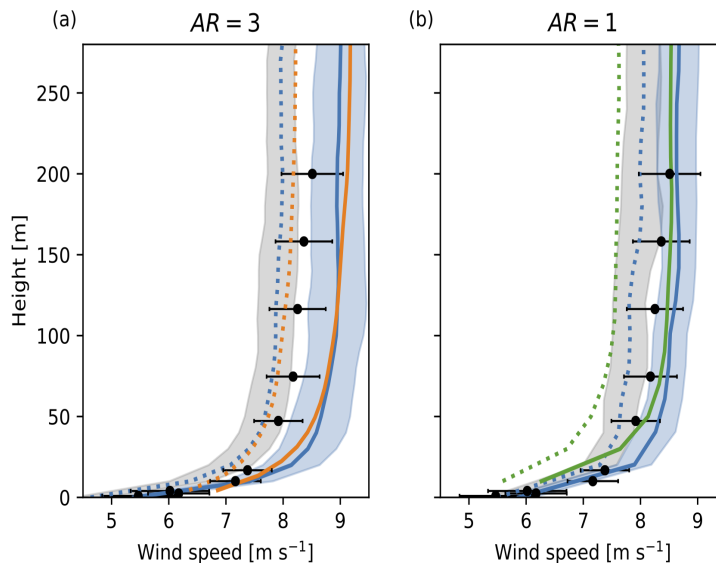
Figure 11.9. Effect of forcing perturbations. Solid lines for $U_g = 10$ m s^{-1}, $H_S = 1.25H_{S,0}$. Dotted lines show the corresponding baseline run. (a) Nalu-Wind, AR = 3 (blue) and WRF (orange), (b) Nalu-Wind, AR = 1 (blue) and HiGrad (green). Observations as in Figure 11.8. Blue and gray shaded areas are ±1 standard deviation ranges of U_{10min} for perturbed and baseline forcings of Nalu-Wind, respectively.

Increases in both the wind speed itself and the variance of the wind speed are much weaker in the AR=1 Nalu-Wind simulations [Figure 11.9(b)], contrary to expected changes in the flow due to higher shear and larger surface heat fluxes. Comparison of resolved TKE in baseline and perturbed simulations also shows a very weak change (not shown).

As for the neutral case, we perform sensitivity tests on model configuration options. These are summarized in Table 11.2 and results are shown in Figure 11.10. For the AR=3 simulations, the largest sensitivity is to use of the Smagorinsky scheme, as was found in the neutral case. However, the results are quite different for the AR=1 simulations. Here, we find a strong response to the use of the CVFEM scheme, which produces a jagged wind speed profile. Recall that these are not instantaneous oscillations but rather time-averaged profiles. The dashed line in Figure 11.10(b) corresponds to another CVFEM sensitivity test simulation performed with a reduced 0.5-s time step. The jaggedness of the profile is not removed, but we do note an apparent time step sensitivity. To examine this further, we carried out additional CVFEM and baseline simulations, as shown in Figure 11.11. When looking at time averages of the virtual tower data (i.e., single location vertical profiles), significant time step/iteration count sensitivity is found for the CVFEM simulations and a smaller time step sensitivity is shown by the baseline configuration simulations. However, when time and spatial averages are both used (exploiting the periodic simulation domain), the time step sensitivity disappears. Note that the anomalous CVFEM wind speed profile persists. Due to this finding, we recomputed the wind speed profiles shown in Figure 11.10 using combined planar and temporal averaging. Key features of the model configuration sensitivity are qualitatively in agreement to the sensitivity shown in the time-averaged-only results, but the quantitative spread in the models is affected.
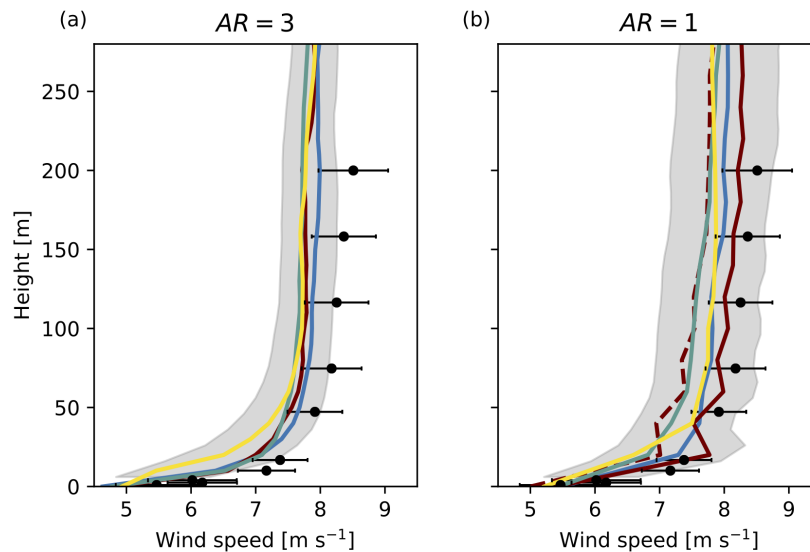
Figure 11.10. Sensitivity of mean wind speed to solution options in Nalu-Wind: baseline options (N-C-1-3 and N-C-1-1, blue); CVFEM discretization (CVFEM-C-1-3 and CVFEM-C-1- 1; maroon); central operators for interpolation of advected scalars (CentAd-C-1-3 and CentAd- C-1-1,teal); and Smagorinsky SGS closure (Smag-C-1-3 and Smag-C-1-1, yellow).
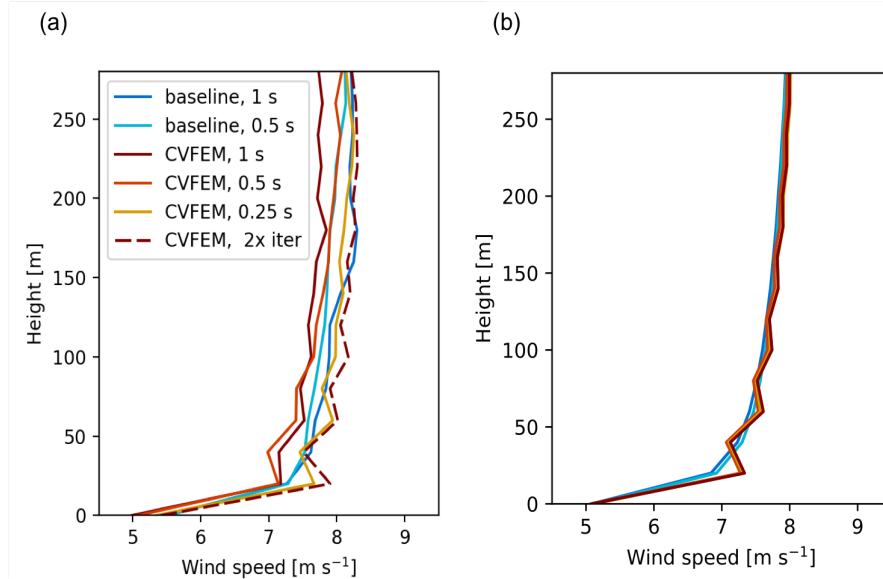
Figure 11.11. Sensitivity of mean wind speed to time step plotted as (a) time average of single point data and (b) time and planar averages over entire periodic flow domain.

11.4 Conclusions

In this work, we revisited the comparison of microscale solvers performed earlier in the MMC project to incorporate Nalu-Wind, a relatively new, highly advanced solver. Simulated winds were compared to observed wind speeds near the SWiFT site in west Texas. Here we focus on the mean wind speed and the variance of the 10-minute averaged wind speed. Detailed analysis of second-moment quantities (turbulent fluxes and turbulent kinetic energy) remains as future work. Discrepancies between models and observations are expected because of the simulations' idealization of the real convective and neutral flow scenarios; however, the differences among the models are difficult to attribute owing to the many differences between the codes in terms of the formulations of their governing equations, numerical schemes, and closures. Nalu-Wind's predictions of mean wind speeds were typically plausible relative to the observations and other models, although there are indications that the implementation of the surface flux scheme and modeling of near-wall turbulence should be improved. Sensitivities of Nalu-Wind to forcing perturbations were generally stronger than sensitivities to various discretization and turbulence modeling options. This strongly argues for the importance of providing realistic forcing to microscale solvers using techniques such as those being developed in the MMC project.

12.0 Synthesis and Summary

The MMC team continues to work together to advance the science and application of coupling mesoscale models to microscale models for the purpose of better simulating wind plants. The team has made major advances in FY19, in planning via a PIRT analysis, setting up a common code development and assessment framework within a team GitHub repository, testing methods to quantify uncertainty, comparing Nalu-Wind to other microscale models, and building a lidar simulator that allows comparison between simulations and 3D lidar scans. In addition, the team has advanced in its core capabilities, planning, and performing rigorous comparisons of coupling techniques and methods to generate turbulence at the microscale. New initiatives to better model surface-layer physics, including applying machine-learning methods, were initiated in FY19. Each of these is summarized briefly below.

12.1 PIRT Analysis

The PIRT is a format to enumerate physical phenomena of importance to an application, such as wind energy, and to rank their importance to the application, our level of physical understanding, and our ability to model those phenomena. The relative levels of phenomena importance and model adequacy lead to a priority score for each phenomena. Such a system enables research groups to prioritize research and development of physics models. The earlier creation of PIRTs for the A2e wind-turbine-wake dynamics and high-fidelity modeling efforts covered phenomena at the turbine and turbine-wake level. There was a need for an atmospheric-scale PIRT, so in FY19 the MMC team developed this atmospheric/MMC PIRT, using a draft all-encompassing PIRT from the 2015 A2e ModSim workshops that included a mesoscale PIRT as a starting point. Team members from all participating MMC labs provided input to the creation of this PIRT. Early in the effort, we realized that this PIRT is somewhat location specific, so phenomena and rankings are provided for flat onshore, complex terrain onshore, and offshore situations. We find that the offshore situation has the most high-priority phenomena due to the relative absence of measured parameters of importance, and model adequacy, level of validation, and simulation capabilities. Surprisingly, the flat onshore condition ranks second highest in terms of cumulative priority. While people often think of the flat onshore situation as relatively easy, it contains many important phenomena, including low-level jets and the land side of land-sea breezes that are challenging to simulate, yet impact a very large number of developments. Although the PIRT is a useful guide, every modeling exercise is application specific, so one must think about the application at hand and how the various phenomena affect that application to prioritize model development for that application. The MMC PIRT can therefore assist the group in developing a clearer picture of research priorities in applications that we support.

12.2 Assessment

Two new objectives have been defined and met this year for assessment of our MMC capabilities. Our first objective was to establish a repository of assessment tools with accompanying living documentation of our workflow and best practices, thereby facilitating the development and dissemination of our research. To this end, we utilized the Python language and Jupyter notebook format to meet our current requirements. This choice reflected the existence of the large Python user community, the large number of available tool libraries in the public domain, and consequently, the ease of learning, applying, and sharing these tools. In addition, Jupyter notebooks bridge the gap between coding and reporting, combining

documentation and executable Python code with inline code output and figures. Our second objective was to establish central repositories for our WRF code—with accompanying MMC-related modifications—as well as WRF simulation setups and data sets for forcing and evaluating those simulations. Having a common code base and input decks has enabled direct comparisons between simulation results, improving the quality and reproducibility of our work. In the spirit of open science and making the team's results and code readily available to industry, both of these objectives have been realized in the public domain on GitHub. Two of our current research studies comparing coupling methods and perturbation methods have successfully adopted the new tools, Jupyter notebooks, and MMC WRF code.

12.3 Mesoscale Modeling Advances

To improve mesoscale boundary layer simulation at the higher resolutions that are becoming common practice, as well as in horizontally heterogeneous settings, the MMC project has been advancing a fully 3D PBL scheme that continues work from the WFIP 2 project. Traditional methods of modeling the boundary layer in mesoscale simulations treat each vertical column independently, computing turbulent stresses and fluxes in the vertical direction only. Such an approach assumes horizontal homogeneity, which limits the applications to flat, smooth surfaces, at sufficiently coarse resolutions that horizontal transport can be neglected. During FY19, the team ported the 3D PBL code to WRF v4.0.3 and thoroughly tested it, implemented and tested a substepping scheme, implemented prognostic TKE computation, and advanced the ways that the surface boundary conditions are handled by the scheme. These advances make this 3D PBL scheme more usable in general modeling for wind energy.

12.4 Coupling Comparisons

The MMC team has identified a variety of viable mesoscale-microscale coupling methods over the past few years. In FY19, we began a formal comparison process that will continue into FY20. This process began by performing a comparison of coupling configurations on the SWiFT November 8, 2013, diurnal cycle benchmark case. Coupling configurations include WRF to WRF-LES, WRF to SOWFA in a few configurations, WRF to Nalu-Wind, and observations to SOWFA. This chapter is a snapshot of that coupling comparison effort. Beyond the flat terrain diurnal cycle case, we plan to also perform organized coupling comparisons for the offshore and complex terrain cases.

Additionally, work was performed in FY19 to develop the "profile assimilation technique" and further examine and document best practices for the "budget component approach." Also, we studied the effect of complex terrain in creating turbulence in the microscale domain when mesoscale inflow that lacks resolved turbulence is applied. Advances were made in handling atmospheric gravity waves within the microscale domain. Last, we examined the effect of the activation or deactivation of the atmospheric physical process parameterizations within the microscale domain, such that are normally activated within the mesoscale domain, and may impact the formation of turbulence and other phenomena of importance to wind energy while activated within the microscale domain as well.

12.5 Perturbation Comparisons

The turbulence working group within the MMC project team examined several different inflow perturbation methods developed to accelerate the development of resolved turbulence on microscale simulation domains forced by mesoscale (nonturbulent) inflow. These methods were

assessed within a revised team workflow, consisting of a shared repository of common code bases, data sets, and assessment scripts, as described in Section 12.2.

This year's activities focused on the assessment of inflow perturbation methods within the context of a case study culled from the unstable afternoon portion of November 08, 2013, diurnal cycle observed at the SWiFT facility. Participants from five institutions across the working group all pulled a common version of the MMC WRF code, modified to support analysis of perturbation methods, built the executable in their own environments, ran the simulations, and evaluated the results using common assessment scripts housed within the MMC GitHub. Intercomparison of results, facilitated by the use of common metrics and presentations, enabled quantitative determination of strengths and weaknesses of the various approaches, while also helping to identify tunable parameters that influence the performance of the methods. This framework will be utilized to compare other methods that have not yet undergone formal assessment, as well as to examine the performance of all of the techniques in increasingly challenging conditions, including other stability categories, complex terrain, and offshore settings, in future work.

12.6 Near-Surface Physics

New machine-learning approaches to model the surface layer based on relationships between measured data have shown improvements over traditional parameterizations based upon the Monin-Obukhov Similarity Theory. Both random forests and artificial neural networks can be trained to predict friction velocity, temperature scale, and moisture scale, even improving on MOST for flat-terrain sites different than those the models were initially trained on. The random forest approach has been tested in WRF for a diurnal cycle case, showing promise at forcing the expected diurnal case. These machine-learning models will be tested in additional onshore cases as well as for offshore implementation. Two additional methods will be tested for modeling the marine surface layer: adding forcing to the momentum equations and using immersed boundary conditions. These multiple approaches will be tested for the marine surface in the coming year, providing much needed information on best methods to model this complex offshore environment.

12.7 Uncertainty Quantification

Idealized LES have long been known to be sensitive to SGS turbulence SGS closures, but the implications for microscale simulations coupled to realistic forcing with mesoscale variability are not well characterized. To investigate this issue, an ensemble of several dozen coupled WRF/WRF-LES simulations of a convective boundary layer observed during the WFIP 2 campaign were performed, varying key parameters of a common turbulent kinetic energy-based SGS closure. Parameter sensitivity was evaluated considering different LES grid resolutions, observation locations, and sensitivity analysis methods. The robustness of these findings for onshore cases will be assessed by performing additional case studies. Moving forward, the UQ analysis approaches that the team finds to be most valuable will be applied to quantifying uncertainty in simulations of the offshore wind-plant environment.

12.8 Lidar Simulator

Scanning lidar data were constructed using a highly resolved turbulent flow field generated by WRF-LES for the unstable condition, and the PPI mode near the surface to compare the flow structures between simulated and measured lidar scanning data. These data sets were

analyzed using POD spatial modes. The fluctuating velocity about the mean of radial velocity and the orientation and size of spatial structures resulting from the POD modes were found to be similar among both simulated and measured data. This shows that the streak-like structures produced by WRF-LES for the moderate heat and wind condition near the surface correspond well with similar structures observed within the real atmosphere. In addition to the lidar simulator, turbulence was characterized using several days of measured scanning lidar data near the surface for unstable conditions. The lidar data (simulated and measured) were binned into different groups according to the magnitude of mean and variance of the radial velocity of the scanned sector before applying the POD approach. The spatial POD modes of these data showed that the varying size and shape of spatial structures depend on the mean and variance of radial velocity of the scanned sector. The structures of the POD spatial modes change from cellular to streak-like as the magnitude of mean and variance of the radial velocity increases. This result reflects that scale of turbulence is a function of the forcing conditions and that the POD approach can be used to analyze the turbulence structures.

12.9 Comparison of Nalu-Wind to Other Microscale Models

Nalu-Wind is a relatively new microscale solver with advanced capabilities for wind-plant simulation. Due to its novelty, it was not included in an intercomparison of microscale solvers performed previously by the MMC team (Mirocha et al. 2018). We revisited this earlier study, using Nalu-Wind to simulate the same suite of neutral and convective boundary layer scenarios based on observed conditions at the SWiFT site in west Texas. Nalu-Wind's predictions of the wind speed profile were generally found to be about as consistent with the observed wind speeds as the results of the previously tested microscale solvers, but some potential areas for improvement were also identified. Further evaluation of Nalu-Wind for simulation of atmospheric boundary layers is planned using both canonical flow configurations and coupled runs with realistic forcing derived from mesoscale simulations.

12.10 Relevance for Wind Energy

Most of the energy in the atmosphere inhabits the largest scales. It is through nonlinear interactions that this energy cascades into the finer scales, including those scales where wind plants reside. Thus, it is critical to correctly model this energy cascade as a forcing for microscale simulations of wind plants that are sufficiently detailed for making industry decisions. This MMC provides the correct forcing for those simulations that can model wake interactions, plant control strategies, analyze loads on turbines, and all applications that require models of the wind plant or turbine blades. The coupling studies are defining best practices for particular use case scenarios. The intercomparison of methods to generate turbulence will provide better turbulence intensity estimates for the load studies. Moving beyond Monin-Obukov theory to parameterize the surface layer using machine learning and real data, alternative methods such as drag or immersed boundaries, or combinations thereof, promises to improve models of the lowest layers of the atmosphere. Continued efforts to assess the models' accuracy and to quantify their uncertainty will help industry better plan in a probabilistic environment. By performing this applied research, we are building new tools that can be used by industry to make decisions using these tools that have been widely exercised on real-world cases.

To assure that the MMC efforts remain relevant to the wind industry, the team held three webinars with industry, both to present our most recent advances and to solicit feedback from industrial partners on their needs and where they see the most useful advances. In addition, MMC formed an industrial advisory panel, including six members that represent wind-plant

developers, turbine manufacturers, and wind power forecasters. This panel helped plan an industry workshop in June 2019.

12.11 Plans for the Future

At the beginning of FY20, the MMC plans to complete and publish some of the ongoing work, including the rigorous intercomparison of coupling techniques and turbulence generation methods. Completing this work will clarify best practices in this MMC domain as gleaned from several years of joint research across several laboratories. Not only will it include the nearly canonical conditions at the SWiFT site, but also use the WFIP 2 data to make some strong statements about best practices for simulating wind plants in complex terrain. The team plans to assess potential use cases and available data in parallel with finishing the onshore intercomparisons. Using machine learning for physics parameterization by publishing the onshore work and training such models for offshore conditions will test blending physics with artificial intelligence as a path for future simulation of wind-plant environments. All of these efforts will transition toward the offshore environment.

In coming years, the team will emphasize coupling the mesoscale to the microscale in the offshore environment. The team has planned a large case study of an offshore wind farm for FY20, beginning from identifying an interesting use case that includes complex physics, such as land-shore breezes and low-level jets. At the mesoscale, the team will add an appropriate surface layer for wave conditions to WRF and produce a high-quality mesoscale simulation. The mesoscale will be coupled with Nalu-Wind (or SOWFA) while generating turbulence appropriate for the conditions. The team will use actuator disk codes to simulate turbines in both WRF-LES and Nalu-Wind (SOWFA). This first simulation will help the team define what we already do well in the offshore environment and where we should focus resources in areas where we need improvement.

13.0 References

Allaerts, D., C. Draxl, E. Quon, and M. Churchfield. "Large-Eddy Simulation of a Diurnal Cycle Driven by Assimilation of Mesoscale Time-Height Profiles." *Boundary Layer Meteorology*, submitted September 2019.

Arthur, R. S., J. D. Mirocha, and K. A. Lundquist. 2018. "Using a Canopy Model Framework To Improve Large-Eddy Simulations of the Atmospheric Boundary Layer in the Weather Research and Forecasting Model." *Mon.-Wea. Rev.* **147**(1), 31-52.

Beare, R. J., M. K. MacVean, A. A. M. Holtslag, J. Cuxart, I. Esau, J.-C. Golaz, M. A. Jimenez, M. Khairoutdinov, B. Kosovic, D. Lewellen, T. S. Lund, J. K. Lundquist, A. McCabe, A. F. Moene, Y. Noh, S. Raasch, and P. P. mSullivan. 2006. "An Intercomparison of Large-Eddy Simulations of the Stable Boundary Layer." *Boundary-Layer Meteorol.* **118,** 247–272.

Brasseur, J. G., and T. Wei. 2010. "Designing Large-Eddy Simulation of the Turbulent Boundary Layer To Capture Law-of-the-Wall Scaling." *Phys. Fluids* **22,** 021303. https://doi.org/10.1063/1.3319073.

Chan, S., and M. Leach. 2007. "A Validation of FEM3MP with Joint Urban 2003 Data." *J. Appl. Meteor. Climatol.* **46**, 2127–2146.

Churchfield, M. J., S. Lee, J. Michalakes, and P. J. Moriarty. 2012. "A Numerical Study of the Effects of Atmospheric and Wake Turbulence on Wind Turbine Dynamics." *J. Turbul.* **13**, N14. https://doi.org/10.1080/14685248.2012.668191.

Deardorff, J. W. 1980. "Stratocumulus-Capped Mixed Layers Derived from a Three-Dimensional Model." *Bound. Layer Meteor.* **18,** 495-527.

de Roode, S. R., H. J. J. Jonker, B. J. H. van de Wiel, V. Vertregt, and V. Perrin. 2017. "A Diagnosis of Excessive Mixing in Smagorinsky Subfilter-Scale Turbulent Kinetic Energy Models." *J. Atmos. Sci.* **74**, 1495-1511.

Domino, S. 2015. "Sierra Low Mach Module: Nalu Theory Manual 1.0." https://github.com/NaluCFD/NaluDoc.

Draxl, C., D. Allaerts, E. Quon, and M. Churchfield. "Coupling Mesoscale Momentum and Temperature Budget Components to Large-Eddy Simulations for Wind Energy Applications." *Boundary Layer Meteorology*, submitted November 2019.

Genuer, R., J.-M. Poggi, and C. Tuleau-Malot. 2010. "Variable Selection Using Random Forests." *Pattern Recognition Letters* **31**, 2225-2236.

Haupt, S. E., B. Kosovic, W. Shaw, L. Berg, M. Churchfield, J. Cline, C. Draxl, B. Ennis, E. Koo, R. Kotamarthi, L. Mazzaro, J. Mirocha, P. Moriarty, D. Munoz-Esparza, E. Quon, R. K. Rai, M. Robinson, and G. Sever. 2019b. "On Bridging a Modeling Scale Gap: Mesoscale to Microscale Coupling for Wind Energy." *Bulletin of the American Meteorological Society,* Early online release. https://journals.ametsoc.org/doi/abs/10.1175/BAMS-D-18-0033.1?mobileUi=0.

Haupt, S. E., D. Allaerts, L. Berg, M. Churchfield, A. DeCastro, C. Draxyl, E. Koo, B. Kosovic, R. Kotamarthi, B. Kravitz, L. Mazzaro, J. Mirocha, E. Quon, R. Rai, J. Sauer, G. Sever, and W.

Shaw. 2019a. "FY18 Report of the Atmosphere to Electrons Mesoscale-to-Microscale Coupling Project." Pacific Northwest National Laboratory, PNNL-28259, 124 pp.

Haupt, S. E., A. Anderson, R. Kotamarthi, J. J. Churchfield, Y. Feng, C. Draxl, J. D. Mirocha, E. Quon, E. Koo, W. Shaw, R. Linn, L. Berg, B. Kosovic, R. Rai, B. Brown, and B. L. Ennis. 2017. "Second Year Report of the Atmosphere to Electrons Mesoscale-to-Microscale Coupling Project: Nonstationary Modeling Techniques and Assessment." Pacific Northwest National Laboratory, PNNL-26267, 156 pp.

Haupt, S. E., A. Anderson, L. Berg, B. Brown, M. J. Churchfield, C. Draxl, B. L. Ennis, Y. Fang, B. Kosović, R. Kotamarthi, R. Linn, J. D. Mirocha, P. Moriarty, D. Munoz-Esparaza, R. Rai, and W. J. Shaw. 2015. "First Year Report of the A2e Mesoscale-to-Microscale Coupling Project." Pacific Northwest National Laboratory, PNNL-25108, 124 pp.

Helton, J. C., and F. J. Davis. 2003. "Latin Hypercube Sampling and the Propagation of Uncertainty in Analyses of Complex Systems." *Reliability Engineering & System Safety* **81**.1, 23-69.

Jähn, M., D. Muñoz-Esparza, F. Chouza, O. Reitebuch, O. Knoth, M. Haarig, and A. Ansmann. 2016. "Investigations of Boundary Layer Structure, Cloud Characteristics and Vertical Mixing of Aerosols at Barbados with Large-Eddy Simulations." *Atmospheric Chemistry and Physics* 16(2), p. 651.

Jiang, P., Z. Wen, W. Sha, and G. Chen. 2017. "Interaction Between Turbulent Flow and Sea Breeze Front Over Urban-Like Coast in Large-Eddy Simulation." *Journal of Geophysical Research: Atmospheres* 122(10), 5298-5315.

Kaimal, J. C, J. C. Wyngaard, Y. Izumi, and O. R. Coté. 1972. "Spectral Characteristics of Surface-Layer Turbulence." *Quarterly Journal of the Royal Meteorological Society* **98**, no. 417, 563-589.

Kaul, C. M., S. Ananthan, M. J. Churchfield, J. D. Mirocha, L. K. Berg, and R. Rai. "Large-Eddy Simulations of Idealized Atmospheric Boundary Layers Using Nalu-Wind." NAWEA/WINDTECH, October 14-16, 2019. Amherst, MA.

Kelley, C. L., and B. L. Ennis. 2016. "SWiFT Site Atmospheric Characterization." Sandia National Laboratories, SAND2016-0216, 82 pp.

Kelley, N. D. 2011. "Turbulence-Turbine Interaction: The Basis for the Development of the TurbSim Stochastic Simulator." National Renewable Energy Laboratory, NREL/TP-5000-52353.

Lee, G. J., D. Muñoz-Esparza, C. Yi, and H. J. Choe. 2019. "Application of the Cell Perturbation Method to Large-Eddy Simulations of a Real Urban Area." *Journal of Applied Meteorology and Climatology* 58(5), pp.1125-1139.

Liaw, A., and M. Wiener. 2002. "Classification and Regression by Random Forest." *R News* **2/3**, 18-22.

Lundquist, K. A, F. K. Chow, and J. K. Lundquist. 2012. "An Immersed Boundary Method Enabling Large-Eddy Simulations of Flow Over Complex Terrain the WRF Model." *Mon. Wea. Rev.* **140**, 3936–3955.

Mann, J. 1998. "Wind Field Simulation." *Probabilistic Engineering Mechanics* **13**.4, 269-282.

Mazzaro, L. J., E. Koo, D. Munoz-Esparza, J. K. Lundquist, and R. R. Linn. 2019. "Random Force Perturbations: A New Extension of the Cell Perturbation Method for Turbulence Generation in Multiscale Atmospheric Boundary Layer Simulations." *J. Adv. Model. Earth Syst.* **11**, 2311–2329. https://doi.org/10.1029/2019MS001608.

Mazzaro, L. J., D. Munoz-Esparza, J. K. Lundquist, and R. R. Linn. 2017. "Nested Mesoscale-to-LES Modeling of the Atmospheric Boundary Layer in the Presence of Under-Resolved Convective Structures." *J. Adv. Model. Earth Syst.* 9, 1795–1810. https://doi.org/10.1002/2017MS000912.

Mellor, G. L. 1973. "Analytic Prediction of the Properties of Stratified Planetary Surface Layers." *J. Atmos. Sci.* **30**, 1061-1069. https://doi.org/10.1175/1520-0469(1973)030<1061:APOTPO>2.0.CO;2.

Mellor, G. L., and T. Yamada. 1974. "A Hierarchy of Turbulence Closure Models for Planetary Boundary Layers." *J. Atmos. Sci*. **31**, 1791-1806. https://doi.org/10.1175/1520-0469(1974)031<1791:AHOTCM>2.0.CO;2.

Mellor, G. L., and T. Yamada. 1982. "Development of a Turbulence Closure Model for Geophysical Fluid Problems." *Reviews of Geophysics* **20**, 851-875. https://doi.org/10.1029/RG020i004p00851.

Mirocha, J. D., M. J. Churchfield, D. Munoz-Esparaza, R. Rai, Y. Feng, B. Kosovic, S. E. Haupt, B. Brown, B. L. Ennis, C. Draxl, J. S. Rodrigo, W. J. Shaw, L. K. Berg, P. Moriarty, R. Linn, R.V. Kotamarthi, R. Balakrishnan, J. Cline, M. Robinson, and S. Ananthan. 2018. "Large-Eddy Simulation Sensitivities to Variations of Configuration and Forcing Parameters in Canonical Boundary Layer Flows for Wind Energy Applications." *Wind Energy Science 3,* 589-613. https://doi.org/10.5194/wes-3-589-2018.

Monin, A. S., and A. M. Obukhov. 1954. "Basic Laws of Turbulent Mixing in the Surface Layer of the Atmosphere." *Tr. Akad. Nauk. SSSR Geophiz. Inst*. **24** (151), 163–187.

Morrison, H., G. Thompson, and V. Tatarskii. 2009. "Impact of Cloud Microphysics on the Development of Trailing Stratiform Precipitation in a Simulated Squall Line: Comparison of One- and Two-Moment Schemes." *Mon. Wea. Rev.* **137**, 991-1007. https://doi.org/10.1175/2008MWR2556.1.

Munoz-Esparza, D., B. Kosovic, J. D. Mirocha, and J. van Beeck. 2014. "Bridging the Transition from Mesoscale-to-Microscale Turbulence in Numerical Weather Prediction Models." *Boundary Layer Meteorol.* 153(3), 409–440. https://doi.org/10.1007/s10546-014-9956-9.

Muñoz-Esparza, D., B. Kosović, J. van Beeck, and J. Mirocha. 2015. "A Stochastic Perturbation Method To Generate Inflow Turbulence in Large-Eddy Simulation Models: Application to Neutrally Stratified Atmospheric Boundary Layers." *Physics of Fluids (1994-present)* **27**, 035102. https://doi.org/10.1063/1.4913572.

Muñoz-Esparza, D., J. K. Lundquist, J. A. Sauer, B. Kosovic, and R. R. Linn. 2017. "Coupled Mesoscale-LES Modeling of a Diurnal Cycle During the CWEX-13 Field Campaign: From

Weather to Boundary-Layer Eddies." *J. Adv. Model. Earth Syst.* **9,** 1572–1594. https://doi.org/10.1002/2017MS000960.

Muñoz-Esparza, D., and B. Kosović. 2018. "Generation of Inflow Turbulence in Large-Eddy Simulations of Nonneutral Atmospheric Boundary Layers with the Cell Perturbation Method." *Mon. Wea. Rev.* **146**(6), 1889-1909.

Muñoz-Esparza, D., R. Sharman, J. Sauer, and B. Kosović. 2018. "Toward Low-Level Turbulence Forecasting at Eddy-Resolving Scales." *Geophysical Research Letters* **45**(16), 8655-8664.

Nakanishi, M., and H. Niino. 2006. "An Improved Mellor-Yamada Level 3 Model: Its Numerical Stability and Application to a Regional Prediction of Advecting Fog." *Bound. Layer Meteor.* 119, 397-407.

Quon, E. W., A. S. Ghate, and S. K. Lele. 2018. "Enrichment Methods for Inflow Turbulence Generation in the Atmospheric Boundary Layer." *J. Phys.: Conf. Ser.* **1037**, 072054. https://doi.org/10.1088/1742-6596/1037/7/072054.

Rai, R. K., L. K. Berg, B. Kosović, J. D. Mirocha, M. S. Pekour, and W. J. Shaw. 2017. "Comparison of Measured and Numerically Simulated Turbulence Statistics in a Convective Boundary Layer Over Complex Terrain." *Boundary-Layer Meteorology* **163**, 69–89.

Rai, R. K., L. K. Berg, B. Kosović, J. D. Mirocha, M. S. Pekour, and W. J. Shaw. 2016. "Comparison of Measured and Numerically Simulated Turbulence Statistics in a Convective Boundary Layer Over Complex Terrain." *Bound.-Layer Meteor*. **163**, 69-98.

Rai, R. K., L. K. Berg, B. Kosovic, S. E. Haupt, J. D. Mirocha, B. Ennis, and C. Draxl. 2019. "Evaluation of the Impact of Horizontal Grid Spacing in Terra Incognita on Coupled Mesoscale-Microscale Simulations Using the WRF Framework." *Monthly Wea. Rev.* **147**, 1007-1027. https://journals.ametsoc.org/doi/abs/10.1175/MWR-D-18-0282.1.

Rodrigo, J. S., M. Churchfield, and B. Kosovic. 2016. "Atmospheric Boundary Layer Modeling Based on Mesoscale Tendencies and Data Assimilation at Microscale." *Wind Energy Science Discussions*. https://doi.org/10.5194/wes-2016-26.

Sauer, J. A., D. Muñoz-Esparza, J. M. Canfield, K. R. Costigan, R. R. Linn, and Y. J. Kim. 2016. "A Large-Eddy Simulation Study of Atmospheric Boundary Layer Influence on Stratified Flows Over Terrain." *J. Atmos. Sci.* **73**, 2615-2632. https://doi.org/10.1175/JAS-D-15-0282.1.

Shaw, W. J., L.K. Berg, J. Cline, C. Draxl, I. Djalalova, E.P. Grimit, J.K. Lundquist, M. Marquis, J. McCaa, J.B. Olson, C. Sivaraman, J. Sharp, and J.M. Wilczak, 2019. "The Second Wind Forecast Improvement Project (WFIP 2): General Overview." *Bull. Amer. Meteor. Soc.* **100**, 1687–1699.

Shaw, R. H., and E. G. Patton. 2003. "Canopy Element Influences on Resolved- and Subgrid-Scale Energy within a Large-Eddy Simulation." *Agr. For. Meteor.* **115**, 5–17.

Skamarock, W. C., J. B. Klemp, J. Dudhia, D. O. Gill, D. M. Barker, M. G. Dudhia, X.-Y. Huang, W. Wang, and J. G. Powers. 2008. "A Description of the Advanced Research WRF Version 3." *National Center for Atmospheric Research,* NCAR/TN-4751STR.

Stein, M. 1987. "Large Sample Properties of Simulations Using Latin Hypercube Sampling." *Technometrics* **29.2**, 143-151.

Wyngaard, J. C. 2004. "Toward Numerical Modeling in the '*Terra Incognita'*." *J. Atmos. Sci.* **61**, 1816-1826.

Xie, Z.-T., and I. P. Castro. 2008. "Efficient Generation of Inflow Conditions for Large Eddy Simulation of Street-Scale Flows." *Flow, Turbul. and Combust.* **81**, 449–470. https://doi.org/10.1007/s10494-008-9151-5.

Yang, B., Y. Qian, L. K. Berg, P.-L. Ma, S. Wharton, V. Bulaevskaya, H. Yan, Z. Hou, and W. J. Shaw. 2017. "Sensitivity of Turbine-Height Wind Speeds to Parameters in Planetary Boundary-Layer and Surface-Layer Schemes in the Weather Research and Forecasting Model." *Bound. Layer Meteor.* **162**, 117-142. https://doi.org/10.1007/s10546-016-0185-2.

Appendix A – List of Project Publications

A.1   Journal Articles

Allaerts, D., C. Draxl, E. Quon, and M. Churchfield. "Large-Eddy Simulation of a Diurnal Cycle Driven by Assimilation of Mesoscale Time-Height Profiles." *Boundary Layer Meteorology*, submitted September 2019.

Abstract: Mesoscale-to-microscale coupling aims to address the limited scope of traditional large-eddy simulations by driving the microscale flow with information concerning large-scale weather patterns provided by mesoscale models. This paper presents a new offline mesoscale-to-microscale coupling technique for horizontally homogeneous microscale flow conditions in which adequate mesoscale internal source terms are computed based on mesoscale time-height profiles of mean flow quantities. The advantage of such an approach is that it doesn't rely on mesoscale budget components, which are not outputted by default by most mesoscale solvers, and that it could also be used to drive microscale simulations with observational data. The performance of the proposed profile assimilation technique is assessed based on the simulation of a quiescent diurnal cycle over the Scaled Wind Farm Facility (SWiFT) site in west Texas. Results indicate that simple data assimilation techniques lead to unphysically high levels of shear and turbulence caused by the algorithm's inability to cope with inaccuracies in the mesoscale time-height profiles. Modifying the algorithm to account for vertical coherence in the mesoscale internal source terms allows the microscale solver to take over and correct the provided mesoscale time-height profiles, leading to improved predictions of turbulence statistics in line with meteorological tower observations and simulation results obtained with standard internal forcing coupling techniques.

Arthur, R. S., J. D. Mirocha, and K. A. Lundquist. 2018. "Using a Canopy Model Framework To Improve Large-Eddy Simulations of the Atmospheric Boundary Layer in the Weather Research and Forecasting Model. *Mon.-Wea. Rev.* **147**(1), 31-52. https://doi.org/10.1175/MWR-D-18-0204.1.

Abstract: A canopy model framework is implemented in the Weather Research and Forecasting model to improve the accuracy of large-eddy simulation (LES) of the atmospheric boundary layer (ABL). The model includes two options that depend on the scale of surface roughness elements. A resolved canopy model, typically used to model flow through vegetation canopies, is employed when roughness elements are resolved by the vertical LES grid. In the case of unresolved roughness, a modified "pseudo-canopy model" is developed to distribute drag over a shallow layer above the surface. Both canopy model options are validated against idealized test cases in neutral stability conditions and are shown to improve surface layer velocity profiles relative to simulations employing Monin-Obukhov Similarity Theory (MOST), which is commonly used as a surface boundary condition in ABL models. Use of the canopy model framework also leads to increased levels of resolved turbulence kinetic energy and turbulent stresses. Because LES of the ABL has a well-known difficulty recovering the expected logarithmic velocity profile (log-law) in the surface layer, particular focus is placed on using the pseudo-canopy model to alleviate this issue over a range of model configurations. Tests with varying surface roughness values, LES closures, and grid aspect ratios confirm that the pseudo-canopy model generally improves log-law agreement relative to simulations that employ a standard MOST boundary condition. The canopy model framework thus represents a low-cost, easy-to-implement method for improving LES of the ABL.

Draxl, C., D. Allaerts, E. Quon, and M. Churchfield. "Coupling Mesoscale Momentum and Temperature Budget Components to Large-Eddy Simulations for Wind Energy Applications." *Boundary Layer Meteorology*, submitted November 2019.

Abstract: Wind plants are exposed to a variety of weather phenomena on many scales— from synoptic to mesoscale to microscale conditions. Mesoscale phenomena are described by mesoscale numerical weather prediction models and drive large horizontal variations on the microscale. Microscale turbulence and flow structures can be predicted by large-eddy simulation (LES) models and are important because their variability impacts the operating environment of wind plants. To simulate wind flow through a wind plant across a wide range of atmospheric conditions that drive wind plant performance, microscale models have to be coupled with mesoscale models, because microscale models lack atmospheric physical processes to represent local forcing.

Here we couple mesoscale model output to an LES solver by applying mesoscale momentum and temperature budget components from the Weather Research and Forecasting model to the governing equations of Simulator fOr Wind Farm Applications (SOWFA). We test whether averaging the budget components impacts the LES simulations with regard to quantities of interest to wind energy. Results show that averaging reduces the spatiotemporal variability of the mesoscale momentum budget components; however, when coupled with LES, the mesoscale bias (in comparison with observations in wind speed, wind direction, and potential temperature) is not corrected by the LES simulation. On the contrary, LES can correct for shear and veer. In both cases, however, averaging the budget components showed no significant impact on mean flow quantities in the microscale and is not necessary when coupling mesoscale budget components to LES.

Haupt, S. E., B. Kosovic, W. Shaw, L. Berg, M. Churchfield, J. Cline, C. Draxl, B. Ennis, E. Koo, R. Kotamarthi, L. Mazzaro, J. Mirocha, P. Moriarty, D. Munoz-Esparza, E. Quon, R. K. Rai, M. Robinson, and G. Sever. 2019. "On Bridging a Modeling Scale Gap: Mesoscale-to-Microscale Coupling for Wind Energy." *Bulletin of the American Meteorological Society,* Early online release. https://journals.ametsoc.org/doi/abs/10.1175/BAMS-D-18-0033.1?mobileUi=0.

Abstract: Accurately representing flow across the mesoscale to microscale is a persistent roadblock for completing realistic microscale simulations. The science challenges that must be addressed to coupling at these scales include: 1) What is necessary to capture the variability of the mesoscale flow and how do we avoid generating spurious rolls within the *terra incognita* between the scales? 2) Which methods effectively couple the mesoscale to the microscale and capture the correct nonstationary features at the microscale? 3) What are the best methods to initialize turbulence at the microscale? 4) What is the best way to handle the surface layer parameterizations consistently at the mesoscale and the microscale? 5) How do we assess the impact of improvements in each of these aspects and quantify the uncertainty in the simulations?

The U.S. Department of Energy Mesoscale-to-Microscale-Coupling project seeks to develop, verify, and validate physical models and modeling techniques that bridge the most important atmospheric scales determining wind plant performance and reliability, which impacts many meteorological applications. The approach begins with choosing case days that are interesting for wind energy for which there are observational data for validation. The team has focused on modeling nonstationary conditions for both flat and complex terrain. This paper describes the approaches taken to answer the science challenges, culminating in recommendations for best approaches for coupled modeling.

Mirocha, J. D., M. J. Churchfield, D. Munoz-Esparaza, R. Rai, Y. Feng, B. Kosovic, S. E. Haupt, B. Brown, B. L. Ennis, C. Draxl, J. S. Rodrigo, W. J. Shaw, L. K. Berg, P. Moriarty, R. Linn, R. V. Kotamarthi, R. Balakrishnan, J. Cline, M. Robinson, and S. Ananthan. 2017. "Large-Eddy Simulation Sensitivities to Variations of Configuration and Forcing Parameters in Canonical Boundary Layer Flows for Wind Energy Applications." *Wind Energy Sci.* **3**, 589-613. https://doi.org/10.5194/wes-3-589-2018.

Abstract: The sensitivities of idealized large-eddy simulations (LES) to variations of model configuration and forcing parameters on quantities of interest to wind power applications are examined. Simulated wind speed, turbulent fluxes, spectra and cospectra are assessed in relation to variations of two physical factors: geostrophic wind speed and surface roughness length, and several model configuration choices, including mesh size and grid aspect ratio, turbulence model, and numerical discretization schemes, in three different code bases. Two case studies representing nearly steady neutral and convective atmospheric boundary layer (ABL) flow conditions over flat terrain, occurring at the Sandia Scaled Wind Farm Technology test facility, were used to force and assess idealized LES using periodic lateral boundary conditions. Comparison with fast-response velocity measurements at five heights within the lowest 50 m indicates that most model configurations performed similarly overall, with differences between observed and predicted wind speed generally smaller than measurement variability. Simulations of convective conditions produced turbulence quantities and spectra that matched the observations well, while those of neutral simulations produced good predictions of stress, but smaller than observed magnitudes of turbulence kinetic energy, likely due to tower wakes influencing the measurements during the neutral case. While sensitivities to model configuration choices and variability in forcing can be considerable, idealized LES are shown to reliably reproduce quantities of interest to wind energy applications within the lower ABL during quasi-ideal, nearly steady neutral and convective conditions.

Rai, R. K., L. K. Berg, B. Kosović, S. E. Haupt, J. D. Mirocha, B. L. Ennis, and C. Draxl. 2019. "Evaluation of the Impact of Horizontal Grid Spacing in Terra Incognita on Coupled Mesoscale–Microscale Simulations Using the WRF Framework." *Monthly Weather Review* 147(3), 1007-1027.

Abstract: Coupled mesoscale–microscale simulations are required to provide time-varying weather-dependent inflow and forcing for large-eddy simulations under general flow conditions. Such coupling necessarily spans a wide range of spatial scales (i.e., ~10 m to ~10 km). Herein, we use simulations that involve multiple nested domains with horizontal grid spacings in the terra incognita (i.e., $\leqslant 1$ km) that may affect simulated conditions in both the outer and inner domains. We examine the impact on simulated wind speed and turbulence associated with forcing provided by a terrain with grid spacing in the terra incognita. We perform a suite of simulations that use combinations of varying horizontal grid spacings and turbulence parameterization/modeling using the Weather Research and Forecasting (WRF) Model using a combination of planetary boundary layer (PBL) and large-eddy simulation subgrid-scale (LES-SGS) models. The results are analyzed in terms of spectral energy, turbulence kinetic energy, and proper orthogonal decomposition (POD) energy. The results show that the output from the microscale domain depends on the type of turbulence model (e.g., PBL or LES-SGS model) used for a given horizontal grid spacing but is independent of the horizontal grid spacing and turbulence modeling of the parent domain. Simulation using a single domain produced less POD energy in the first few modes compared to a coupled simulation (one-way nesting) for similar horizontal grid spacing,

which highlights that coupled simulations are required to accurately pass the mesoscale features into the microscale domain.

Rai, R. K., L. K. Berg, M. Pekour, W. J. Shaw, B. Kosovic, J. D. Mirocha, and B. L. Ennis. 2017. Spatio-Temporal Variability of Turbulence Kinetic Energy Budgets in the Convective Boundary Layer over Both Simple and Complex Terrain." *J. Appl. Meteor.and Climatol.* https://doi.org/10.1175/JAMC-D-17-0124.1 (in press).

Abstract: The assumption of subgrid-scale (SGS) horizontal homogeneity within a model grid cell, which forms the basis of SGS turbulence closures used by mesoscale models, becomes increasingly tenuous as grid spacing is reduced to a few kilometers or less, such as in many emerging high-resolution applications. Herein, we use the turbulence kinetic energy (TKE) budget equation to study the spatiotemporal variability in two types of terrain—complex (Columbia Basin Wind Energy Study [CBWES] site, northeastern Oregon) and flat (Scaled Wind Farm Technology [SWiFT] site, West Texas) using the Weather Research and Forecasting (WRF) model. In each case, six-nested domains (three domains each for mesoscale and large-eddy simulation [LES]) are used to downscale the horizontal grid spacing from ~10 km to ~10 m using the WRF model framework. The model output was used to calculate the values of the TKE budget terms in vertical and horizontal planes as well as the averages of grid cells contained in the four quadrants (a quarter area) of the LES domain. The budget terms calculated along the planes and the mean profile of budget terms show larger spatial variability at the CBWES site than at the SWiFT site. The contribution of the horizontal derivative of the shear production term to the total shear production was found to be ≈45% and ≈15% at the CBWES and SWiFT sites, respectively, indicating that the horizontal derivatives applied in the budget equation should not be ignored in mesoscale model parameterizations, especially for cases with complex terrain with <10 km scale.

Rai, R. K., L. K. Berg, B. Kosovic, J. D. Mirocha, M. S. Pekour, and W. J. Shaw. 2016. "Comparison of Measured and Numerically Simulated Turbulence Statistics in a Convective Boundary Layer over Complex Terrain." *Bound.-Layer Meteor.* **163**, 69-98.

Abstract: The Weather Research and Forecasting (WRF) model can be used to simulate atmospheric processes ranging from quasi-global to tens of meters in scale. Here we employ large-eddy simulation (LES) using the WRF model, with the LES domain nested within a mesoscale WRF model domain with grid spacing decreasing from 12.15 km (mesoscale) to 0.03 km (LES). We simulate real-world conditions in the convective planetary boundary layer over an area of complex terrain. The WRF-LES model results are evaluated against observations collected during the U. S. Department of Energy-supported Columbia Basin Wind Energy Study. Comparison of the first- and second-order moments, turbulence spectrum, and probability density function of wind speed shows good agreement between the simulations and observations. One key result is to demonstrate that a systematic methodology needs to be applied to select the grid spacing and refinement ratio used between domains, to avoid having a grid resolution that falls in the grey zone, and to minimize artefacts in the WRF-LES model solutions. Furthermore, the WRF-LES model variables show large variability in space and time caused by the complex topography in the LES domain. Analyses of WRF-LES model results show that the flow structures, such as roll vortices and convective cells, vary depending on both the location and time of day as well as the distance from the inflow boundaries.

Simon, J. S., B. Zhou, J. D. Mirocha, and F. K. Chow. 2019. "Explicit Filtering and Reconstruction To Reduce Grid Dependence in Convective Boundary Layer Simulations Using WRF-LES." *Mon.-Wea. Rev.* 147(5), 1805-1821. https://doi.org/10.1175/MWR-D-18-0205.1.

Abstract: As model grid resolutions move from the mesoscale to the microscale, turbulent structures represented in atmospheric boundary layer simulations change dramatically. At intermediate resolutions, the so-called gray zone, turbulent motions are not resolved accurately, posing a challenge to numerical simulations. The representation of turbulence is also highly sensitive to the choice of closure model. Here, we examine explicit filtering and reconstruction in the gray zone as a technique to better represent atmospheric turbulence. The convective boundary layer is simulated using the Weather Research and Forecasting (WRF) Model with horizontal resolutions ranging from 25 m to 1 km. Four large-eddy simulation (LES) turbulence models are considered: the Smagorinsky model, the TKE-1.5 model, and two versions of the dynamic reconstruction model (DRM). The models are evaluated by their ability to produce consistent mean potential temperature profiles, heat and momentum fluxes, velocity fields, and turbulent kinetic energy spectra as the grids become coarser. The DRM, a mixed model that uses an explicit filtering and reconstruction technique to account for resolvable subfilter-scale (RSFS) stresses, performs very well at resolutions of 500 m and 1 km without any special tuning, whereas the Smagorinsky and TKE-1.5 models produce heavily grid-dependent results.

A.2   Conference Papers (presenter in bold)

Allaerts, D., C. Draxl, and M. Churchfield. "Large-Eddy Simulations of a Diurnal Cycle Driven by Mesoscale and Observational Profile Assimilation." American Physical Society Division of Fluid Dynamics Meeting, November 18-20, 2018. Atlanta, GA.

Allaerts, D., C. Draxl, E. Quon, and M. Churchfield, "Evaluation of Internal Forcing Techniques for Mesoscale-to-Microscale Coupling." 2019 Wind Energy Science Conference, June 16-20, 2019. Cork, Ireland.

Arthur, R. S., J. D. Mirocha, N. Marjanovic, B. D. Hirth, J. L. Schroeder, and **F. K. Chow**. "Multi-Scale Simulations of Wind Farm Performance with Complex Terrain and Weather Events." NAWEA/WINDTECH, October 14-16, 2019. Amherst, MA.

Churchfield, M., D. Allaerts, P. Hawbecker, and E. Quon. "Treatment of Gravity Waves in Wind Energy Atmospheric Large-Eddy Simulation." June 16-20, 2019. Cork, Ireland.

Cline, J. W., **W. J. Shaw**, and S. E. Haupt. "Meteorology Research in DOE's Atmosphere to Electrons (A2e) Program." Ninth Conference on Weather, Climate, and the New Energy Economy, AMS Annual Meeting, January 8, 2018. Phoenix, AZ.

Cline, J., S. E. Haupt, and W. Shaw. "Meteorology Research in DOE's Atmosphere to Electrons (A2e) Program, WindTech International Conference on Future Technologies in Wind Energy, October 24, 2017. Boulder, CO.

Draxl, C., M. Churchfield, and J. S. Rodrigo. "Coupling the Mesoscale to the Microscale Using Momentum Budget Components." North American Wind Energy Symposium, September 2017. Ames, IA.

Draxl, C., M. Churchfield, and J. S. Rodrigo. "Coupling the Mesoscale to the Microscale Using Momentum Budget Components." AMS Annual Meeting, January 2017. Seattle, WA.

Haupt, S. E., L. Berg, M. Churchfield, B. Kosovic, W. Shaw, and J. Mirocha. "Mesoscale to Microscale Coupling for Wind Energy Applications: Addressing the Challenges." NAWEA/WindTech Conference, October 15, 2019. Amherst, MA.

Haupt, S. E. "Advances in Mesoscale to Microscale Coupling for Wind Energy Applications." 6th International Conference on Energy and Meteorology, June 25, 2019. Lyngby, Denmark.

Haupt, S. E. "Mesoscale to Microscale Coupling for Wind Energy Applications." Energy Systems Integration Group Meteorology & Market Design for Grid Services Workshop, June 5, 2019. Denver, CO.

Haupt, S. E., B, Kosovic, W. Shaw, L. Berg, R. Rai, J. Mirocha, M. Churchfield, C. Draxl, and M. Robinson. "Recent Advances in Mesoscale to Microscale Coupling." AMS Conference on Boundary Layers and Turbulence, June 14, 2018. Oklahoma City, OK.

Haupt, S. E. "Progress in Mesoscale to Microscale Coupling: Modeling Nonstationary Conditions in Flat and Complex Terrain." International Conference on Energy & Meteorology, May 22, 2018. Shanghai, China.

Haupt, S. E. "Meteorology, Climate, and the Electric Sector – Forecasting for an Integrated Energy System." ESIG Forecasting Workshop, June 19, 2018 (invited panel talk). St. Paul, MN.

Haupt, S. E., L. Berg, M. Churchfield, J. Cline, J. Mirocha, B. Kosovic, C. Draxl, R. Rai, R. Kostmarthi, M. Robinson, and W. Shaw. "The U.S. DOE A2e Mesoscale-to- Microscale Coupling Project: Nonstationary Modeling Techniques and Assessment." International Conference on Energy and Meteorology, June 28, 2017. Bari, Italy.

Haupt, S. E., **J. Cline**, W. Shaw, L. Berg, M. Churchfield, J. Mirocha, B. Kosovic, C. Draxl, R. Rai, and R. Kotamarthi. "The U.S. DOE A2e Mesoscale-to-Microscale Coupling Project: Nonstationary Modeling Techniques and Assessment." European Geophysical Union, April 26, 2017. Vienna, Austria.

Haupt, S. E., W. Shaw, B. Kosovic. "The DOE A2e Mesoscale-to-Microscale Coupling Project." AMS Symposium on Boundary Layers and Turbulence, June 20, 2016. Salt Lake City, UT.

Haupt, S. E. "Meteorology Models Enabling Wind Energy." Wyoming Renewable Energy Summit, June 13, 2016 (invited keynote). Laramie, WY.

Haupt, S. E., W. Shaw, and B. Kosovic. "Meso-to-Microscale Coupling Project." WindTech Workshop, October 19, 2015. London, Ontario, Canada.

Hawbecker, P., and M. Churchfield. "Mesoscale-to-Microscale Coupling for a Wind Ramp Case over Complex Terrain." 99th American Meteorology Society Annual Meeting, January 8, 2019. Phoenix, AZ.

Kosovic, B., J. D. Mirocha, M. J. Churchfield, D. Munoz-Esparza, R. K. Rai, Y. Feng, S. E. Haupt, B. Brown, B. L. Ennis, C. Draxl, J. Sanz Rodrigo, W. J. Shaw, L. K. Berg, P. Moriarty, R. Linn, and R. V. Kotamarthi. "Assessment of Large-eddy Simulations of the Atmospheric

Boundary Layer for Wind Energy Applications." WindTech International Conference on Future Technologies in Wind Energy, October 25, 2017. Boulder, CO.

Kaul, C. M., S. Ananthan, M. J. Churchfield, J. D. Mirocha, L. K. Berg, and R. Rai. "Large-Eddy Simulations of Idealized Atmospheric Boundary Layers Using Nalu-Wind." NAWEA/WINDTECH, October 14-16, 2019. Amherst, MA.

Mirocha, J. D. "Toward the Integration of Atmosphere and Wind Plant Physics and Simulation Techniques: An Overview of the DOE's Mesoscale-Microscale Coupling Project." Meteorology and Climate - Modeling for Air Quality Conference, U.C. Davis, September 11, 2019. Davis, CA.

Mirocha, J. D. and S. E. Haupt. "The U.S. DOE Mesoscale-to-Microscale Coupling Project: Extending Boundary Layer Flow Simulation to Complex Environments." Ninth Conference on Weather, Climate, and the New Energy Economy, AMS Annual Meeting, January 8, 2018. Phoenix, AZ.

Mirocha, J. D., R. K. Rai, M. J. Churchfield, Y. Feng, C. Draxl, J. Sanz Rodrigo, B. L. Ennis, B. Kosović, and S. E. Haupt. "An Investigation of Online and Offline Mesoscale-Microscale Coupling Techniques During Unsteady Meteorological Conditions." WindTech International Conference on Future Technologies in Wind Energy, October 25, 2017. Boulder, CO.

Quon, E. W., A. S. Ghate, and S. K. Lele. 2018. "Enrichment Methods for Inflow Turbulence Generation in the Atmospheric Boundary Layer." *J. Phys.: Conf. Ser.*, **1037**, 072054, https://doi.org/10.1088/1742-6596/1037/7/072054.

Rai, R. K., L. K. Berg, B. Kosovic, J. D. Mirocha, S. E. Haupt, B. L. Ennis, and C. Draxl. "Evaluation of the Impact on Terra Incognita for Mesoscale and Microscale WRF Simulations." WindTech International Conference on Future Technologies in Wind Energy, October 25, 2017. Boulder, CO.

Rai, R. K., L. K. Berg, B. Kosovic, J. D. Mirocha, M. Pekour, B. Ennis, and W. J. Shaw. "Examination of the Spatio-Temporal Variability of the Terms of the Turbulent Kinetic Energy Budget over a Complex Terrain in the Convective Boundary Layer: A Tool for Parameterization Development." American Meteorological Society Meeting, January 24, 2017. Seattle, WA.

Rai, R. K., L. K. Berg, B. Kravitz, B. Kosovic, J. D. Mirocha, B. Ennis, and S. E. Haupt. "Improving Simulation of Turbulence in WRF-LES of Stable Condition Using Velocity Fluctuations." Tenth Conference on Weather, Climate, and the New Energy Economy, AMS Annual Meeting, January 8, 2019. Phoenix, AZ.

Rai, R. K., L. K. Berg, C. Kaul, J. Mirocha, A. Choukulkar, W. A. Brewer, Y. Pichugina, and R. Banta. "Characterization of Turbulence Under Different Stability Conditions Using Lidar Scanning Data Near the WFIP 2 Physics Site." NAWEA/WINDTECH, October 14-16, 2019. Amherst, MA.

Sever, G., R. V. Kotamarthi, and Y. Feng. "A Turbulence Library for Asynchronous Coupling of Meso and Microscale Models." WindTech - International Conference on Future Technologies in Wind Energy, October 25, 2017. Boulder, CO.

Appendix B – Contributions of Individual Laboratories

Lawrence Livermore National Laboratory: LLNL's primary contributions to the MMC project during FY19 were: 1) to lead the effort to assess various inflow perturbation methods used to accelerate turbulence development on turbulence-resolving microscale simulation domains forced by mesoscale (nonturbulent) inflow, and 2) to make available new codes and case study data sets on a publicly accessible site, to encourage tech transfer and engagement with others in research and industry. As described in detail in Section 7.0, achievement of these goals necessitated a significant shift in the team's established workflow, including transition of all team members to a common code development and assessment environment. This new environment, consisting of core computational codes, data to force and evaluate model simulations, and assessment scripts, achieves several important goals, including improved collaboration across the team, more rigorous code development and documentation practices, unambiguous intercomparison and assessment of various methods, and finally a platform from which to share new codes and procedures, both across the team and with any interested party who wishes to investigate or adopt our tools and techniques (https://github.com/a2e-mmc). While LLNL provided high-level oversight of the perturbation assessment and code dissemination tasks, NCAR and NREL led several of the major components of developing the community environment, the code modification and validation framework, and the generation of the multiple data processing and analysis scripts used to assess the methods.

In addition to the common code development, analysis, and dissemination framework, LLNL also implemented improvements into the stochastic cell perturbation method, including a height-dependent perturbation refresh timescale, and ability to utilize boundary-layer height computed from the bounding mesoscale simulation during a nested simulation. LLNL also continued developing the distributed drag surface canopy parameterization with a view toward complex terrain and offshore applications. LLNL also worked with collaborators at UC Berkeley to examine the use of the more sophisticated "DRM" dynamic LES subgrid model, relative to simpler linear eddy-viscosity approaches, in simulating turbulence at coarse model resolutions and into grey zone scales. Finally, LLNL continued to assist in project planning, and communication and dissemination, including participating in team and industry meetings and teleconferences, and contributing material for and presenting at conferences.

Los Alamos National Laboratory: LANL's primary contribution to the MMC project during FY19 was participation in the effort to assess various inflow perturbation methods used to accelerate turbulence development on turbulence resolving microscale simulation domains forced by mesoscale inflow, as described in Section 7.0. As part of this effort, LANL made available to the team codes related to the random force perturbation extension of the cell perturbation method and ran simulations based on case study data sets provided by LLNL.

LANL team members attended in-person and phone MMC meetings and have contributed to journal publications in FY19, including one first-author publication on the random force extension of the cell perturbation method.

National Center for Atmospheric Research: NCAR continued to serve in a leadership role for the MMC project, which includes leading biweekly team telecons, representing the team at A2e meetings and external peer reviews, and facilitating and publicizing the work. Dr. Haupt served as project Principal Investigator and contributed to the A2e Uber-PI meetings as well as overall project leadership, including work planning and tracking. NCAR hosted team workshops in Boulder in January and April 2019. Dr. Haupt was also responsible for summaries in quarterly reports and producing this FY19 Annual Report and presented an overview of project progress

at DOE Headquarters in May 2019. She also led a team summary paper that appears in the *Bulletin of the American Meteorological Society*. The NCAR team members presented papers on MMC work at the Tenth Conference on Weather, Climate, and the New Energy Economy held as part of the American Meteorological Society (AMS) Annual Meeting in Phoenix, AZ in January 2019; Energy Systems Integration Group Forecast conference in Denver in June 2019; Wind Energy Science Conference in Cork, Ireland in June 2019; International Conference on Energy and Meteorology held in Lyngby, Denmark in June 2019; and the MAC-MAQ conference in California in September 2019.

NCAR led the assessment planning and implementation. In FY19, that process was formalized (in collaboration with NREL and the other laboratories) and new standardized processes were initiated. The team moved toward completing postprocessing and assessment in Jupyter notebooks in Python, with standard code archived on a GitHub repository. In addition, standard code bases were initiated, which allows more rigorous comparison of techniques.

NCAR led the Mesoscale Modeling portion of the project in 2019, producing some use cases and also advancing the 3D PBL scheme that was initiated in the WFIP 2 project. NCAR also began incorporating new machine-learning models for the surface layer as part of the MMC project in FY19. The team is in the process of moving the emphasis of our research toward applications in the offshore environment. NCAR is providing leadership in assessing the primary needs for the offshore environment and incorporating that expertise into the team.

National Renewable Energy Laboratory: NREL's main roles within the MMC project during FY19 were: 1) to lead the coupling methods group, including the formal coupling methods assessment for the SWiFT flat-terrain, diurnal cycle case outlined in Chapter 6.0 of this report, 2) to lead the creation of the A2e-MMC Github repository and work side-by-side with NCAR to produce high-quality Python codes for performing everything from simulation assessment to publication-quality plots outlined in Chapter 4.0 of this report, and 3) to develop new coupling-related methods. Some specific highlight activities that members from the NREL team undertook include participation in mesoscale modeling efforts, participation in the inflow turbulence perturbation comparison effort, development of the new profile assimilation coupling technique and further analyzed the budget-component coupling approach, examination of the role of terrain in microscale inflow turbulence generation, enhancement of the use of TurbSim for inflow turbulence generation, and development of strategies for atmospheric gravity wave handling in the microscale.

NREL continued to assist in project planning. Members of the NREL team attended the in-person and phone meetings of the overall MMC group. The NREL team is providing overlap between MMC and other A2e projects, including the High-Fidelity Modeling (HFM), Wake Dynamics, and Controls Science projects.

Members of the NREL team have been first-authors or coauthors of various journal publications in FY19 and presented work at conferences, including the American Physical Society Division of Fluid Dynamics Meeting, the American Meteorological Society Annual Meeting, and the Wind Energy Science meeting.

Pacific Northwest National Laboratory: PNNL staff contributed to many facets of the MMC project, including: preliminary testing of Nalu-Wind, development of coupling methods, development of perturbation methods, development and application of a lidar simulator, UQ, and assessment. Efforts related to Nalu-Wind focused on setting up, running, and evaluating Nalu-Wind simulations using the same case studies presented by Mirocha et al. (2018). This

work was presented by Kaul et al. (2019) at the North American Wind Energy Academy (NAWEA)/International Conference on Future Technologies in Wind Energy (WindTech) conference and is described in detail in Chapter 11.0 of this report. The team's work on perturbation methods focused on generating turbulence using synthetic methods, such as those of Mann or Veers (Chapter 7.0). Application of a new lidar simulator gives the opportunity to more carefully evaluate the nature of turbulence in the planetary boundary layer. This work is presented in Chapter 10.0 and is a collaboration with the A2e WFIP 2 project. Staff renewed efforts focused on UQ presented in Chapter 9.0 that are focused on LES applications and builds on other UQ efforts.

PNNL staff contributed to or led (Rai et al. 2019) several peer-reviewed publications. The team also presented results at the American Meteorological Society Annual Meeting and the NAWEA/WindTech conference.

Pacific Northwest National Laboratory

902 Battelle Boulevard
P.O. Box 999
Richland, WA 99354
1-888-375-PNNL (7665)

www.pnnl.gov